



Transportation Consortium of South-Central States

Solving Emerging Transportation Resiliency, Sustainability, and Economic Challenges through the Use of Innovative Materials and Construction Methods: From Research to Implementation

Development of a Self-Powered Weigh-in-Motion System

Project No. 19ITSUTSA01

Lead University: University of Texas at San Antonio

Final Report
December
2020

Disclaimer

The contents of this report reflect the views of the authors, who are responsible for the facts and the accuracy of the information presented herein. This document is disseminated in the interest of information exchange. The report is funded, partially or entirely, by a grant from the U.S. Department of Transportation's University Transportation Centers Program. However, the U.S. Government assumes no liability for the contents or use thereof.

Acknowledgements

The authors would like to acknowledge the support by the Transportation Consortium of South-Central States (TranSET)

TECHNICAL DOCUMENTATION PAGE

1. Project No. 19ITSUTSA01	2. Government Accession No.	3. Recipient's Catalog No.	
4. Title and Subtitle Development of a Self-Powered Weigh-in-Motion System		5. Report Date Dec. 2020	
7. Author(s) PI: A.T. Papagiannakis https://orcid.org/0000-0002-3047-7112 Co-PI: Sara Ahmed https://orcid.org/0000-0003-0935-5011 Co-PI: Samer Dessouky https://orcid.org/0000-0002-6799-6805 GRA: Reza Khalili https://orcid.org/0000-0002-8383-4945 GRA: Gopal Vishwakarma https://orcid.org/0000-0002-5440-9149		6. Performing Organization Code	
9. Performing Organization Name and Address Transportation Consortium of South-Central States (Tran-SET) University Transportation Center for Region 6 3319 Patrick F. Taylor Hall, Louisiana State University, Baton Rouge, LA 70803		8. Performing Organization Report No.	
12. Sponsoring Agency Name and Address United States of America Department of Transportation Research and Innovative Technology Administration		10. Work Unit No. (TRAIS)	
		11. Contract or Grant No. 69A3551747106	
		13. Type of Report and Period Covered Final Research Report Aug. 2019 – Dec. 2020	
		14. Sponsoring Agency Code	
15. Supplementary Notes Report uploaded and accessible at Tran-SET's website (http://transet.lsu.edu/) .			
16. Abstract <p>This report describes the development of a novel weigh-in-motion (WIM) system that utilizes piezoelectric elements for sensing load and powering an ultra-low power microcontroller unit (MCU) that serves as its data acquisition system. A system of 4 piezoelectric (PZT) stacks serves as the energy harvester, while load sensing is done via a set of 4 PZT elements connected in parallel. Two alternative MCUs were considered, with various data handling capabilities and power consumption requirements. These MCUs have very short “wake-up” times allowing vehicle sensing without the need for inductive loops commonly used in conventional WIM systems. Special electric circuits were developed for maximizing the power output and for conditioning/sensing the voltage output. Electromechanical models were fitted to describe the relationship between voltage output, load and loading frequency/vehicle speed. Software were developed implementing the electromechanical model selected for estimating vehicle speed, axle load, number of axles and their spacing as well as vehicle classification. The software was first implemented in Matlab® and then converted to C prior to loading on the MCU memory. The system was tested in the laboratory by applying loads through a UTM servo-hydraulic loading system. Accuracies in measuring load, speed and class were successfully compared to the tolerances prescribed by the ASTM standard E1318.</p>			
17. Key Words Structural health monitoring, power harvesting, sensor, thermoelectric		18. Distribution Statement Restricted pending IP disclosure.	
19. Security Classif. (of this report) Unclassified	20. Security Classif. (of this page) Unclassified	21. No. of Pages 96	22. Price

Form DOT F 1700.7 (8-72)

Reproduction of completed page authorized.

SI* (MODERN METRIC) CONVERSION FACTORS

APPROXIMATE CONVERSIONS TO SI UNITS

Symbol	When You Know	Multiply By	To Find	Symbol
LENGTH				
in	inches	25.4	millimeters	mm
ft	feet	0.305	meters	m
yd	yards	0.914	meters	m
mi	miles	1.61	kilometers	km
AREA				
in ²	square inches	645.2	square millimeters	mm ²
ft ²	square feet	0.093	square meters	m ²
yd ²	square yard	0.836	square meters	m ²
ac	acres	0.405	hectares	ha
mi ²	square miles	2.59	square kilometers	km ²
VOLUME				
fl oz	fluid ounces	29.57	milliliters	mL
gal	gallons	3.785	liters	L
ft ³	cubic feet	0.028	cubic meters	m ³
yd ³	cubic yards	0.765	cubic meters	m ³
NOTE: volumes greater than 1000 L shall be shown in m ³				
MASS				
oz	ounces	28.35	grams	g
lb	pounds	0.454	kilograms	kg
T	short tons (2000 lb)	0.907	megagrams (or "metric ton")	Mg (or "t")
TEMPERATURE (exact degrees)				
°F	Fahrenheit	5 (F-32)/9 or (F-32)/1.8	Celsius	°C
ILLUMINATION				
fc	foot-candles	10.76	lux	lx
fl	foot-Lamberts	3.426	candela/m ²	cd/m ²
FORCE and PRESSURE or STRESS				
lbf	poundforce	4.45	newtons	N
lbf/in ²	poundforce per square inch	6.89	kilopascals	kPa
APPROXIMATE CONVERSIONS FROM SI UNITS				
Symbol	When You Know	Multiply By	To Find	Symbol
LENGTH				
mm	millimeters	0.039	inches	in
m	meters	3.28	feet	ft
m	meters	1.09	yards	yd
km	kilometers	0.621	miles	mi
AREA				
mm ²	square millimeters	0.0016	square inches	in ²
m	square meters	10.764	square feet	ft ²
m	square meters	1.195	square yards	yd ²
ha	hectares	2.47	acres	ac
km	square kilometers	0.386	square miles	mi ²
VOLUME				
mL	milliliters	0.034	fluid ounces	fl oz
L	liters	0.264	gallons	gal
m	cubic meters	35.314	cubic feet	ft ³
m	cubic meters	1.307	cubic yards	yd ³
MASS				
g	grams	0.035	ounces	oz
kg	kilograms	2.202	pounds	lb
Mg (or "t")	megagrams (or "metric ton")	1.103	short tons (2000 lb)	T
TEMPERATURE (exact degrees)				
C	Celsius	1.8C+32	Fahrenheit	°F
ILLUMINATION				
lx	lux	0.0929	foot-candles	fc
cd/m ²	candela/m ²	0.2919	foot-Lamberts	fl
FORCE and PRESSURE or STRESS				
N	newtons	0.225	poundforce	lbf
kPa	kilopascals	0.145	poundforce per square inch	lbf/in ²

TABLE OF CONTENTS

TECHNICAL DOCUMENTATION PAGE	ii
TABLE OF CONTENTS.....	iv
LIST OF FIGURES	vi
LIST OF TABLES	xii
ACRONYMS and ABBREVIATIONS.....	xiii
SYMBOLS.....	xiv
EXECUTIVE SUMMARY	xvi
1 INTRODUCTION	1
1.1 Background	1
1.2 Conventional WIM Technology	2
1.3 Piezoelectric Materials as Sensors and Harvesters	4
2 OBJECTIVES	6
3 LITERATURE REVIEW	7
3.1 Theory of Linear Piezoelectricity.....	7
3.2 Piezoelectric Electromechanical Model	9
3.3 Piezoelectric Energy Harvesting (PEH) Fundamentals	13
3.4 PEH Applications in Pavements	15
4 METHODOLOGY	1
4.1 Fabricating and Testing the PEH Elements.....	1
4.1.1 Harvester Prototype Fabrication	1
4.1.2 Testing Facilities	4
4.1.3 Testing Isolated PZT Disks.....	6
4.1.4 Testing Individual PZT Disks within a PZT Stack.....	9
4.1.5 Testing PZT Stacks	11
4.1.6 Summary of Findings.....	30
4.2 Electromechanical Modeling.....	31
4.2.1 Isolated PZT Disk Model.....	31
4.2.2 PZT Stack Model	33
4.2.3 Model for Four PZT Stacks Connected in Parallel.....	38

4.2.4	In Summary.....	40
4.3	WIM Enclosure Design and PZT Sensing Model.....	40
4.3.1	WIM Enclosure Design.....	40
4.3.2	Laboratory Testing and PZT Sensor Model Calibration.....	45
4.3.3	In Summary.....	51
4.4	WIM AND CLASSIFICATION ALGORITHMS.....	51
4.4.1	Signal Conditioning	51
4.4.2	Frequency/Vehicle Speed Estimation.....	54
4.4.3	Nominal versus Actual Test Frequencies	56
4.4.4	Refitting the PZT Sensing Model Using Actual Frequencies.....	57
4.4.5	Classification Algorithm.....	58
4.4.6	Data output format	62
4.4.7	Algorithm for Load Estimation.....	62
4.4.8	Algorithm Implementation.....	63
4.4.9	In Summary.....	64
4.5	Circuitry Design.....	66
4.5.1	PZT Sensing Element Circuit	66
4.5.2	Energy Harvesting Circuit	66
4.5.3	The MCUs Considered	67
4.5.4	In Summary.....	69
5	ANALYSIS AND FINDINGS	70
5.1.	WIM System Testing	70
5.1.1.	Algorithm Performance	70
5.1.2.	Testing the MCU #1 in the laboratory	73
5.2.	PEH Power Generation	78
5.2.1.	PEH Matlab/Simulink® simulation.....	78
5.2.2.	PEH laboratory testing.....	88
6	CONCLUSIONS.....	91
7	REFERENCES	92

LIST OF FIGURES

Figure 1. (a) Location of WIM sites in Texas (b) Location of WIM sites in Ohio (2107).....	1
Figure 2. FHWA vehicle classification scheme based on vehicle “signatures”.	2
Figure 3. Instrumented Plate WIM sensor examples (a) Load cell (b) Bending plate.....	3
Figure 4. a) Polymer piezo sensor b) Polymer piezo installation schematic.	3
Figure 5. a) Quartz piezo sensor b) Quartz piezo installation schematic.....	3
Figure 6. Piezoelectric coupling representation for low frequencies.....	10
Figure 7. Mechanical model of a vibrating mass.....	11
Figure 8. Piezoelectric electromechanical model.	11
Figure 9. Equivalent electrical circuit of a piezoelectric element at low frequencies (21).....	12
Figure 10. A bridge rectifier built with four diodes translates AC current into DC (https://www.electronics-tutorials.ws/diode/diode_6.html).	14
Figure 11. Circuitual interface for piezoelectric energy harvesting (27).....	14
Figure 12. Piezoelectric structure a) 33 mode b) 31 mode (22).....	15
Figure 13. Piezoelectric disks are assembled into stacks connected in parallel.	1
Figure 14. Copper sheet work pieces before and after electroplating. The electrodes are cut from these work pieces (right).....	2
Figure 15. Work pieces resting in a 10% alkaline cleaner 60 °C tank.	2
Figure 16. Electroplating setup. Notice that the current is set to 1 Amp.....	3
Figure 17. PEH elements (a) before soldering (b) after soldering.....	4
Figure 18. Types of applied mechanical load in UTM machine: a) Continuous sinusoidal loading b) Pulsating loading.	4
Figure 19. 10 Hz continuous sinusoidal load with an amplitude of 11 kN.....	5
Figure 20. 10 Hz pulsating load with an 11 kN amplitude and a rest period of 0.9 sec.	5
Figure 21. Laboratory setup.....	6
Figure 22. Example of voltage output from 30 Hz load of 1.1 kN on a single PZT element.....	7
Figure 23. Voltage signal amplitudes based on two methods.....	8
Figure 24. Percentage difference between the two methods of calculating the signal amplitude for different frequencies.	8
Figure 25. RMS power from one PZT disk; Sinusoidal 1.1 kN load, frequencies 2.5 Hz-62 Hz. .	9
Figure 26. Test condition for top disk within the stack with sinusoidal loading.....	10

Figure 27. Test condition for top disk within the stack with pulsating loading.....	10
Figure 28. Voltage amplitudes (a) Top disk within stack no rectifier (b) Top disk within stack with rectifier.....	11
Figure 29. The power output from (a) top disk within the stack (b) rest of the 5 disks in the stack.	11
Figure 30. Relationship between stress and OC voltage for four fabricated stacks.	12
Figure 31. Voltage amplitude versus stress amplitude under an external electrical load of 3 M Ω ; Stack A, sinusoidal load of 10 Hz frequency.....	13
Figure 32. Stress versus output voltage; Stack A, external resistance of 3 M Ω ; Pulse loading of 11 kN, 0.1 sec and 0.9 sec rest period.....	14
Figure 33. OC voltage versus stress for different frequencies.....	14
Figure 34. The effect of frequency on αOCf	15
Figure 35. Voltage versus stress for various frequencies; 650 k Ω external resistor, pulse loading.	15
Figure 36. The effect of frequency on $\alpha 650 \text{ k}\Omega f$	16
Figure 37. RMS power and electrical load for stack A under 3 kN 10 Hz sinusoidal load The matching impedance is 3 M Ω where the graph reaches its maximum.	17
Figure 38. RMS power output versus electrical load resistance relationship at the same frequency for (a) sinusoidal excitation force (b) pulsating excitation.	18
Figure 39. RMS power output versus electrical load resistance for various frequencies; (a) sinusoidal load with 1.1 kN peaks (b) sinusoidal load with 6 kN peaks.	18
Figure 40. The influence of rectifying the piezoelectric output voltage.....	19
Figure 41. Testing two PZT stacks connected in parallel.....	19
Figure 42. Voltage output versus external resistance; Two PZT stacks connected in parallel; sinusoidal loads, (a) 1.1 kN and (b) 2.2 kN.	20
Figure 43. Power output versus external resistance; Two PZT stacks connected in parallel; Sinusoidal loads, (a) 1.1 kN and (b) 2.2 kN.	21
Figure 44. Different rectifier configurations (a) two rectifiers (b) one rectifier.	22
Figure 45. Two stacks connected to individual rectifiers connected in parallel (a) Voltage amplitude (b) RMS power.	22
Figure 46. The comparison of the power from two parallel stacks with and without rectifier.....	23
Figure 47. Circuit configuration for two stacks in series with rectifiers.	23
Figure 48. Output of two stacks for 10 Hz in series with and without rectifier compared to parallel a) Voltage amplitude b) RMS power.....	24

Figure 49. Output of two stacks for 62 Hz in series with rectifier compared to parallel a) Voltage amplitude b) RMS power.....	24
Figure 50. RMS power from three stacks in parallel for a) 10 Hz b) 62 Hz.....	26
Figure 51. Voltage measured at 1M Ω relationship to excitation force at 10 Hz for three stacks in parallel compared to one individual stack.	26
Figure 52. Power output of one, two and three stacks in parallel for a) 10 Hz b) 62 Hz.	27
Figure 53. Power versus number of PZT stacks under a load of 1.1 kN (a) 10 Hz (b) 62 Hz.....	27
Figure 54. Output of four stacks connected in parallel (a) Voltage amplitude (b) RMS Power. .	28
Figure 55. Matching impedance and frequency relationship; Four PZT stacks in parallel versus a single PZT stack.....	29
Figure 56. Effect of the number of stacks connected in parallel; Each stack carries the same load of 1.1 kN applied at 10 Hz (a) Voltage (b) Power.	29
Figure 57. Effect of the number of stacks connected in parallel; Each stack carries the same load of 1.1 kN applied at 62 Hz (a) Voltage (b) Power.	30
Figure 58. Power output versus number of stacks; Each stack carries 1.1 kN (a) Loading frequency of 10 Hz (b) Loading frequency of 62 Hz.	30
Figure 59. Electro-mechanical correspondence of piezoelectric materials: (a) Electromechanical model and (b) Equivalent electrical circuit.....	31
Figure 60. Frequency dependent model parameters for a single isolated disk.	33
Figure 61. Frequency dependent electrical constants for one PZT stack; (a) C_P and (b) C_{em}	34
Figure 62. Electro-mechanical model verification using laboratory data obtained for various loads and frequencies.	35
Figure 63. Power output versus impedance and frequency; (a) 1.1 kN load, (b) 11.1 kN load....	35
Figure 64. Individual PZT stack outputs subjected to a total load of 4.4 kN at 10 Hz; External resistance of 3 M Ω	36
Figure 65. Matching impedance versus loading frequency of a PZT stack.....	37
Figure 66. Comparison between the matching impedance of one disk and the stack.	37
Figure 67. The ratio of matching impedance of disk and stack with respect to frequency.	38
Figure 68. Frequency dependent electrical constants for four PZT stacks; (a) C_P and (b) C_{em}	39
Figure 69. Electro-mechanical model verification using laboratory data obtained for various loads and frequencies for the 4 PZT stacks.....	39
Figure 70. Comparison between the frequency dependent model parameters (a) C_P (b) C_{em}	40
Figure 71. PEH Housing schematic illustrating the location of the 4 PZT stacks.....	41

Figure 72. PEH box installed in the road schematic (a) top view (b) section view.....	41
Figure 73. Design axles (a) dual tires (b) single tires.	41
Figure 74. Top plate of the box modelled as simply supported beam a) loading from dual tires b) loading from single tire.....	42
Figure 75. (a) FE model for the static pavement system and the energy-harvesting module (not to scale); and (b) mesh of the pavement structure.	43
Figure 76. Vertical stresses in the asphalt concrete under the center axis of the load.....	44
Figure 77. Fabricated PEH box and PZT posts (a) Top/bottom parts (b) Fully assembled box...	45
Figure 78. Detail of the PZT stacks and their support inside the PEH enclosure.....	45
Figure 79. Testing 4 PZT sensors in parallel; (a) Rigid plate, (b) Scaled-down PEH enclosure.	46
Figure 80. Frequency dependent parameters for PZT sensors; (a) C_P and (b) C_{em} ; ϕ frequency independent.	46
Figure 81. Frequency dependent parameters for PZT sensors; (a) C_P and (b) C_{em} ; ϕ frequency dependent.	47
Figure 82. The fitted parameter ϕ as a function of loading frequency.....	47
Figure 83. Sensors model verification for (a) 3 kN 50 Hz (b) 6 kN 20 Hz.	48
Figure 84. Sensors model verification for (a) 3 kN 50 Hz (b) 6 kN 20 Hz.	49
Figure 85. OC voltage versus force for four PZT sensors under 20 Hz for the experimental set up in 5-7(b).	49
Figure 86. Test setups in order to evaluate the effect of rigidity of the top plate.....	50
Figure 87. Voltage versus force for the experimental set up in 5-7(a).	50
Figure 88. Four PZT Sensor model comparison using data generated from the experimental set up in Figure 77(a); (a) 3 kN 50 Hz (b) 6 kN 20 Hz.	50
Figure 89. Schematic of the raw voltage output, the rectified and scaled down voltage.....	52
Figure 90. Signal before and after the filtering; (a) 4.4 kN at 30 Hz (b)11 kN at 62 Hz.....	52
Figure 91. Oscilloscope measurement for a 4.4 kN 30 Hz load; Oscilloscope resolution of 25 V.	53
Figure 92. Rectified four PZT sensor output in response to a load of 11 kN at 62 Hz.....	53
Figure 93. Sensor output of a 4.4 kN 30 Hz load.	55
Figure 94. Sensor output for an 8 kN load at 62 Hz.	56
Figure 95. Model 2 fitted using actual frequencies; External resistances 50 k Ω to 10 M Ω	57
Figure 96. Model 3 fitted using actual frequencies; External resistances 50 k Ω to 1 M Ω	58

Figure 97. Example of estimating voltage amplitude; 8 kN load at a 62 Hz nominal frequency.	63
Figure 98. Flowchart logic for implementing the algorithm.....	65
Figure 99. Block diagram of the electronic circuitry.....	66
Figure 100. Original MCU Unit; STM8L152M8T6 (57).....	67
Figure 101. Alternative MCU unit; LPC54018-IoT-Module + OM4006 base board (58).....	68
Figure 102. Matlab® algorithm measured versus applied loads; Sampling at 2.5 kHz.	71
Figure 103. Matlab® algorithm measured versus applied loads; Sampling at 5 kHz.	71
Figure 104. Experimental set up for testing the MCU #1.....	74
Figure 105. Simulated loading sequence for a Class 3 vehicle.....	74
Figure 106. Simulated loading sequence for a Class 5 vehicle.....	75
Figure 107. Simulated loading sequence for a Class 6 vehicle.....	76
Figure 108. Simulated loading sequence for a Class 9 vehicle.....	77
Figure 109. Equivalent PZT circuit in Matlab/Simulink®.....	78
Figure 110. Example of Matlab/Simulink® model validation results.....	79
Figure 111. Simulation results of one PZT stack with resistive load at 62 Hz and 6 kN (a) voltage, (b) current and (c) power versus time.	80
Figure 112. Simulation circuit schematic for a PZT stack feeding the diode rectifier, and resistive load.....	80
Figure 113. Simulation results of one PZT stack with diode rectifier and resistive load at 62 Hz and 6 kN (a) voltage, (b) current and (c) power versus time.	81
Figure 114. (a) Model of four stacks of PZT, (b) four PZT stacks connected to a diode rectifier and an equivalent resistive load.....	82
Figure 115. Simulation results of four PZT stacks with diode rectifier and equivalent resistive load at 62 Hz and 6 kN (a) voltage, (b) current and (c) power versus time.	83
Figure 116. Simulation results of one PZT stack with diode rectifier and resistive load at 62 Hz and 6 kN (a) voltage, (b) current and (c) power versus time.	84
Figure 117. Simulation circuit schematic with four PZT stacks, diode rectifier, flyback DC/DC converter and a resistive load.....	85
Figure 118. Simulation results at the output of the diode rectifier for four PZT stacks with diode rectifier, flyback DC/DC converter and resistive load of 145 Ω at 62 Hz and 6 kN (a) voltage, (b) current and (c) power versus time.	86
Figure 119. Simulation results at the flyback output of four PZT stacks with diode rectifier, flyback DC/DC converter and resistive load of 145 Ω at 62 Hz and 6 kN (a) voltage, (b) current and (c) power versus time.	87

Figure 120. Simulation results at the flyback output of four PZT stacks with diode rectifier, flyback DC/DC converter and resistive load of 42Ω at 62 Hz and 11 kN (a) voltage, (b) current and (c) power versus time. 88

Figure 121. Experimental setup of the four piezo-stacks with diode rectifier, flyback DC/DC converter, resistive load and LEDs. 89

Figure 122. Experimental result – output voltage of the four piezo-stacks with diode rectifier, flyback DC/DC converter, resistive load and LEDs. 90

LIST OF TABLES

Table 1. WIM system types based on their accuracy tolerances (3).....	4
Table 2. Literature overview of PEH applications for pavements.....	15
Table 3. Piezoelectric material properties(47) and (48).....	1
Table 4. Slope of the PZT stack voltage output versus stress at 10 Hz.	12
Table 5. Experimentally obtained matching impedances of one versus two PZT stacks connected in parallel.	21
Table 6. Comparison of series and parallel connections in terms of maximum power and the matching impedance for low and high frequencies.	25
Table 7. Fitted parameters of an isolated disk that was used to build the stacks.....	32
Table 8. Fitted parameters of the model of one individual stack.....	33
Table 9. Fitted parameters of the model for four PZT stacks connected in parallel.....	38
Table 10. Material Properties for the FE Static Analysis	43
Table 11. Oscilloscope electronic noise.....	54
Table 12. Nominal versus actual frequencies established from manual Δt measurements.	56
Table 13. Nominal versus actual frequencies established from the algorithm.	56
Table 14. Estimated algorithm errors in estimating vehicle speed.	57
Table 15. Vehicle Classification Algorithm (55).....	59
Table 16. Standardized Vehicle W-Record Format (TMG 2016).	62
Table 17. Load measurement error statistics of Matlab® algorithm; Sampling at 2.5 kHz.	72
Table 18. Load measurement error statistics of Matlab® algorithm; Sampling at 5 kHz.	72
Table 19. Error statistics for the simulated Class 3 vehicle shown in Figure 103.....	75
Table 20. Error statistics for the simulated Class 5 vehicle shown in Figure 104.....	75
Table 21. Error statistics for the simulated Class 6 vehicle shown in Figure 105.....	76
Table 22. Error statistics for the simulated Class 9 vehicle shown in Figure 106.....	77

ACRONYMS and ABBREVIATIONS

AASHTO - American Association of State Highway and Transportation Officials

AC - Alternative Current

AISI - American Iron and Steel Institute

ASTM - American Society for Testing and Materials

DAQ - Data Acquisition

DC - Direct Current

FWHA - Federal Highway Administration

GVW - Gross Vehicle Weight

LED - Light-Emitting Diode

LTPP - Long-Term Pavement Performance

MAF - Monthly Adjustment Factor

MCU - Microcontroller Unit

MEMS - Micro Electronic Mechanical System

MEPD - Mechanistic-Empirical Pavement Design

NALDS - Normalized Axle Load Spectra

OC - Open Circuit

PEH - Piezoelectric Energy Harvester

PVDF - Polyvinylidene Fluoride

PZT - Lead Zirconate Titanate

RAM - Random Access Memory

RMS - Root Mean Square

SD - Standard Deviation

SD Memory - Secure Digital Memory

USB - Universal Serial Bus

UTM - Universal Testing Machine

VCD - Vehicle Classification Distributions

WIM - Weigh-In-Motion

SYMBOLS

U = stored energy density of the piezoelectric continuum [J]

V = Voltage [V]

T = Stress [kPa]

S = Strain

D = Electric displacement per unit area [$C.m^{-2}$]

G_1 = elastic Gibbs energy

G = Gibbs free energy

F = Helmholtz free energy

H = electric Gibbs energy or electric enthalpy

E_i = Electric field tensor [$N.C^{-1}$ or $V.m^{-1}$]

e_{kij} = Piezoelectric constant

d_{kij} = Alternative form of piezoelectric constant [$C.N^{-1}$]

ϵ_{ij}^S = Permittivity constant evaluated at constant strain [$F.m^{-1}$]

c_{ijkl}^E = The elastic stiffness constant under constant electrical field

s_{ijkl}^E = elastic compliance under constant electrical field

M_m = Mass [kg]

B_m = Damping coefficient [$N.s.m^{-1}$]

K = Stiffness coefficient [$N.m^{-1}$]

$x(t)$ = Displacement [m]

ϕ = Relates the mechanical properties of PZT to electrical analogous counterparts [$V.N^{-1}$]

F_{in} = Excitation force amplitude [N]

C_m = Compliance coefficient, [$m.N^{-1}$]

Z = Electrical impedance [Ω]

R = Electrical resistance [Ω]

C_{em}, C_p = Capacitance constants in piezoelectric model [F]

L_{em} - Inductance [H]

ω = Angular frequency [rad/s]

f = Frequency [Hz]

j = Imaginary unit

t = Thickness [m]

v = velocity [m/s]

i = current [C/s]

N = the number of turns of the transformer

d = duty ratio

EXECUTIVE SUMMARY

This report describes the development of a novel weigh-in-motion (WIM) system that utilizes piezoelectric elements for sensing load and powering an ultra-low power microcontroller unit (MCU) that serves as its data acquisition system. A system of 4 piezoelectric (PZT) stacks serves as the energy harvester, while load sensing is done via a set of 4 PZT elements connected in parallel. Each PZT stack consists of 6 cylindrical PZT elements of 1-inch in diameter placed on top of each other and connected in parallel by alternating their polarities. This allows increasing the amperage while decreasing the voltage output of the stacks that serve as the piezoelectric energy harvesters (PEHs). On top of each PZT stack, there is an electrically isolated cylindrical PZT element of 1-inch diameter. Four of these elements connected in parallel serve as the load sensors. The WIM box enclosure has a simple “shoe-box” design, with each corner of its upper plate supported by one of the PZT stacks/sensor combinations. The box was sized to capture one wheel path (i.e., 28-inch wide by 8 inch long).

Two MCUs were considered, with varying data handling capabilities and power consumption requirements. These MCUs have very short “wake-up” times allowing vehicle sensing without the need for inductive loops commonly used by commercially available WIM systems. The common headway of 2 seconds was allotted to separate vehicles. The advantage of the faster MCU is that it allows a higher sampling frequency of 2.5 kHz and can handle parallel processing, which shortens the time need to process each vehicle. Within the 2 second time interval allotted to each vehicle, the time interval of loading pulses allows computing the loading frequency/vehicle speed and the time interval between pulses allows computing the axle spacing. The amplitude of pulses and the loading frequency is input into the electromechanical model of the sensing elements to predict load. Special electric circuits were developed for maximizing the power output and for conditioning/sensing the voltage output. Electromechanical models were fitted to describe the relationship between voltage output, load and loading frequency/vehicle speed. A servo-hydraulic Universal Testing Machine (UTM) was used to apply loads at various frequencies. An oscilloscope was used for collecting the voltage output data. The model for the four PZT stacks connected in parallel was used for simulating the energy harvesting potential of the system, while the model for the PZT elements was used to translate voltage output to load for sensing purposes.

Software was developed implementing the electromechanical model fitted for sensing. It outputs vehicle speed, axle load, number of axles and their spacing as well as vehicle classification according to the FHWA 13 vehicle scheme. The data is output for each individual vehicle using the W-record format specified in the 2016 Traffic Monitoring Guide. The software was first implemented in Matlab® and then converted to C language prior to loading onto MCU memory. The system was tested in the laboratory by applying loading sequences simulating various vehicle classes. The results show that vehicle speed and classification predictions are accurate and axle load predictions are precise and in general within the tolerance limits prescribed by the ASTM standard E1318. Additional work is need to implement and field test the faster MCU, which will shorten the time needed to process a vehicle.

1 INTRODUCTION

1.1 Background

Traffic data collection is an essential input to roadway infrastructure design and management. It encompasses the collection of a multitude of data elements ranging from simple traffic volume counts to vehicle classification and axle weighing. Automated axle load weighing systems measure individual axle loads and classify vehicles without stopping them. These systems are called weigh-in-motion (WIM) systems. They are better suited for traffic data collection than the static weigh scales used for load enforcement, since the latter are by their function biased towards the heavier loaded vehicles. WIM data are widely used in pavement design, bridge design and traffic analysis, as well as in screening overloaded trucks for law enforcement purposes. Roadway agencies in the United States spend millions annually for purchasing/maintaining WIM systems and processing their output. Despite that, there is seldom a sufficient amount of traffic load data, mainly because there is a limited number of permanent WIM stations available. In 2017, for example, Texas operated 39 permanent WIM stations to cover 314k center-line miles of their national highway system alone. Similarly, Ohio operated 50 permanent WIM stations to cover their 122k center-line miles (Figure 1). Site-specific traffic loads are a key input in obtaining realistic influence lines and transverse load distribution for designing new bridges and assessing existing ones (1). Site-specific WIM data is also essential for the mechanistic-empirical pavement design (MEPD) that state agencies are in the process of implementing (2). The data elements required include vehicle classification distributions (VCDs), monthly adjustment factors (MAFs) and normalized axle load spectra (NALDS). Considering the shortage of permanent WIMs, it is necessary to assemble this traffic input by combining limited site-specific traffic information with representative regional or national traffic data obtained from other permanently installed WIM systems. This introduces a high uncertainty in the traffic load input, which could result in significant underestimation of the required structural thicknesses needed to accommodate the actual traffic loads. Clearly, more accurate site specific WIM data and larger number of WIM stations can improve traffic load estimation and reduce design uncertainties.

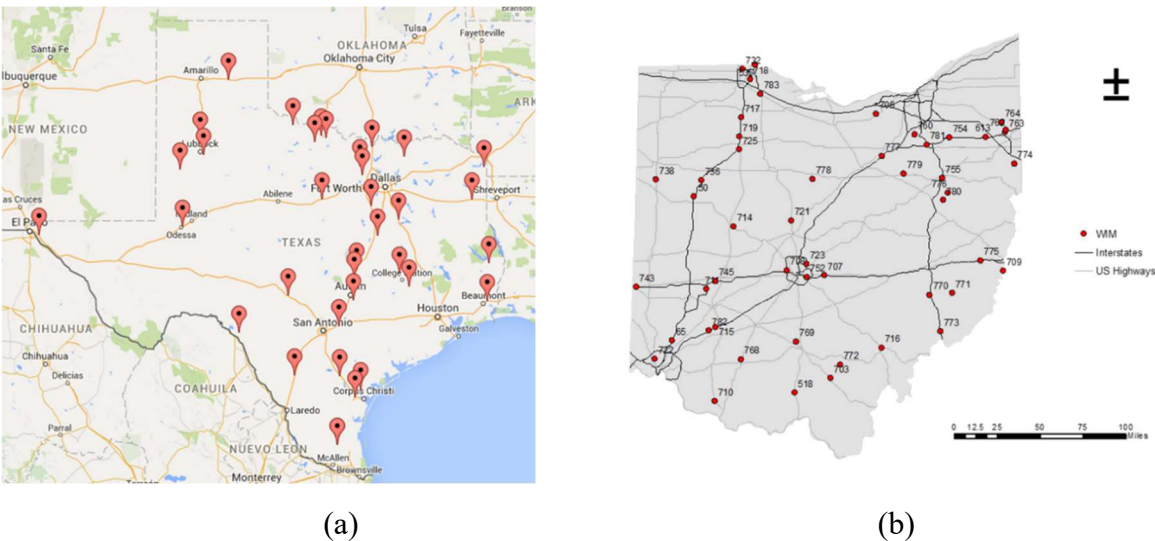


Figure 1. (a) Location of WIM sites in Texas (b) Location of WIM sites in Ohio (2107).

1.2 Conventional WIM Technology

WIM systems utilize a combination of inductive loops and one or more axle load sensors. Axle load sensors consist of either plates equipped with load cells or strain gauges, or strips made of piezoelectric or quartz materials. The inductive loops allow measuring vehicle speed and hence, allow estimation of the axle spacing and the vehicle class of passing vehicles. The most common vehicle classification scheme is the one defined by the Federal Highway Administration (FHWA) distinguishing 13 vehicle classes (Figure 2). It is noted that from a pavement design point of view, only heavy vehicles are of interest (i.e., FHWA classes 4-13).











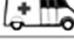

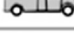


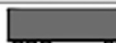




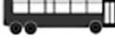

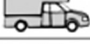

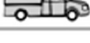

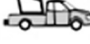










Class 1 Motorcycles		Class 7 Four or more axle, single unit	
Class 2 Passenger cars		Class 8 Four or less axle, single trailer	
			
			
			
Class 3 Four tire, single unit		Class 9 5-Axle tractor semitrailer	
			
			
Class 4 Buses		Class 10 Six or more axle, single trailer	
			
			
Class 5 Two axle, six tire, single unit		Class 11 Five or less axle, multi trailer	
			
			
Class 6 Three axle, single unit		Class 12 Six axle, multi-trailer	
			
			
		Class 13 Seven or more axle, multi-trailer	
			
			

Figure 2. FHWA vehicle classification scheme based on vehicle “signatures”.

Examples of WIM plate sensors are shown in Figure 3. An example of a polymer piezo strip sensor is shown in Figure 4, while a quartz piezo strip sensor is shown in Figure 5. The data acquisition systems of these systems are either PC-based or use a proprietary microcontroller unit (MCU). Typically, they are installed in a roadside box, powered by the electric grid and require internet connection for uploading the data.

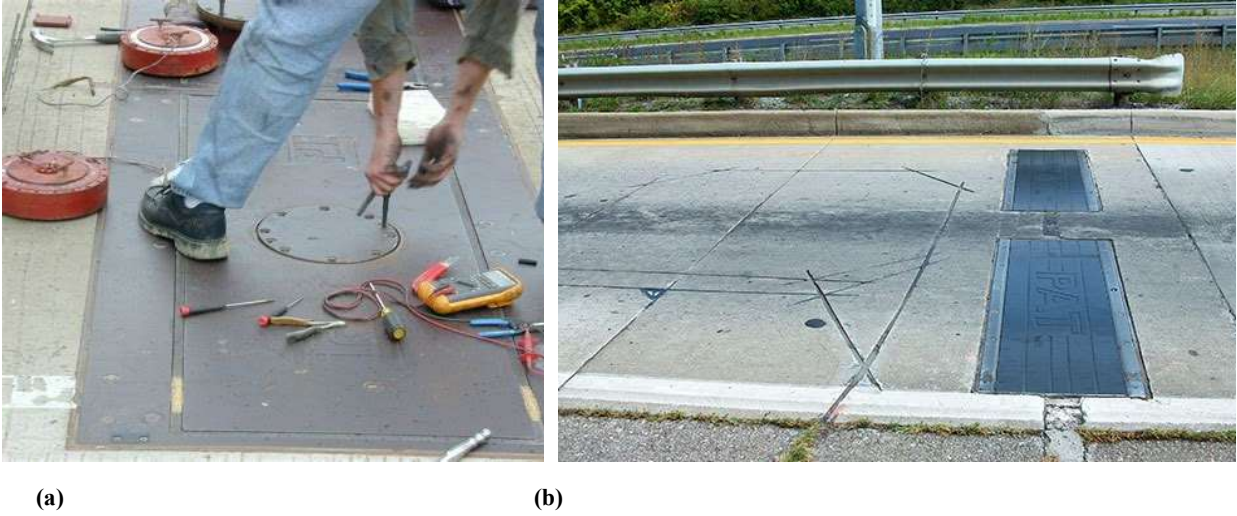


Figure 3. Instrumented Plate WIM sensor examples (a) Load cell (b) Bending plate.

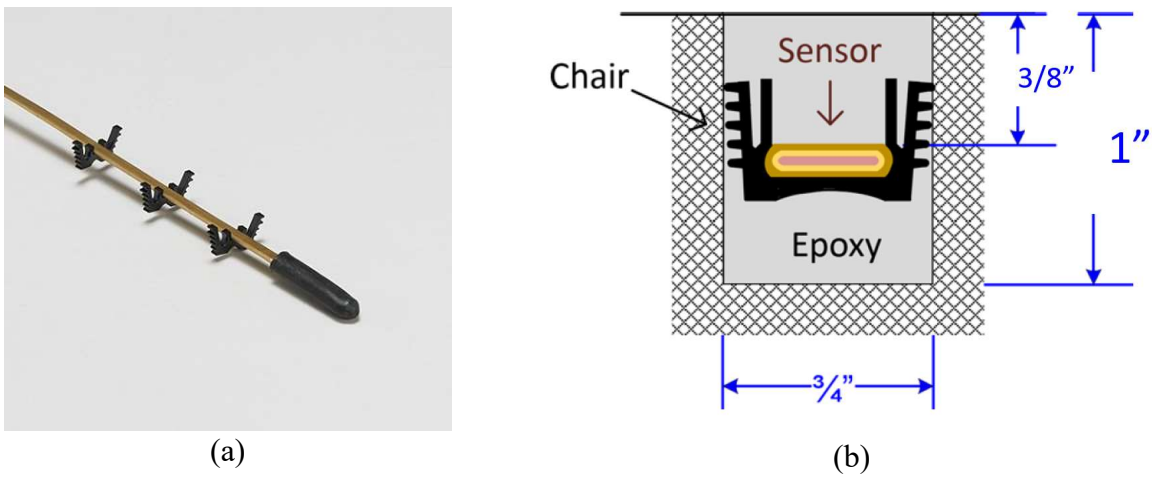


Figure 4. a) Polymer piezo sensor b) Polymer piezo installation schematic.

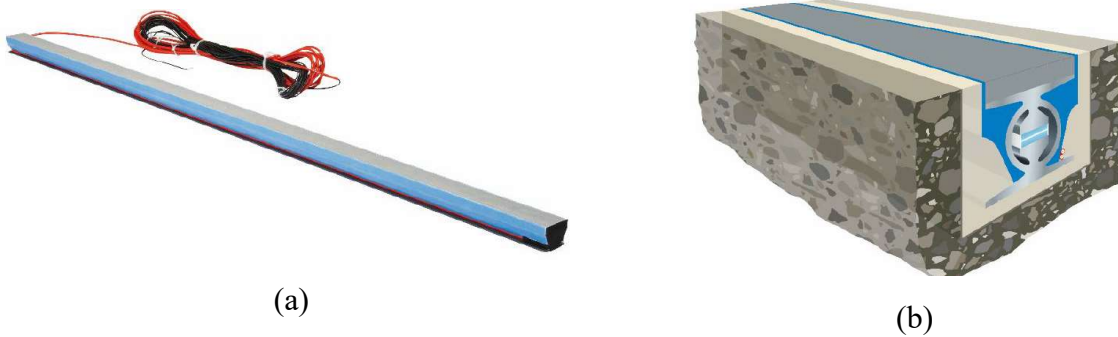


Figure 5. a) Quartz piezo sensor b) Quartz piezo installation schematic.

WIM system performance is evaluated according to ASTM Standard E1318-09(2017), entitled *Standard Specification for Highway Weigh-In-Motion (WIM) Systems with User Requirements and Test Methods* (3). Load measuring accuracy is evaluated with reference to the static load of vehicles. This makes WIM accuracy a function of pavement roughness and vehicle dynamics/speed. Accordingly, this standard classifies WIM systems into four types based on their accuracy characteristics. Table 1 lists the error confidence intervals in measuring static axle loads at a confidence of 95% for the first three WIM types. The fourth type is not listed because it relates to the use of WIM systems for direct load enforcement, which has not been approved in the United States. WIM Type I and Type II are suitable for traffic data collection. It is noted that Type I WIM systems have sensors that capture the loads applied on a single wheel path (e.g., using strip sensors that are 5 feet long), while Type II systems provide load measurements of entire axles by covering both right and left wheel paths (e.g., using one plate in each wheel path or strips that are 10 feet long). This standard defines less strict accuracy requirement for WIM Types I and II for vehicle speeds ranging between 10 and 80 mph. The accuracy requirements for Type III systems is more stringent because they are intended for enforcement screening purposes over the same speed ranges. Load enforcement screening is used on heavily trafficked roadways to identify vehicles that are likely to be overloaded so they can be stopped and weighed on static weigh scales.

These conventional WIM systems represent a sizeable investment for equipment purchase, installation, site preparation, and maintenance. As an example, a 4-lane WIM system with Lineas® quartz piezo sensors manufactured by *Kistler Instrument AG* costs around \$133k. This cost includes \$99k for four sets of sensors, \$26k for the controller and \$8k for the installation grouts (4).

Table 1. WIM system types based on their accuracy tolerances (3)

Accuracy tolerance in measuring:	Type I	Type II	Type III
Wheel Load	±25%	-	±20%
Axle Load	±20%	±30%	±15%
Axle Group Load	±15%	±20%	±10%
Gross Vehicle Weight	±10%	±15%	±6%
Vehicle Speed	±1.6 km/h or ±1 mph		
Axle Spacing	±0.15 m or ±0.5 ft		

As a result, there is a need for a less expensive WIM system that is affordable enough to install in many more locations throughout a roadway network. Furthermore, it would be advantageous to operate such systems independently of the electrical power grid. The report at hand documents the development of such a WIM system that utilizes piezoelectric elements for sensing axle loads and it is powered by harvesting the mechanical energy of the vehicles being weighed. Its data acquisition system is an ultra-low power MCU that can be operated by the energy harvested.

1.3 Piezoelectric Materials as Sensors and Harvesters

Piezoelectric materials can be found naturally or synthetically manufactured. The synthetic piezoelectric materials include, quartz, ceramic, polymer or composite crystals (5). Two of the

most common piezoelectric materials are Lead Zirconate Titanate (PZT) and Polyvinylidene Fluoride (PVDF). PZT is in the piezo-ceramic family, and PVDF is a polymer. Each piezoelectric material has different parameters that affect its performance and efficiency. PZT is an inorganic fragile ceramic material with a high piezoelectric coefficient. On the other hand, the PVDF is a polymer composite with excellent flexibility, thermal stability and chemical resistance, but it has a lower piezoelectric coefficient (6).

There is an abundance of literature describing the use of piezoelectric materials as sensors and harvesters, as described in detail in the Literature Review (i.e., Section 3 of this Report). An example of using piezoelectric elements as sensors for roadway applications is the work by (7). They used the voltage output of a strip piezoelectric sensor to estimate tire loads. Two algorithms were used for this purpose. The first utilized the peak voltage output and an adaptive footprint tire model that translated the peak voltage to load as a function of the radius of the tire imprint. The second algorithm utilized a relationship between the normalized integrated voltage (i.e., area under the voltage as a function of time curve) versus tire load relationship. The latter required no assumptions as to the size of the tire imprint and produced more accurate results. The field tests conducted involved tire loads ranging from 14 to 28 kN and vehicle speeds ranging from 30 km/h to 100 km/h.

Piezoelectric energy harvesters (PEH) consist of two main components, a mechanical system for carrying external load input to the PZTs and an electrical circuit for conditioning the electrical output. The configuration and integration of these two elements have a significant effect on device efficiency (8). Effective energy harvesting in pavements requires piezoelectric devices that satisfy stringent requirements for stiffness, durability and strength. To protect piezoelectric elements from vehicular loads and adverse environment conditions, they need to be encased in a properly designed enclosure made of suitable materials, such as concrete, steel or engineered plastic (9). Another example utilizing piezoelectric elements as pavement health monitoring sensors was described by Michigan State University (10) (11). They developed a miniaturized, self-powered, batteryless strain sensor that can be embedded into the asphalt concrete layer, monitor the number of strain cycles by strain level and wirelessly transmit the results to a road-side receiver.

There is also an abundance of literature on utilizing piezoelectric elements for mechanical energy harvesting that can power low consumption roadside lights, signage or data collection systems (12). The electrical energy generated by piezoelectric harvesters is relatively low, so it is necessary to store it in order to power infrastructure applications (13). There are two methods to store electrical energy, namely using supercapacitors or rechargeable batteries (14). Sodano et al. (2005) found that rechargeable batteries perform better than traditional capacitors when a constant power was needed. Results showed compatibility between the battery and the piezoelectric devices and a charge of 40 mAh was obtained from the piezoelectric device in less than an hour (15). Xiong (2015) studied the applicability of rechargeable batteries to store the energy generated from piezoelectric devices. According to their results, the charging speed of the battery was initially high. However, subsequently, the charging rate dropped drastically until the battery got fully charged (16).

2 OBJECTIVES

The introduction presented in previous section suggests that there is a need for many more WIM installations than currently State highway agency can afford to install and operate. It also indicates that piezoelectricity technology shows promise for both load sensing and powering of such systems. This report describes the development of such a WIM system. Its goal is to create an inexpensive and self-powered WIM system equipped and driven by piezoelectricity. Its particular objectives are to:

- Characterize the electro-mechanical behavior of piezoelectric elements,
- Develop electronics to condition and maximize the power output under the loading conditions anticipated under in-service roadway traffic,
- Develop algorithms and software for conditioning the load sensing signal and processing it into the output produced by conventional WIM systems, yielding axle loads, vehicle speed and vehicle classification for each passing vehicle and,
- Integrate these elements into a prototype system that can be installed on the roadway surface.

It is noted that this development builds upon work on energy harvesting carried out earlier (17) (18).

3 LITERATURE REVIEW

3.1 Theory of Linear Piezoelectricity

The piezoelectric materials are crystalline materials found in nature or synthetically produced. The natural piezoelectric crystals are both present at the surface or deep within the earth such as clear quartz and amazonite (19). Piezoelectric materials exhibit electric polarization when they are mechanically strained. Their electric polarization is proportional to the applied strain. This phenomenon is called “direct piezoelectric effect” which was discovered by the Curie brothers in 1880 (20). There is also the “inverse piezoelectric effect” where a piezoelectric material strains when it is subjected to an electric field. These two effects are interrelated, however electricity generation under strain is of primary interest for mechanical energy harvesting.

Currently, piezoelectric materials are produced synthetically for engineering applications. The most popular piezoelectric ceramic is lead zirconate titanate which is commonly known as PZT which was developed at the Tokyo Institute of Technology in 1950s (20). PZT crystals have high material strength and long service life. They are also resistant to humidity and temperatures well over 100 °C. Moreover, they can be fabricated easily to various shapes (19).

For a linear piezoelectric continuum, the sum of mechanical and electrical work in differential form follow the principle of energy conservation (20):

$$\dot{U} = T_{ij}\dot{S}_{ij} + E_i\dot{D}_i \quad [1]$$

where, the over-dots represent derivatives with respect to time, U is the stored energy density of the piezoelectric continuum, T_{ij} is the stress tensor, S_{ij} is strain tensor, E_i is the electric field tensor and D_i is the displacement vector. Electric displacement is defined as the charge per unit area that would be displaced across a conductor when exposed to an electric field.

Stress and strain are 2nd order symmetric tensors, which in Voigt's notation can be written as vectors with 6 components:

$$\begin{bmatrix} S_1 \\ S_2 \\ S_3 \\ S_4 \\ S_5 \\ S_6 \end{bmatrix} = \begin{bmatrix} S_{11} \\ S_{22} \\ S_{33} \\ 2S_{23} \\ 2S_{13} \\ 2S_{12} \end{bmatrix}, \quad \begin{bmatrix} T_1 \\ T_2 \\ T_3 \\ T_4 \\ T_5 \\ T_6 \end{bmatrix} = \begin{bmatrix} T_{11} \\ T_{22} \\ T_{33} \\ T_{23} \\ T_{13} \\ T_{12} \end{bmatrix} \quad [2]$$

Different types of thermodynamics potentials are used in order to derive the piezoelectric constitutive equations which yield different sets of constitutive equations. There are several energy components including the internal energy, $U = U(S_{ij}, D_i)$, elastic Gibbs energy, $G_1 = G_1(T_{ij}, D_i)$, Gibbs free energy, $G = G(T_{ij}, E_i)$, Helmholtz free energy, $F = F(\sigma_{ij}, D_i)$ and finally the electric Gibbs energy or electric enthalpy, $H = H(S_{ij}, E_i)$ (5). The electric Gibbs energy or electric enthalpy density is given by:

$$H = U - E_i D_i \quad [3]$$

Taking the derivative of the [3] gives:

$$\dot{H} = \dot{U} - \dot{E}_i D_i - E_i \dot{D}_i \quad [4]$$

By substituting [1] into [4]:

$$\dot{H} = T_{ij} \dot{S}_{ij} - D_i \dot{E}_i \quad [5]$$

From Equation [5], it is concluded that strain and electrical field are independent variables, i.e., $H = H(S_{ij}, E_i)$. Furthermore, this equation suggests that stress and electrical displacement, T_{ij} and D_i are the dependent variables, respectively. In other words, one can write (5) and (20):

$$\dot{H} = \left(\frac{\delta H}{\delta S_{ij}} \right)_E \dot{S}_{ij} + \left(\frac{\delta H}{\delta E_i} \right)_s \dot{E}_i \quad [6]$$

By comparing [5] and [6] the following relationships can be obtained:

$$T_{ij} = \left(\frac{\partial H}{\partial S_{ij}} \right)_E, \quad D_i = - \left(\frac{\partial H}{\partial E_i} \right)_s \quad [7]$$

The subscripts E and s in Equation [7] denote that the electric field and the strain are constant, respectively.

For linear piezoelectricity, the electric enthalpy density is given by:

$$H = \frac{1}{2} c_{ijkl}^E S_{ij} S_{kl} - e_{kij} E_k S_{ij} - \frac{1}{2} \varepsilon_{ij}^S E_i E_j \quad [8]$$

Where c_{ijkl}^E the elastic stiffness, is constant evaluated under a constant electric field, e_{kij} is the piezoelectric constant or piezoelectric coefficient and ε_{ij}^S is the permittivity constant evaluated at constant strain. Using Equations [7] and [8] and the convention $\partial S_{ij} / \partial S_{ji} = \delta_{ij}$ (where δ_{ij} is the Kronecker delta with values of 1 or 0 for $i = j$ and $i \neq j$, resp.), gives the linear constitutive equations for an unbound piezoelectric continuum:

$$T_{ij} = c_{ijkl}^E S_{kl} - e_{kij} E_k \quad [9]$$

$$D_i = e_{ikl} S_{kl} + \varepsilon_{ik}^S E_k \quad [10]$$

An alternative form of piezoelectric constitutive equations are:

$$S_{ij} = s_{ijkl}^E T_{kl} + d_{kij} E_k \quad [11]$$

$$D_i = d_{ikl} T_{kl} + \varepsilon_{ik}^T E_k \quad [12]$$

Where d_{kij} is alternative form of piezoelectric constant and s_{ijkl}^E is the elastic compliance. Generally, the electric field can be applied on three orthogonal coordinate axes. In isotropic materials, the electrical displacement will be along the applied electric field but for piezoelectric ceramics which are not isotropic this is not true. In this case, the displacement (D) and the electric field (E) are 3×1 vectors and the dielectric permittivity (ϵ) is a 3×3 matrix. A longitudinal stress on a piezoelectric cylinder will not only make the cylinder shorter and thicker, but also make the cylinder rotate around its longitudinal axis which will not be the case in an isotropic material. In order to describe this behavior, 21 independent stress and strain coefficient are needed. The stress, T , and strain, S , in piezoelectric constitutive equations are 6×1 and c is a 6×6 matrices (21).

3.2 Piezoelectric Electromechanical Model

The model that will be described was developed for piezoelectric materials working in “33” mode, that is for stresses parallel to the direction of polarization (22). Lumped parameter modelling is a common way to develop analytical models for predicting piezoelectric behavior. Piezoelectric ceramics are usually used or manufactured in a way that only one or two strain coefficients define their piezoelectric performance, while the others can be neglected. Platt et al. (21) developed a model by reducing Equations [11] and [12] and assuming a “33” loading mode, as follows:

$$S = s_{33}^E T + d_{33} E \quad [13]$$

$$D = d_{33} T + \epsilon^T E \quad [14]$$

Equations [13] and [14] can be rewritten as:

$$\frac{\Delta t}{t} = s_{33}^E \frac{F}{A} + d_{33} \frac{V}{t} \quad [15]$$

$$\frac{Q}{A} = d_{33} \frac{F}{A} + \epsilon^T \frac{V}{t} \quad [16]$$

Where t is the thickness of the material and Δt is the change in thickness. V is the voltage and F is the applied force in Volts and Newtons, respectively. Considering a sinusoidal operating condition, differentiating equations [15] and [16] with respect to time and transforming them into frequency domain with Laplace transform lead to:

$$v = j\omega C_m F + j\omega d V \quad [17]$$

$$i = j\omega C_p V + j\omega d F \quad [18]$$

Where:

$$v = \text{velocity} = \frac{d\Delta t}{t} \left[\frac{m}{s} \right]$$

$$i = \text{current} = \frac{dQ}{dt} \left[\frac{C}{s} \right]$$

$$C_m = \text{short circuit compliance} = \frac{s^E t}{A} \left[\frac{m}{N} \right]$$

$$C_p = \text{free capacitance} = \frac{\epsilon^T A}{t} \left[\frac{C}{V} \right]$$

The circuit shown in Figure 6 represents the relationships described by Equations [17] and [18]. The mechanical and electrical sides in Figure 6 are coupled with an ideal transformer with a transformer ratio of ϕ which can be determined by Equation [19]:

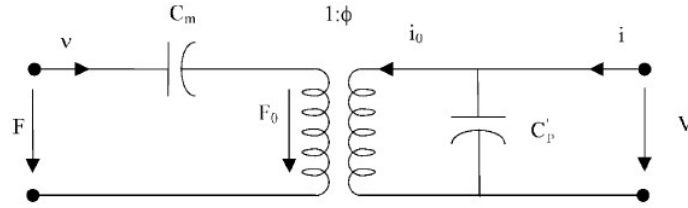


Figure 6. Piezoelectric coupling representation for low frequencies.

$$\phi = -\frac{C_m}{d} = -\frac{s^E t}{Ad} \quad [19]$$

The mechanical and electrical properties of piezoelectric materials changes with load and frequency (21). Based on Equation [16] when the stress is zero, the charge generated by an applied voltage is given by:

$$Q = \frac{\epsilon^T A}{t} V = C_p V \quad [20]$$

And when the displacement is constrained to zero ($\frac{\Delta t}{t} = 0$) Equations [15] and [16] become:

$$Q = \left(1 - \frac{d^2}{s^E \epsilon^T} \right) \frac{\epsilon^T A}{t} V = \left(1 - \frac{d^2}{C_m C_p} \right) \frac{\epsilon^T A}{t} V = (1 - k^2) C_p V = C_p' V \quad [21]$$

Where $\frac{d^2}{C_m C_p} = k^2$ is called the coupling factor. C_p' is called blocked capacitance.

The governing equation of motion of a piezoelectric element can be derived from the lumped parameter model of the material as shown in Figure 7.

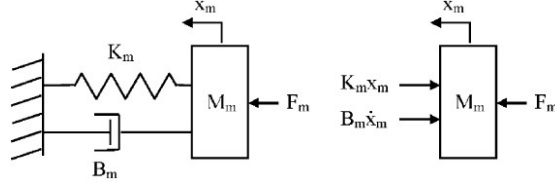


Figure 7. Mechanical model of a vibrating mass.

The equation of motion of the free body diagram shown in Figure 7 is given by:

$$F_m(t) = M_m \ddot{x}_m(t) + B_m \dot{x}_m(t) + K_m x_m(t) \quad [22]$$

Mechanical impedance is analogous to electrical impedance when force is analog of voltage and the velocity is analog of current. Therefore, as the ratio of voltage to current is defined as electric impedance, the ratio of force to velocity is the mechanical impedance which like the electrical impedance is a complex value and change with input force frequency (23). Equation [22] in terms of speed becomes:

$$F_m(t) = M_m \dot{v}_m(t) + B_m v_m(t) + K_m \int_0^t v_m(t) dt \quad [23]$$

Taking the Laplace transform of Equation [23] and assuming the initial condition is zero because of the steady state:

$$F_m(s) = sM_m v_m(s) + B_m v_m(s) + \frac{K_m}{s} v_m(s) \quad [24]$$

Substituting s with $j\omega$ where ω is radian frequency:

$$\frac{F_m(s)}{v_m(s)} = j\omega M_m + B_m + \frac{K_m}{j\omega} \quad [25]$$

As discussed earlier, the ratio of force to the velocity is the mechanical impedance. Incorporating Equation [25] and considering the ideal piezoelectric representation in Figure 6, the electromechanical model can be further developed as illustrated in Figure 8.

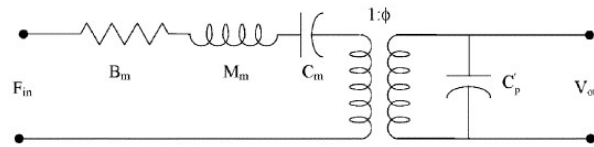


Figure 8. Piezoelectric electromechanical model.

The mechanical properties of the piezoelectric can be converted to analogous equivalent electrical components properties using the transformer ratio, Φ . The equivalent electrical circuit component properties are given by Equations [26] through [30] and an illustration of it is presented in Figure 9.

$$R_{em} = \phi^2 B_m \left(\frac{V^2}{N^2} \right) \left(\frac{N \cdot S}{m} \right) = \left(\frac{V \cdot S}{C} \right) [Ohms] \quad [26]$$

$$C_{em} = \frac{1}{\phi^2 K_m} = \frac{C_m}{\phi^2} \left(\frac{N^2}{V^2} \right) \left(\frac{m}{N} \right) = \left(\frac{C}{V} \right) [Farads] \quad [27]$$

$$L_{em} = \phi^2 M_m \left(\frac{V^2}{N^2} \right) (kg) = \left(\frac{V \cdot S^2}{C} \right) [Henries] \quad [28]$$

$$V_{in} = \phi F_{in} \left(\frac{V}{N} \right) (N) = V [Volts] \quad [29]$$

$$C'_p = (1 - k^2) C_p \left(\frac{C}{V} \right) [Farads] \quad [30]$$

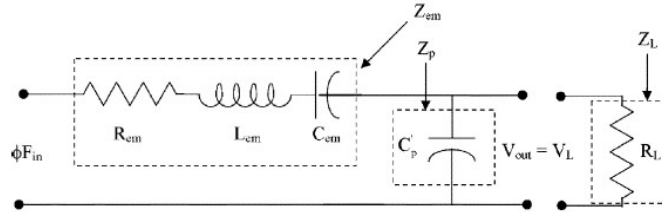


Figure 9. Equivalent electrical circuit of a piezoelectric element at low frequencies (21).

It should be noted that this model is only valid at low frequencies which are below the first resonant mode of PZTs. Also, piezoelectric constants change with excitation force amplitude and frequency and mechanical and electrical boundary conditions in a non-linear fashion (21). The Z_{em} , Z_p and Z_L in Figure 9 are impedances or equivalent impedances of various circuit components and they are given by:

$$Z_{em} = j\omega L_{em} + \frac{1}{j\omega C_{em}} + R_{em} \quad [31]$$

$$Z_p = \frac{1}{j\omega C'_p} \quad [32]$$

$$Z_L = R_L \quad [33]$$

$$Z_{par} = \frac{Z_p Z_L}{Z_p + Z_L} \quad [34]$$

$$Z_{tot} = Z_{em} + Z_{par} \quad [35]$$

The model calculates the output voltage measured across an electrical load, R_L , using:

$$V_L = V_{in} \frac{|Z_{par}|}{|Z_{tot}|} = \phi F_{in} \frac{|Z_{par}|}{|Z_{tot}|} \quad [36]$$

3.3 Piezoelectric Energy Harvesting (PEH) Fundamentals

There has been a multitude of piezoelectric energy harvesting applications. Piezoelectric materials have been used for energy harvesting by embedding them in wearables like shoes and backpacks, where they are powered from human movements (24). Typical output from PZT wafers embedded in shoes was 1.3 mW at 3 V from walking at a rate of 0.8 Hz (21).

Another application is their use in powering micro-electro-mechanical systems (MEMS), often without the need for storage batteries. This is highly desirable where accessing/replacing batteries is problematic, such as remote and hard to reach sensor nodes, safety-monitoring devices, embedded sensors and so on (25). These proposed battery-less solutions eliminate batteries and the associated manufacturing and disposing environmental costs. However, not all studies agreed that efficient PEHs are possible without storing the harvested energy in a rechargeable battery. The energy produced by PEHs is typically low to directly power some electrical systems. In such cases, there is a need to accumulate the electrical power using a capacitor or a rechargeable battery. Capacitors are not the best choice for electrical storage, since they supply short bursts of high electrical power before they totally discharge (15). A study demonstrated that a 40 mAh battery can be successfully charged in a relatively short time from vibrations generated by a typical piece of machinery (15).

A piezoelectric harvester differs from a typical electrical power source because its internal impedance is capacitive rather than inductive in nature (26). Piezoelectric generators development is further confounded by the high voltages and low currents they produce, which results in low power output, while they exhibit high internal impedances. Regardless, this is a high value area of research because several newly developed technologies, such as sensors and MEMS, have low power consumption requirements (21).

When a piezoelectric element is loaded and then unloaded the polarity of the output voltage changes signs from positive to negative or vice versa, hence generating an AC current. To regulate this output and make it suitable for harvesting, it needs to be converted to DC current. This is done through a bridge rectifier (Figure 10). In addition, a capacitor is added to smoothen the DC output. A resistance is also added to represent the external electrical load of the system (Figure 11).

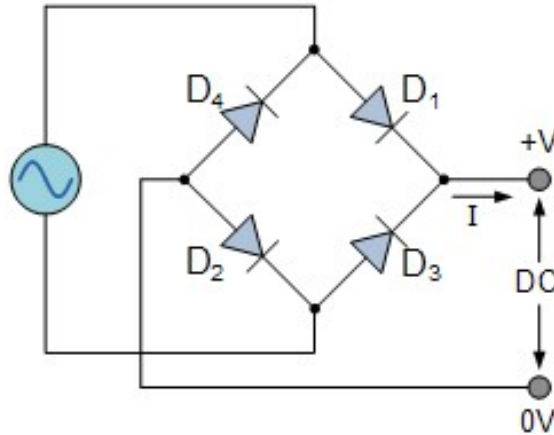


Figure 10. A bridge rectifier built with four diodes translates AC current into DC (https://www.electronicstutorials.ws/diode/diode_6.html).

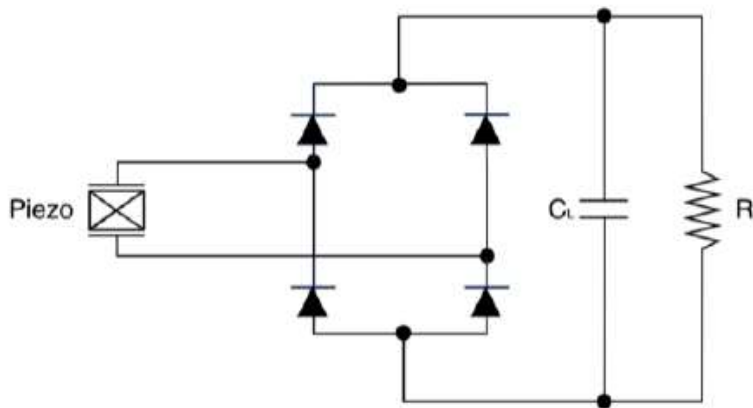


Figure 11. Circuit interface for piezoelectric energy harvesting (27).

Piezoelectric generators usually work in “33” or “31” modes (Figure 12). The mechanical to electrical energy conversion efficiency of the “33” mode is 3 to 5 times higher than that of the “31” mode (28). A piezoelectric structure in “33” mode can produce twice the electrical charges compared to one with the same dimensions in “31” mode (28). However, the stiffness of piezoelectric materials is much higher in the poling direction. As a result, energy harvesting applications that rely on vibration favor the “31” mode especially where loads are low.

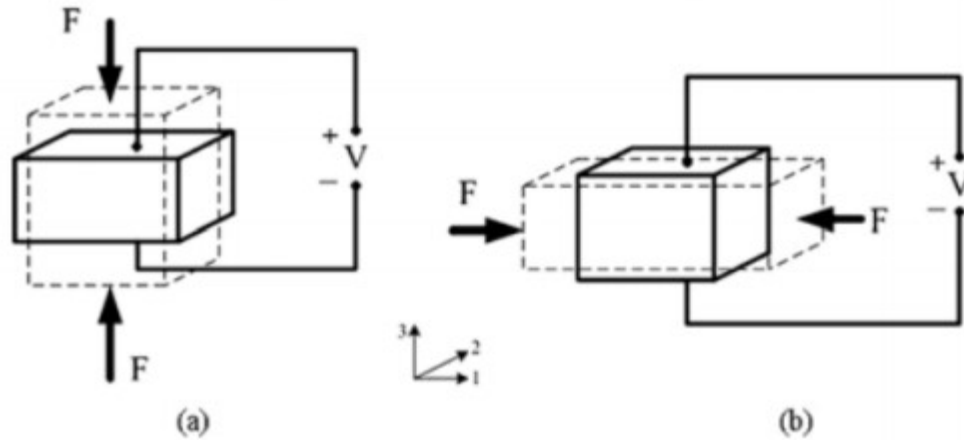


Figure 12. Piezoelectric structure a) 33 mode b) 31 mode (22).

3.4 PEH Applications in Pavements

Table 2 provides an overview of recent efforts to develop PEH applications for roadway pavements. It summarizes the piezoelectric material used, the way they were tested, their electrical output and the conclusions drawn by each study.

Table 2. Literature overview of PEH applications for pavements.

Study	Specimen materials and design	Test	Electric output	Study Conclusions
(29)	PZT ceramics plate fixed to box- piezoelectric sensors at road and railway tunnels cantilever-based piezoelectric generator	In field, under real traffic of railways and roadways loads	showed output energy from railway vibration, at least 135 μ J from 85% of all trains, was higher than road tunnels output	Vehicle vibrations at any location in the road across the pavement and tunnels walls were not enough for energy harvesting. Harvesting the vibrations using more cantilevers can be a solution to increase the output energy.
(30)	Lead Zirconate Titanate (PZT) - Arc and Trapezoidal bridge transducers	Universal Testing Machine (UTM) under different loads and frequencies	232 V for arc bridge and 106 V for trapezoidal	Piezoelectric technology in roadways is practical.
(31)	PZT- some cantilevers plates installed in a speed bump device and underneath of a pavement layer	In field with real vehicle road	7.61 mW for speed bump device and 63.90 mW for underneath device	Increasing the number of piezoelectric cantilevers is useful to generate more energy.
(32)	PZT material- circle plate	Direct compression test	2.43 mW and 1.6V for voltage	Output power was very low. It can be improved by changing the size and network connection of transducers.
(33)	PZT-5H – multilayer stack	Horizontally compressed by a long-stroke shaker at low frequency	0.6 mW/cm ³	Introduce of analytical and numerical tools to predict piezoelectric harvester performance.
(9)	PZT - disk-shape with nine different configuration	Material Testing System (MTS)	3.1 mW electrical energy per passing vehicle	The generated power decreased significantly after one year of operation.

				The product is suitable for small electronics infrastructure
(8)	PZT-8 - device that consisted groups of piezoelectric units including three multilayer stacks	Using shake table to input the vibration excitations	one single unit 85 mW DC power	The output energy was sufficient to power a low-power equipment.
(34)	PZT and phosphor- bronze end cap - Arc and rectangular bridge transducer	MTS provided the necessary half-sine wave load with frequencies of 1Hz and 5Hz and amplitude of 0.1MPa~0.7MPa for the experiment	Arc transducer generated 220 V while the rectangular transducer produced 160 V	The rectangular transducer could tolerate higher stress than the arc bridge.
(35)	PZT-PZNM ceramic attached to a stainless steel - piezoelectric cantilever beams	UTM under different loads and frequency	One-fourth of the harvesting module output power was 184 μ W, and power density was 8.19 mW/m ²	By installation of the prototype in a road with 600 passing vehicle per hour, 4.91 Wh/m ² electrical power could be generated.
(36)	PZT-PZNM as a piezoelectric material and stainless steel for substrate - fixed-fixed beam type piezoelectric plate in a box	Connect shaker to fixed-fixed beam to make a frequency load	112.937 V	Output voltage increased from 92.312 V to 112.937 V when the piezoelectric energy harvester's mass decreased from 6.035 g to 5.386 g.
(37)	PZT transducer	Automatic rutting test machine, the frequency is 0.7 Hz and wheel pressure is 0.7 MPa	16.8 mW	The system has the potential to improve the pavement preservation, management, and maintenance.
(38)	PZT-PZNM ceramic and stainless steel were used for piezoelectric cantilever	UTM and a third-scale mobile loading simulator (MMLS3).	625 mW for UTM test in 15 Hz loading frequency, 280 mW for MMLS3 test and about 330 mW for APT machine test, the maximum power density 21.47 W/m ²	The prototype could work as an energy source for sensors in smart roads and autonomous vehicles.
(18)	PZT- four prototype include 3 layers of PZT connected in series, a stack of 6 PZT-5A ceramic disks, 21 rectangular PZT composite of 3 of 21 rectangular PZTs	UTM loading system	The electrical power generated from a single pass of truck tire load was between 1.0 to 1.8 W	Connecting piezoelectric elements in parallel avoid generating unmanageably high voltages.
(39)	PZT- Biomorph cantilever beam	-	Generated and stored 1.68 mW power	Output was sufficient for the acceleration sensor for data collection and RF communication
(40)	PZT disks - harvesting prototype consisted of two conductive asphalt layer and one layer of piezoelectric	Simulation of traffic loads on specimens by an MTS	Maximum electrical power output was 300 mW under 30 Hz vibration frequency	More flexible conductive asphalt mixture and arranging more piezoelectric materials with higher piezoelectric stress constant increased the output electricity.
(41)	PZT-5X square plates - piezoelectric layered bridge transducers, 64 transducers in an aluminum casting in four layers	Vehicular loading was simulated using a pneumatic piston; loading pressure was 70 kPa at 5 Hz	Maximum output power was 2.1 mW at 5 Hz and 400 k Ω resistive load	The output power is greater at high resistive loads due to the high impedance of Bridge Transducers.
(17)	PZT- a piezoelectric prototype consisted of a stack of 11 piezoelectric	The durability of the prototype with APA machine	Output was 64.12 mW for each passing tire with 64 km/h	The output power remained constant throughout the loading repetition test.

	elements connected in parallel.			
(42)	PZT – the area of the device was 100mm x 100mm	MTS - 0.2 to 0.7 MPa loads were applied	Maximum output was 11.67 mW at 0.7 MPa load and 15 Hz	Maximum output power of the energy harvesting units are positively correlated to the load size and frequency
(43)	PVDF - two connected 15 × 30 × 10 cm ³ modules,	In-field test under real traffic condition	620.2mW (13.8 W/m ²) at 15 cm×30 cm ² area with a passenger vehicle at 80 km/h	The output power has a linear relation to the vehicle speed and weight.
(44)	MFC-M8514-P2 - Cantilever beam with new bandwidth – 101mm x 20mm x 0.21mm dimensions	Laboratory set up with shaker, signal generator, power amplifier and oscillograph	Maximum output power 3.277 mW under the harmonic excitation of 4 m/s ²	The harvester has a high performance by enhanced output power in wide operating frequency range.
(45)	PZT- bridge transducer with 2 mm x 32mm x 32 mm dimensions	Pneumatic system used to simulate vehicle	The output energy for a single loading cycle is 0.83 mJ	Technology can monitor traffic levels and distinguish between light vehicle and a heavy truck.
(40)	PZT - bulk piezoelectric elements inside the piezoelectric layer, including piezo cylinder, piezo curved roof, and piezo ball	MTS with 40 kN uniformly distributed over 0.2m x 0.2m	Maximum output voltage was 85 V for piezo ball configuration.	The voltage outputs from the PZ-EHPS with a rigid piezoelectric layer are generally higher than those from the PZEHPS with a flexible piezoelectric layer.
(46)	Two stacked PZT: the separation-type PZT chip structure uses a multilayer adhesive, and the integral stack co-firing structure uses a monolithic co-firing PZT	MTS applied cyclic loading, 0.7 MPa with 10 Hz	The output power was 22.80 mW	Multilayer units exhibit good structural stability and weatherability

4 METHODOLOGY

4.1 Fabricating and Testing the PEH Elements

This section describes the manufacturing and testing for the PEH elements, hence referred to as PZT stacks, which were developed for powering the traffic data collection system.

4.1.1 Harvester Prototype Fabrication

The piezoelectric disks used in fabricating the PEH stacks were manufactured by APC International, Ltd. Each disk has a thickness of 6.8 mm and a diameter of 25.1 mm. The piezoelectric material is lead zirconate titanate (PZT). The manufacturers provided the piezoelectric properties shown in Table 3, which correspond to the resonant frequency of the material (i.e., 10,000 Hz).

Table 3. Piezoelectric material properties(47) and (48).

APC Material Number	840
Navy Equivalent	Navy I
Relative Dielectric Constant (K^T)	1275
Dielectric Dissipation Factor @ 1 kHz ($\tan \delta$)	0.60
Curie Point (T_c)	325 °C
Electromechanical Coupling Factor (k_{33})	0.72
Piezoelectric Charge Constant (d_{33})	$290 \cdot 10^{-12}$ C/N
Piezoelectric Voltage Constant (g_{33})	$26.5 \cdot 10^{-3}$ Vm/N
Young's Modulus	$6.8 \cdot 10^{10}$ N/m ²

The piezoelectric disks were assembled in reverse polarity forming a column or stack and connected in parallel as shown in Figure 13. The in-parallel connection has two advantages:

- It reduces the voltage output of the stack and
- Reduces the matching impedance needed for maximizing power output.

These advantages will be made clear in describing the results of PEH laboratory testing (see section 4.1.5).

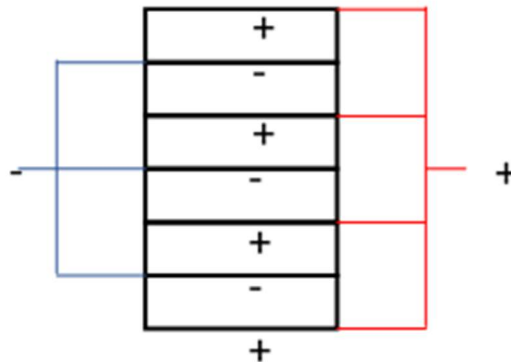


Figure 13. Piezoelectric disks are assembled into stacks connected in parallel.

Electrical connectors were fabricated from 3 mils (0.003'') copper strips sandwiched between the disks. These connectors were soldered to the piezoelectric disks using 2 mils Indium foils. In order to provide electrical insulation, for the most top and bottom electrodes a copper sheet coated with a Kapton® layer was used as electrodes. In order to provide proper bonding between the copper and Indium during the soldering process, the copper was first electroplated with Indium. The copper sheets and the Kapton® copper sheets were cut into “work” pieces as shown in Figure 14 using a CNC machine. The final electrodes which go into the stack were made by cutting these work pieces with a pair of scissors into proper shapes.

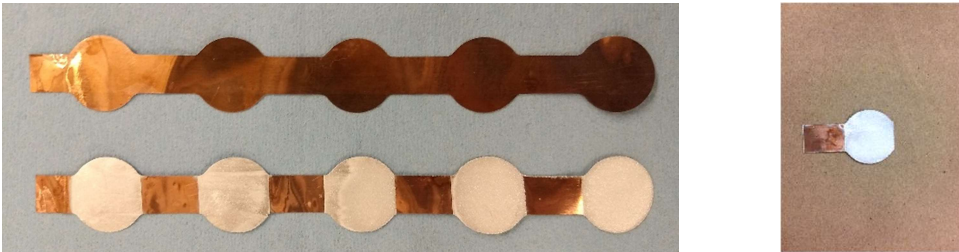


Figure 14. Copper sheet work pieces before and after electroplating. The electrodes are cut from these work pieces (right).

The first step of electroplating was to clean the copper work pieces from their surface pollutants such as grease and oxides. For this purpose, an alkaline cleaner (METKLEEN 2110) was used to clean the grease and an acidic cleaner (Citranox) was used to remove the oxides. Work pieces were placed in a tank containing the alkaline cleaner diluted to 10% at a temperature of 60°C for 20 minutes (Figure 15). After cleaning with alkaline cleaner and washing the pieces with DI water, they were placed in a tank containing 2% Citranox for around 30 minutes.



Figure 15. Work pieces resting in a 10% alkaline cleaner 60 °C tank.

According to the manufacturer’s manual which comes with Indium electroplating solution by Indium Corporation, when plating at a rate of 20 Amps/ft², it takes one hour to accumulate 1.4 mils of electroplated Indium thickness on the work pieces. Each copper work piece had an area of $\pi \cdot 1^2/4$ in², hence:

$$A_{1-side} = 5 \frac{\pi * 1^2}{4} = 3.93 \text{ in}^2 = .027 \text{ ft}^2$$

$$A_{2-side} = .027 * 2 = 0.055 \text{ ft}^2$$

$$I = 0.055 * 20 = 1.09 \text{ Amps}$$

So, the electroplating setup (Figure 16) ran for 1 hour with a current of 1 Amp for achieving 1.4 mils. For the pieces of copper at the ends of the stack (i.e., those that had Kapton® on 1 side), the current was set to 0.4 Amps to reach the same thickness.

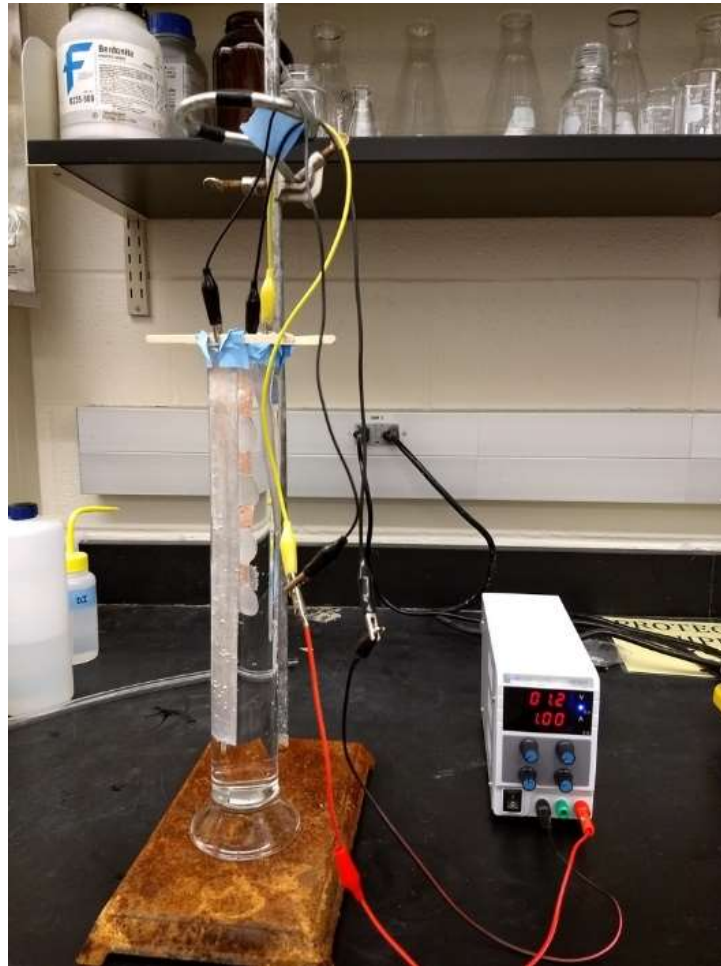


Figure 16. Electroplating setup. Notice that the current is set to 1 Amp.

As described earlier, 2 mils of Indium foils were cut into circles with diameters matching the diameter of the disks (i.e., 1 inch) then placed between the electrodes and the piezoelectric disks. Then, the stack was placed in the oven at a temperature of 175 °C for a duration of 5 hours to effect soldering. Figure 17(b) shows a piezoelectric stack after heat-soldering with the electrodes connected.



Figure 17. PEH elements (a) before soldering (b) after soldering.

4.1.2 Testing Facilities

PEH testing was carried out using a Universal Testing Machine (UTM) with a 25kN static load capacity. This is a servo-hydraulic system commonly used for material testing. It is capable of applying dynamic loads at frequencies limited by the amplitude of the load selected. Hence, at high loads, the frequencies achieved (i.e., actual) are typically lower than the ones dialed (i.e., nominal). Two types of loading functions were used for testing the PZT stacks:

- Continuous sinusoidal loading, which was maintained compressive by selecting a minimum value of 0.2 kN. An example is shown in Figure 18, which shows a maximum peak value of 11 kN. An actual load with this amplitude and frequency applied on one stack and the corresponding actuator displacement is shown in Figure 19. The figure is plotted for one period that is 0.1 sec (i.e., the frequency is 10 Hz).
- Pulsating loading, which consists of half a sine wave followed by a rest period. Figure 18(b) shows an example of such a pulse with a frequency of 10 Hz and peak values of 11 kN and minimum of 0.2 kN. The rest period between pulses is 0.9 sec. Figure 20 shows an example of such a pulsating load applied on a PZT stack. This figure also shows the corresponding displacements versus time.

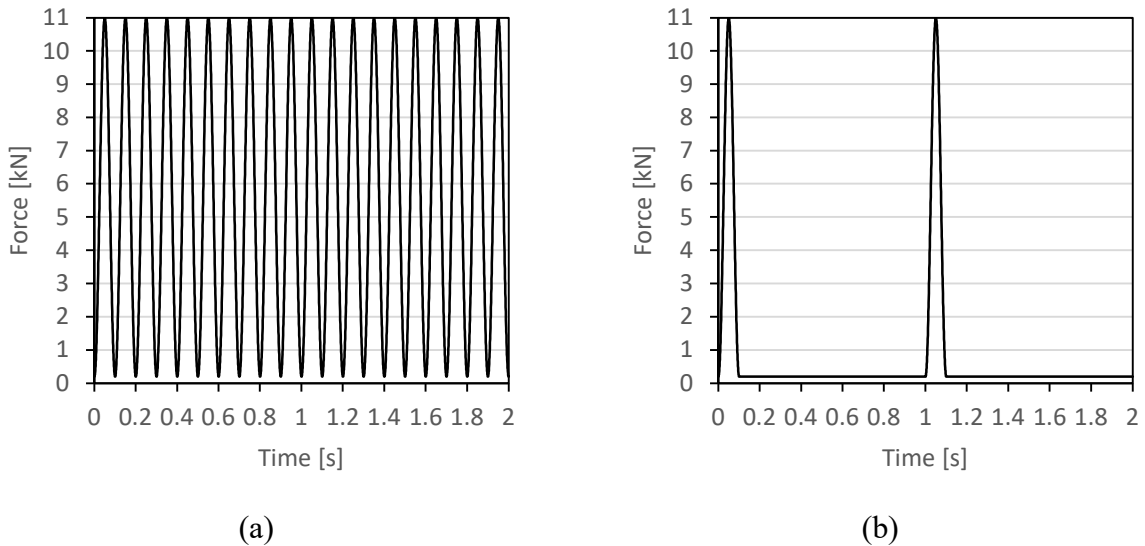


Figure 18. Types of applied mechanical load in UTM machine: a) Continuous sinusoidal loading b) Pulsating loading.

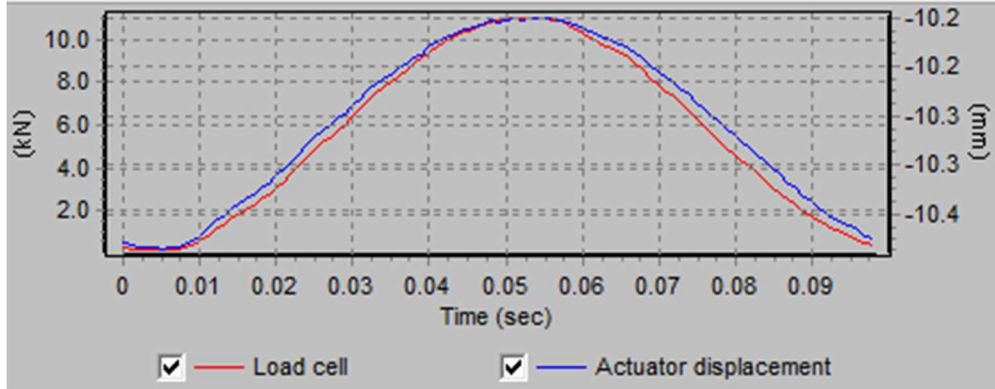


Figure 19. 10 Hz continuous sinusoidal load with an amplitude of 11 kN.

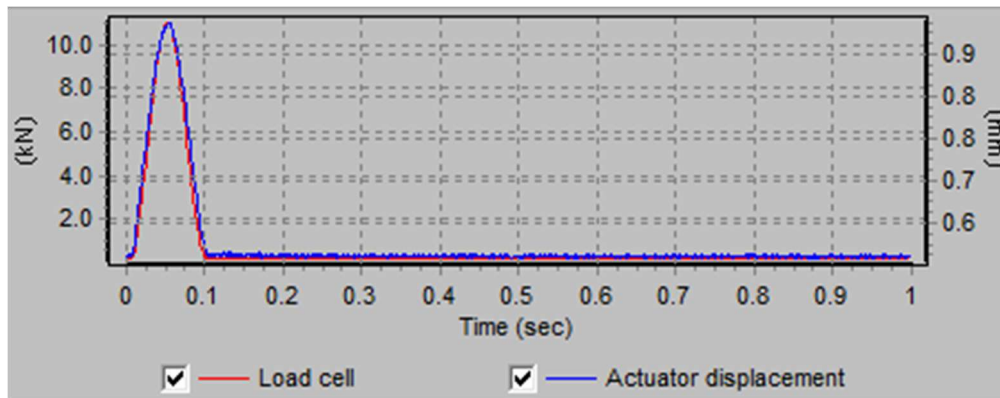


Figure 20. 10 Hz pulsating load with an 11 kN amplitude and a rest period of 0.9 sec.

Piezoelectric voltage output measurements are essential in characterizing the performance of PEHs. The data acquisition (DAQ) system used for monitoring the electrical output of the PZT stacks is important because its internal impedance affects the electrical quantities being measured (49). Early testing of the PZT stacks was carried out using a National Instruments USB 6008 DAQ connected to a laptop computer. This system had a relatively low impedance (144 kΩ) and as a result, it did not satisfy the open-circuit conditions for a DAQ device. In addition, a variable external resistance was used to provide matching impedance for maximizing the electric power output. The testing setup and the laboratory instruments used are shown in Figure 21.

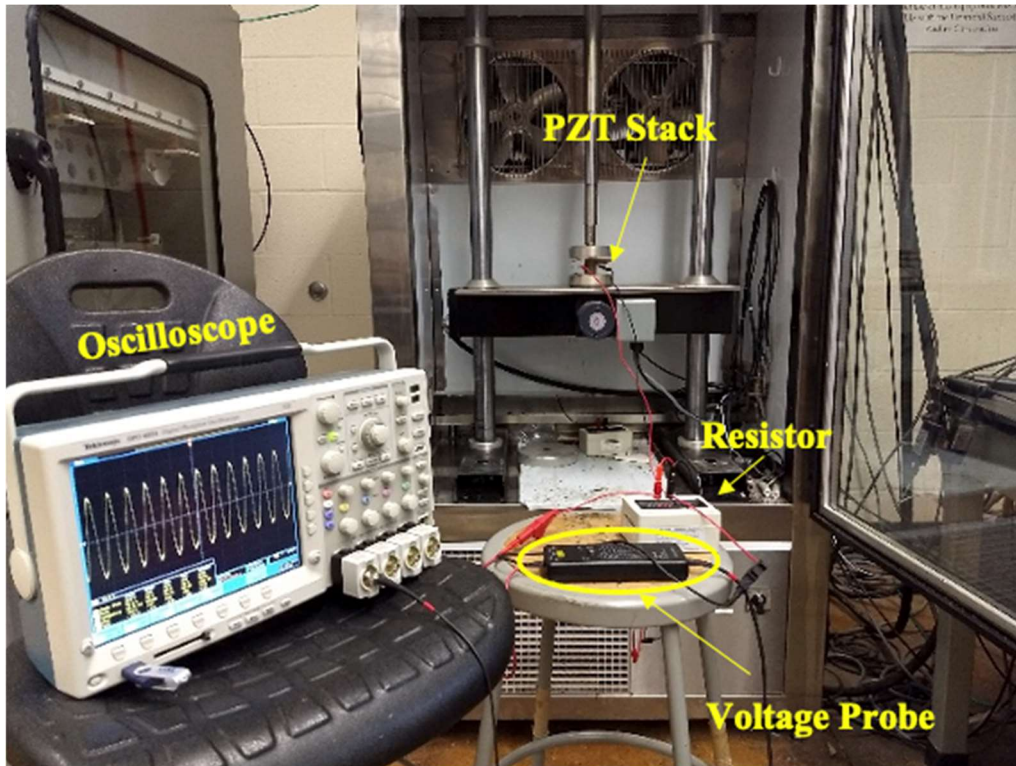


Figure 21. Laboratory setup.

Subsequent PZT stack testing was carried out using an oscilloscope (Tektronix DPO 4054) and a voltage probe with 500X attenuation rate. The reason for selecting this oscilloscope was that it had a very high internal impedance ($1\text{M}\Omega$), which effectively provided electrical measurements under open-circuit conditions.

4.1.3 Testing Isolated PZT Disks

Individual PZT disks were tested under a sinusoidal mechanical load with nominal peak values of 1.1 kN at frequencies ranging from 2.5 Hz to 62 Hz. Each disk was directly connected to the oscilloscope. The reason for conducting experiments on isolated PZT disks was to compare their output to the output of the PZT stacks. Their electromechanical behavior needed to be understood if they were to be used for sensing purposes. The voltage output signal had a sinusoidal shape with the same frequency as the excitation force. Figure 22 illustrates such a signal in the oscilloscope. As can be seen in this figure, the oscilloscope outputs voltage statistics that include the root mean square (RMS) (V_{rms}), the maximum (V_{max}) and the minimum (V_{min}) values of the signal over the time window captured. The amplitude of the voltage signal can be estimated by two methods, depending on the type of loading:

- Multiplying the V_{rms} reading by $\sqrt{2}$, assuming a sinusoidal shape for the output voltage signal or,
- Computing the voltage amplitude using $(V_{max}-V_{min})/2$.

It is noted that while both methods are possible for continuous sinusoidal loading, while only the second is possible for pulsating loading. The limitation of the latter is that there is a small variation in instantaneous V_{max} and V_{min} readings as opposed to the more stable V_{rms} statistic.

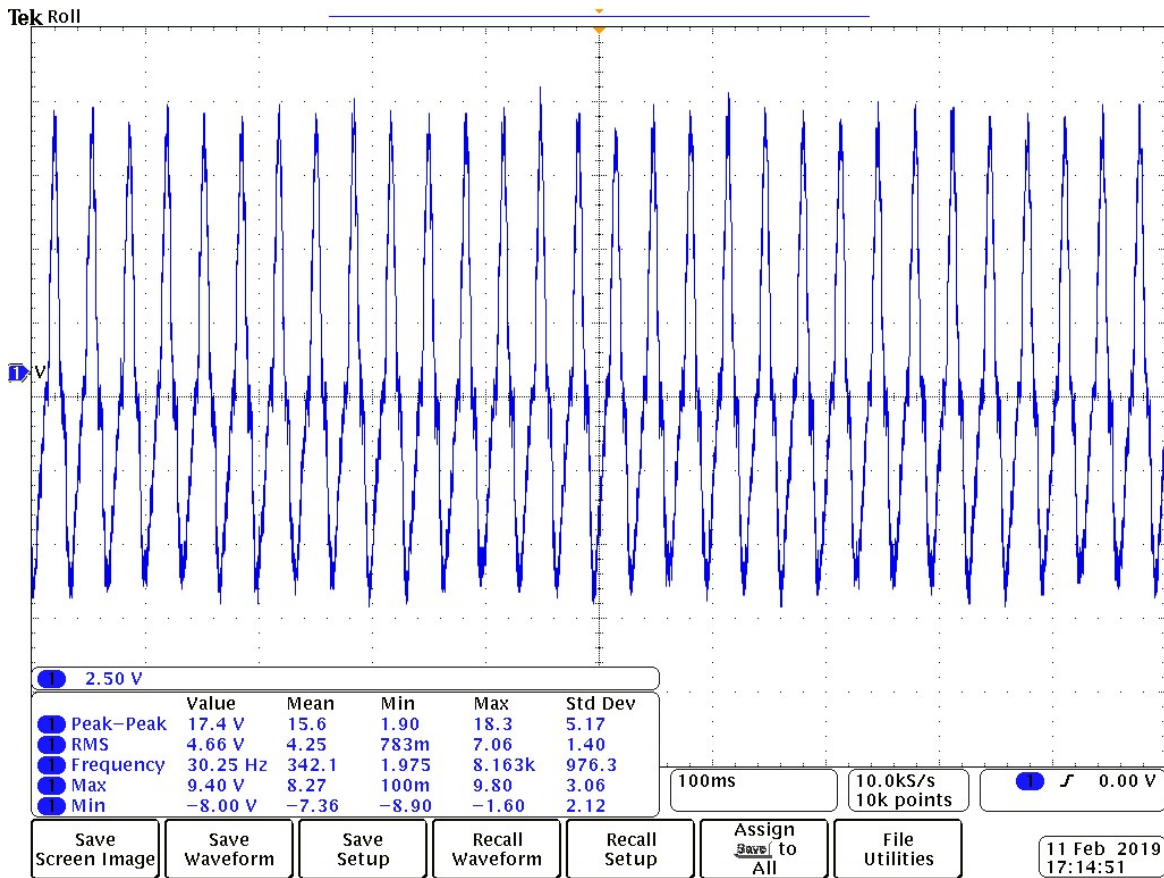


Figure 22. Example of voltage output from 30 Hz load of 1.1 kN on a single PZT element.

Figure 23 plots the voltage amplitude output for a continuous sinusoidal load with an amplitude of 1.1 kN for a range of frequencies. The signal was monitored for different electrical loads dialed in via the external variable resistor. The voltage amplitude was computed based on the two methods discussed earlier. As seen by this figure, computing the signal amplitude based on V_{rms} readings leads to slightly lower amplitudes but overall the resulting shapes of the plotted curves are similar. This difference is plotted in Figure 24 for different excitation frequencies. This difference is mainly due to the fact that the readings of V_{max} and V_{min} from the oscilloscope show the maximum value and the minimum value as opposed to the V_{rms} that is computed based on all the data points in the signal. Another reason is that min-max approach may include oscilloscope

noise. Overall, the differences between these two methods of computing voltage amplitude appear to be large for low external impedance and vice versa.

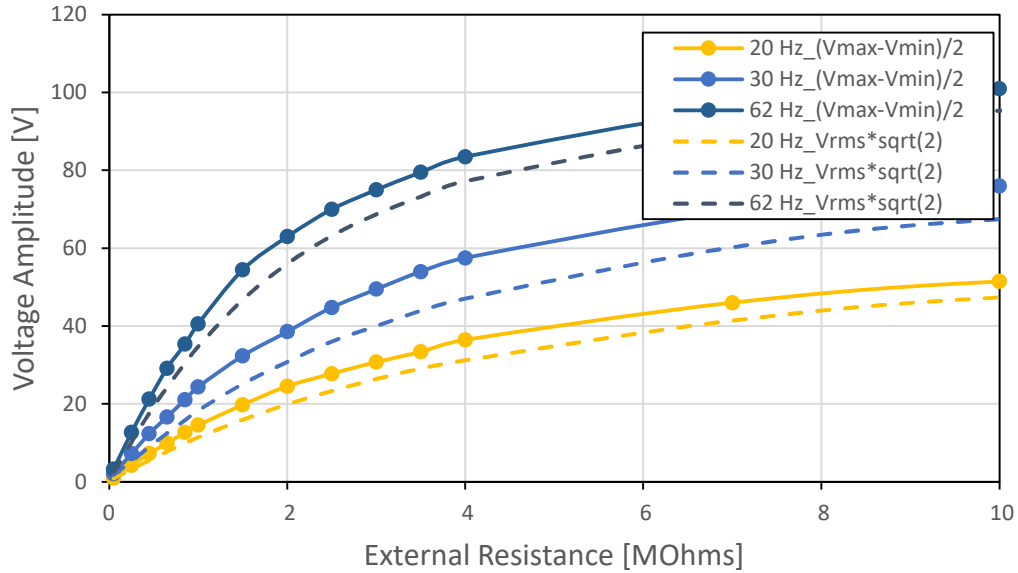


Figure 23. Voltage signal amplitudes based on two methods.

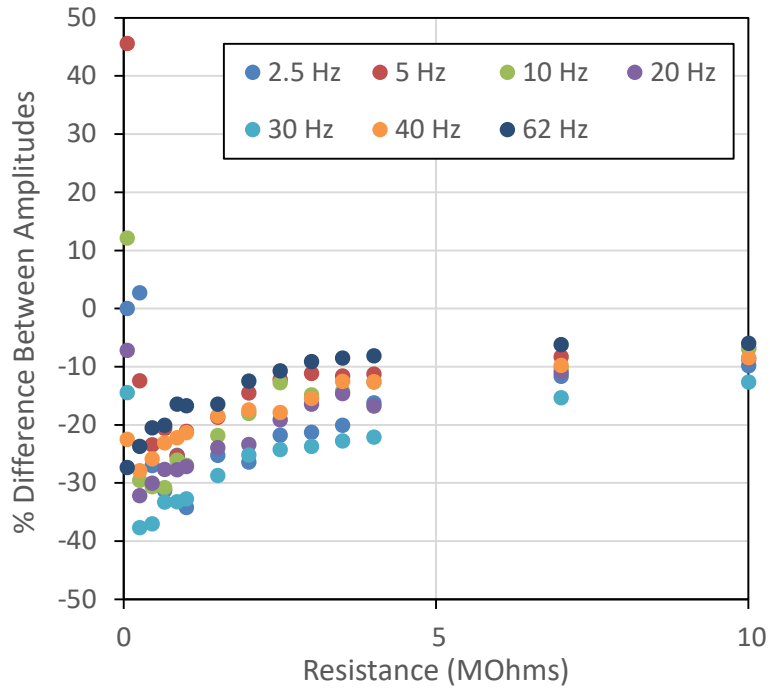


Figure 24. Percentage difference between the two methods of calculating the signal amplitude for different frequencies.

The RMS power output of the PZT disk was calculated via $P=V_{rms}^2/R_L$ by measuring the voltage across an external resistance R_L (Figure 25). This figure suggests that at higher frequencies, the

power output of a PZT disk depends on the external resistance used. This power increases drastically for stacks built by six of these disks as will be shown and discussed later.

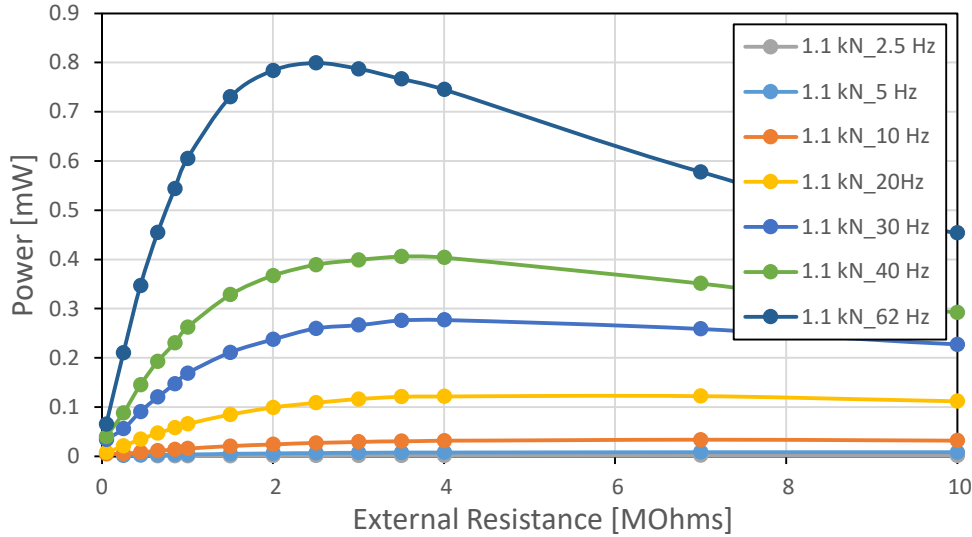


Figure 25. RMS power from one PZT disk; Sinusoidal 1.1 kN load, frequencies 2.5 Hz-62 Hz.

4.1.4 Testing Individual PZT Disks within a PZT Stack

In this section, the behavior of the top disk within a PZT stack is discussed. The rationale behind this test was to investigate the possibility of using the topmost piezoelectric element of a PZT stack for load sensing purposes, while retaining the lower 5 elements for energy harvesting purposes. The calculated loads from each sensor were added and multiplied by two to get the whole axle load (i.e., the box is designed to cover one wheel path meaning that it bears half of the axle load).

First, the test was carried out under a continuous sinusoidal load without an external rectifier connected to the PZT disk. Second, the test was carried out with a pulsating load with an external rectifier. As explained earlier, the role of the rectifier was to convert the bipolar AC voltage output to the PZT to a unipolar DC signal.

For the first trial, the mechanical load was applied in a sinusoidal continuous format. This test was mainly done in order to compare the results of one disk within the PZT stack versus those of an isolated disk which was described earlier (Section 4.1.3). The top disk within the stack was connected to the oscilloscope directly with no rectifier (Figure 26). The load was sinusoidal with a minimum value of 0.1 kN and maximum value of 1.1 kN. The loading frequency swept from 2.5 Hz to 62 Hz. The rest of the stack was connected to the same resistor that the disk was connected to. The voltage amplitudes was derived using $(V_{max}-V_{min})/2$ and was represented by Figure 28 (a). The RMS power from the top disk and the rest of the stack is plotted in Figure 29.

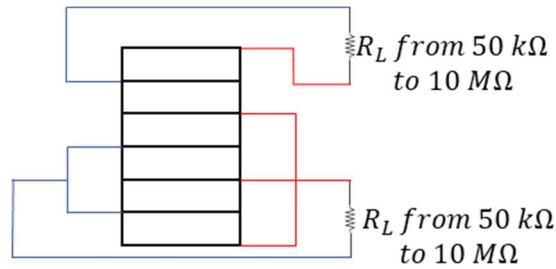


Figure 26. Test condition for top disk within the stack with sinusoidal loading.

For the second trial, the top disk was tested under a pulsating mechanical load with peak maximum value of 1.1 kN and minimum value of 0.1 kN with frequencies ranging from 2.5 Hz to 62 Hz. The disk was connected to a voltage rectifier. The rest of the 5 disks within the stack were connected to a constant resistance of 650 k Ω (Figure 27). A bridge rectifier was used to convert the AC output of the sensors to DC in order to make the signal readable by the microcontroller. This was necessary because the MCU to be used reads only positive voltage inputs.

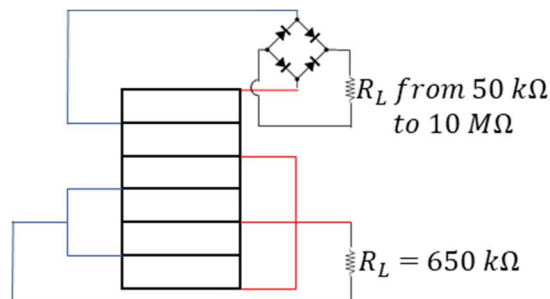


Figure 27. Test condition for top disk within the stack with pulsating loading.

The mechanical load representing light axle loads passing over the sensor consists of pulses with peaks of 1.1 kN and nominal frequencies ranging from 2.5 Hz to 62 Hz. Under pulsating load, the rectified output signal consists of two consecutive peaks. The amplitude of this signal was calculated as the average of the first and second peaks. This amplitude estimate will be used for the calibration of the model, as described under Section 4.2. The experimental data for this test are shown in Figure 28(b).

The results of the two tests are very similar as shown in Figure 28. This suggests that the PZT output is not significantly affected by the mechanical load whether it is sinusoidal or pulsating. It is also concluded that the voltage amplitude is not affected by the rectifier. By comparing the output voltage of the topmost element within the PZT stack (Figure 28), and that of an isolated disk (Figure 23), suggests that the output voltage of a disk within the stack is considerably higher than that of a completely isolated disk. For example, applying 1.1 kN load with a frequency of 62 Hz with an electrical load of 10 M Ω , the disk within the stack outputs 134 V whereas an isolated disk outputs 101 V. This shows that the rest of the stack is influencing the output of the topmost disk. The difference between these two conditions will be seen later in the development of the electromechanical models (Section 4.2). As a result, it was decided to use single PZT elements electrically isolated from the PZT stacks for sensing purposes.

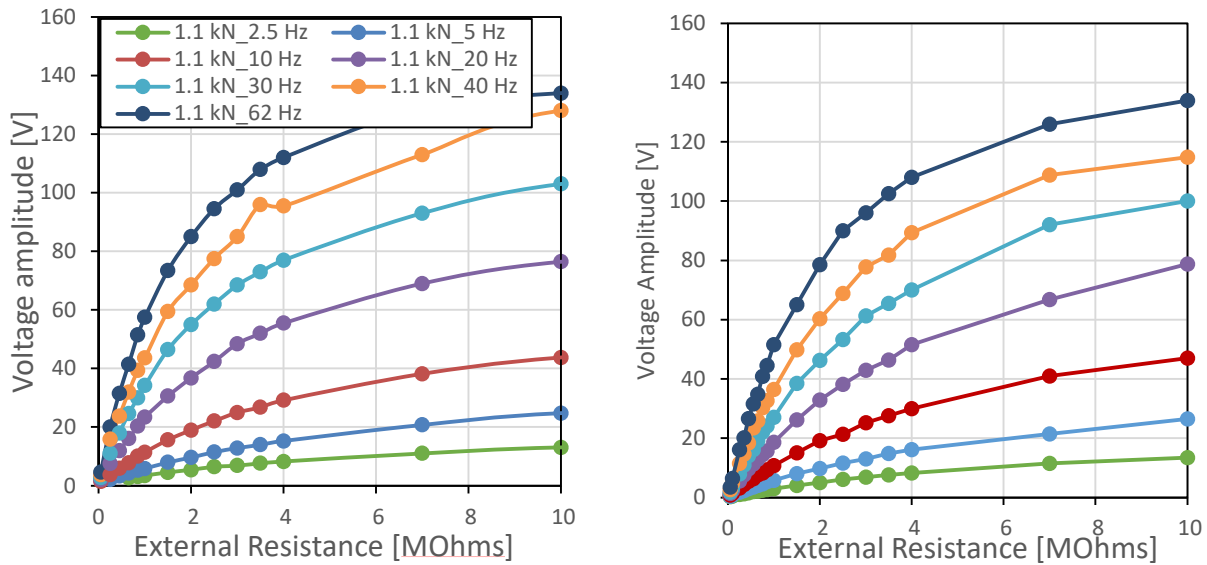


Figure 28. Voltage amplitudes (a) Top disk within stack no rectifier (left) (b) Top disk within stack with rectifier (right).

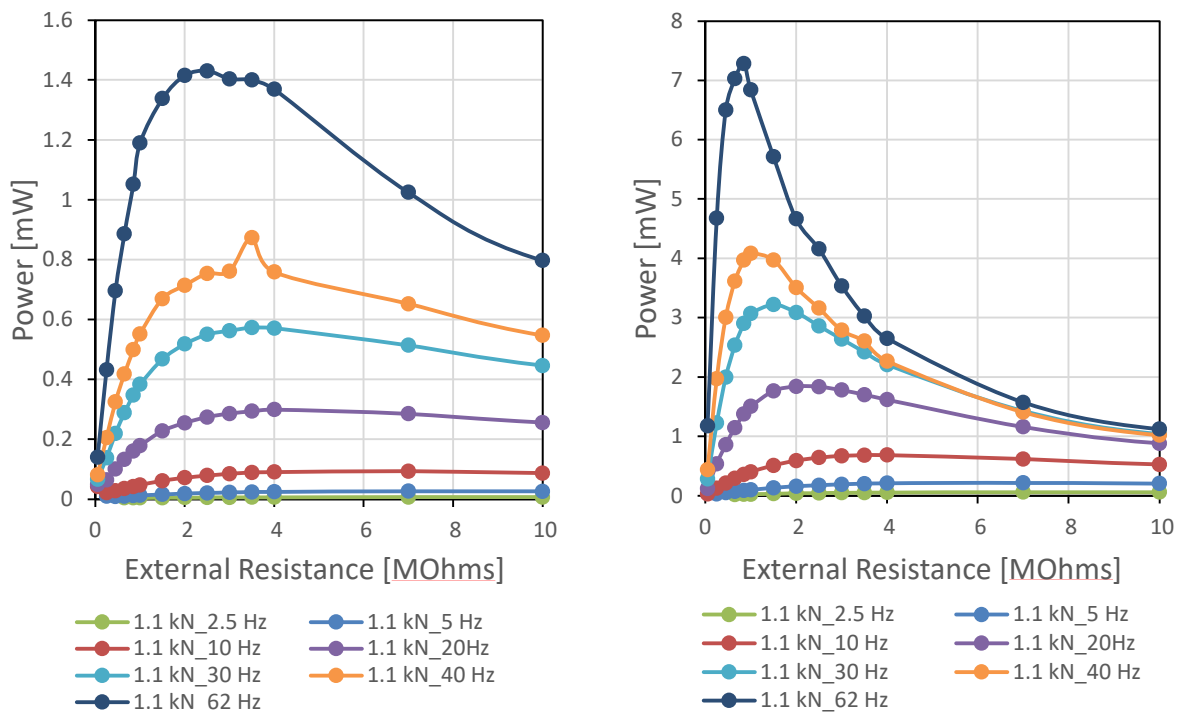


Figure 29. The power output from (a) top disk within the stack (left) (b) rest of the 5 disks in the stack (right).

4.1.5 Testing PZT Stacks

The PEH system design, to be described under Section 4.3, is to be powered by four PZT stacks connected in parallel and sharing the loads applied on the system enclosure. Therefore, extensive testing was carried out to evaluate the PZT stack performance for different loading scenarios. After

testing each individual stack, a series of experiments were done to evaluate the performance of the combined PZT stacks alternatively connected in series and in parallel.

4.1.5.1 PZT Stack Performance Consistency

The objective of this part of the testing was to verify that the fabricated piezoelectric PZT stacks exhibited consistent electromechanical behavior. Four PZT stacks fabricated, hence referred to as A, B C and D. They were tested under 10 Hz continuous sinusoidal loading with amplitudes ranging from 2 kN to 11 kN. Testing was repeated two times for each stack and their output was measured and recorded with the oscilloscope. Each PZT stack was directly connected to the oscilloscope (i.e., there was no rectifier, resistor or capacitor inserted between them), hence, the voltage output was measured under open circuit conditions.

The measured voltage amplitude of the output signal was plotted versus the loading amplitude. For a loading frequency of 10 Hz, the results suggest a linear relationship between load amplitude and voltage amplitude (Figure 30). As can be seen in the figure, the quality of the fit was very good. All the other regression lines for the other specimens have similarly high qualities of fit (i.e., R^2 values around 0.99). The y-intercept for all the regression lines was set to zero, since the output voltage was zero when there was no stress applied. Table 4 summarizes the slopes of the regression lines corresponding to each test. The coefficient of variation (CV) of the slope of these curves was approximately 1.4%, which allowed concluding that the PZT stacks exhibit consistent behaviour and can provide precise stress measurements.

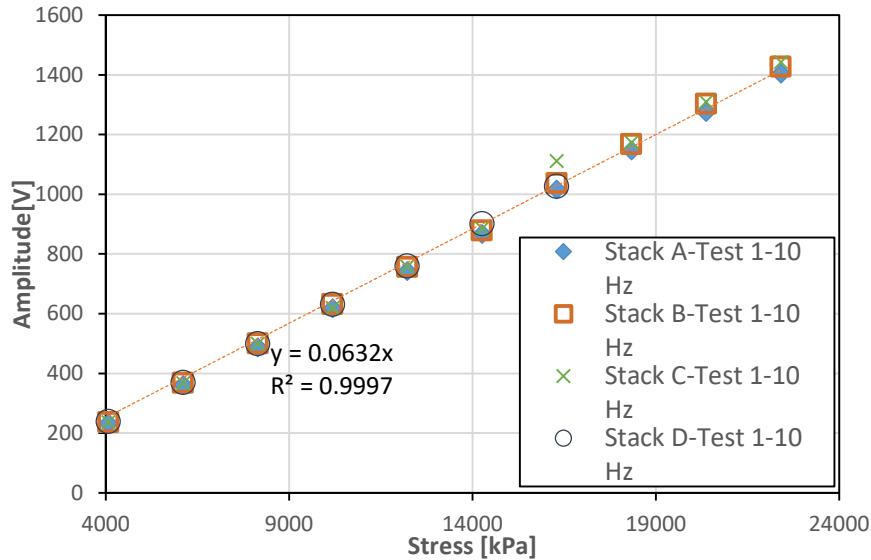


Figure 30. Relationship between stress and OC voltage for four fabricated stacks.

Table 4. Slope of the PZT stack voltage output versus stress at 10 Hz.

Specimen	Slope	
	Test 1	Test 2
Stack A	0.062	0.0621
Stack B	0.0632	0.0636

Stack C	0.064	0.0636
Stack D	0.062	---
Mean	0.0631	0.0631
CV	1.4%	1%

The same test was repeated with each piezoelectric stack connected to a 3 MΩ external resistor. Since it was proven that the PZT stacks behaved consistently, this test was only done for Stack A. It was shown that the relationship between the amplitude of the output voltage and the amplitude of the applied mechanical stress remained linear for a closed circuit. As can be seen in Figure 31, under an external resistance of 3 MΩ, the relationship remained linear but the slope of the regression line was lower than the one obtained under open-circuit conditions (i.e., 0.037 compared to 0.060, respectively).

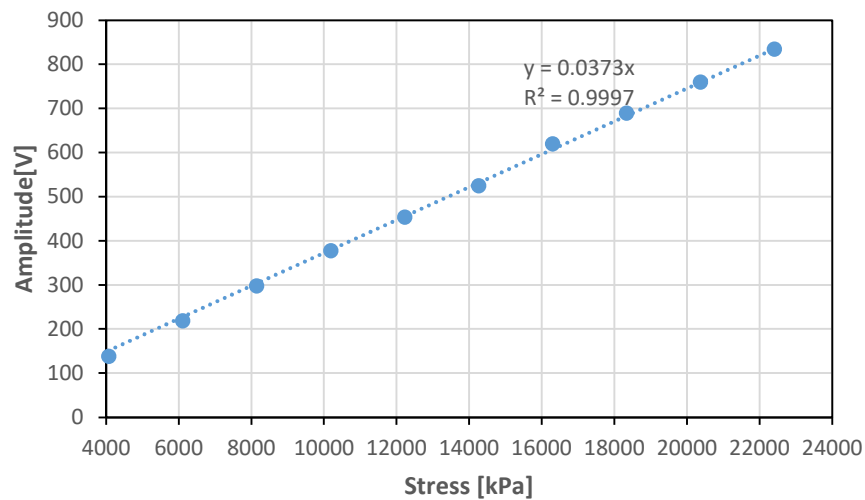


Figure 31. Voltage amplitude versus stress amplitude under an external electrical load of 3 MΩ; Stack A, sinusoidal load of 10 Hz frequency.

The same test was repeated using a pulsating load with an amplitude of 11 kN and loading frequency of 10 Hz (i.e., length of pulse was 0.1 sec). The relationship between the stress and the voltage was similar to that obtained under sinusoidal load. As seen in Figure 32, the regression line under pulsating loads had a slope of 0.041 compared to a slope of 0.037 under a continuously applied sinusoidal load.

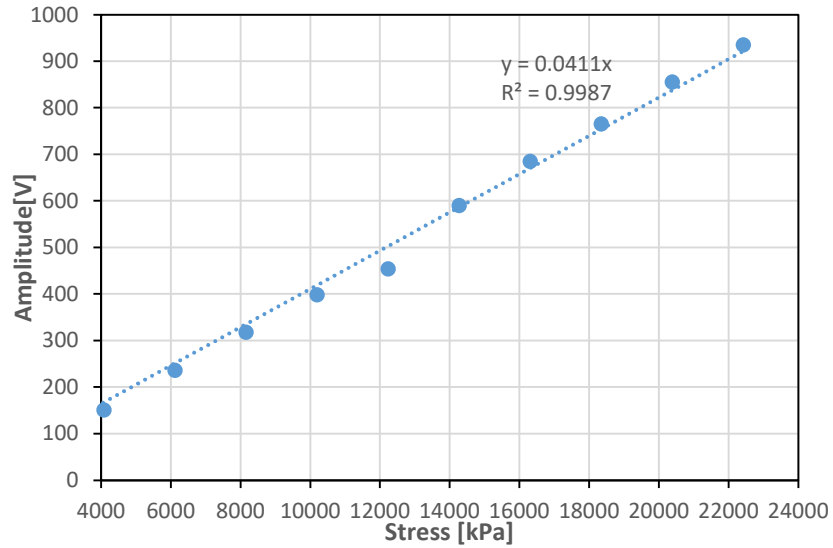


Figure 32. Stress versus output voltage; Stack A, external resistance of 3 MΩ; Pulse loading of 11 kN, 0.1 sec and 0.9 sec rest period.

Following these laboratory tests, it can be concluded that the voltage and stress have a linear relationship which can be written as [37]:

$$V_{RL} = \alpha_{RL}^f \sigma \quad [37]$$

Where, V_{RL} is the voltage amplitude (Volts) measured across electrical load R_L , σ is the applied stress (kPa) and α_{RL}^f is the slope associated with an electrical load of R_L and a loading frequency f . Figure 33 plots the voltage-stress relationship for open circuit conditions for frequencies ranging from 2.5 Hz to 62 Hz.

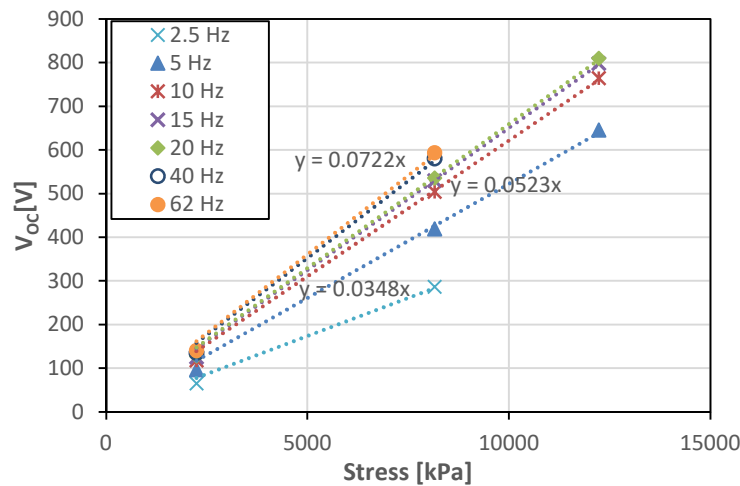


Figure 33. OC voltage versus stress for different frequencies.

Figure 34 plots the α_{RL}^f values (i.e., or the open circuit value α_{OC}^f) versus loading frequency. This suggests that the slope of the voltage-stress relationships, α_{RL}^f , increases with increasing frequency f , although these changes appear to be less pronounced for frequencies higher than about 15 Hz. Hence, it is concluded that under OC conditions and relatively high frequencies, α_{RL}^f is roughly constant. This, however, is not the case for voltage measurements obtained with a finite external electrical load as it will be discussed in the next section.

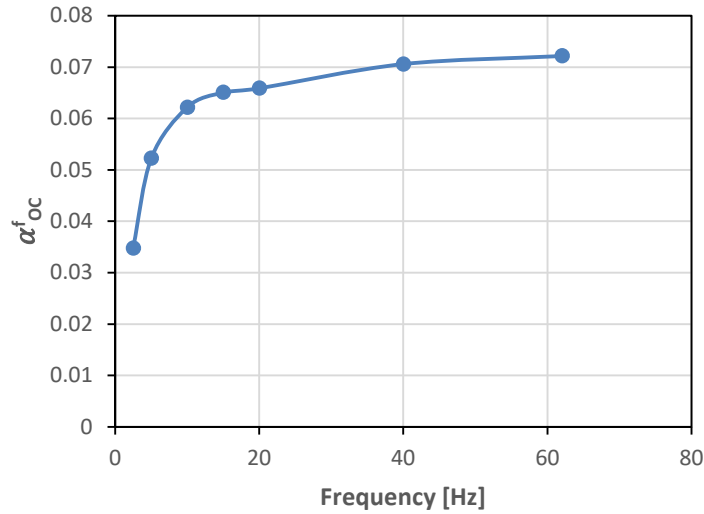


Figure 34. The effect of frequency on α_{oc}^f .

Figure 35 shows the relationship between voltage amplitude and applied stress using an external resistance of 650 k Ω . Figure 36 suggests that as the loading frequency increases the slope α_{RL}^f of the voltage amplitude versus loading amplitude keeps increasing. This effect is plotted in Figure 36. This lead to the conclusion that the relationship between voltage output and stress amplitude needs to be established as a function of the stress frequency and the external electrical load connected to the PZT stacks.

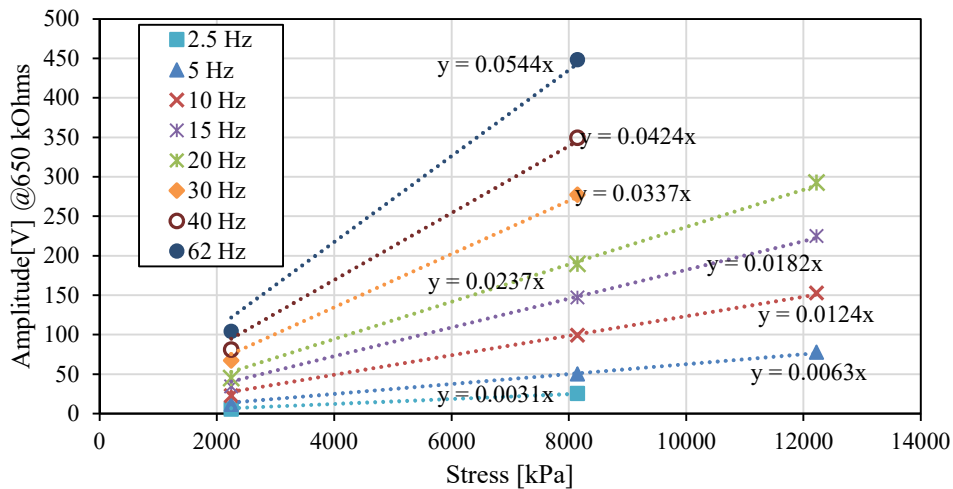


Figure 35. Voltage versus stress for various frequencies; 650 k Ω external resistor, pulse loading.

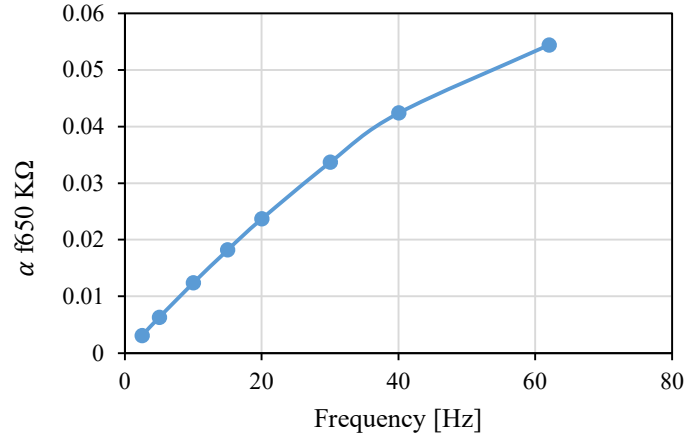


Figure 36. The effect of frequency on $\alpha f_{650 \text{ k}\Omega}$.

4.1.5.2 Impedance matching

According to the power-transfer theorem also known as “Jacobi’s law” (50), the maximum amount of power output from a source occurs when the external electrical impedance matches the internal impedance of the source. The RMS power output of the PZT stack was calculated via $P=V_{rms}^2/R_L$ by measuring the voltage across an external resistance R_L . Testing involved a PZT stack subjected to sinusoidal loads with peak values ranging from 1.1 to 6 kN and loading frequencies from 2.5 to 62 Hz, while varying the external impedance. Under a 3 kN 10 Hz sinusoidal load, Figure 37 shows RMS power measured for various electrical loads. The maximum power occurs for an electrical load of 3 M Ω , which suggests that the internal resistance of a stack is around 3 M Ω . In the following sections, the influence of two factors affecting the matching impedance are investigated, namely the excitation force and the presence of a rectifier. The effect of the excitation force is demonstrated by Figure 38 (a) and (b), which plot the power output versus external impedance for a 10 Hz sinusoidal loading and a pulse loading, respectively. These figures suggest that the external impedance that maximizes the power output is 3 M Ω , regardless of the type of loading.

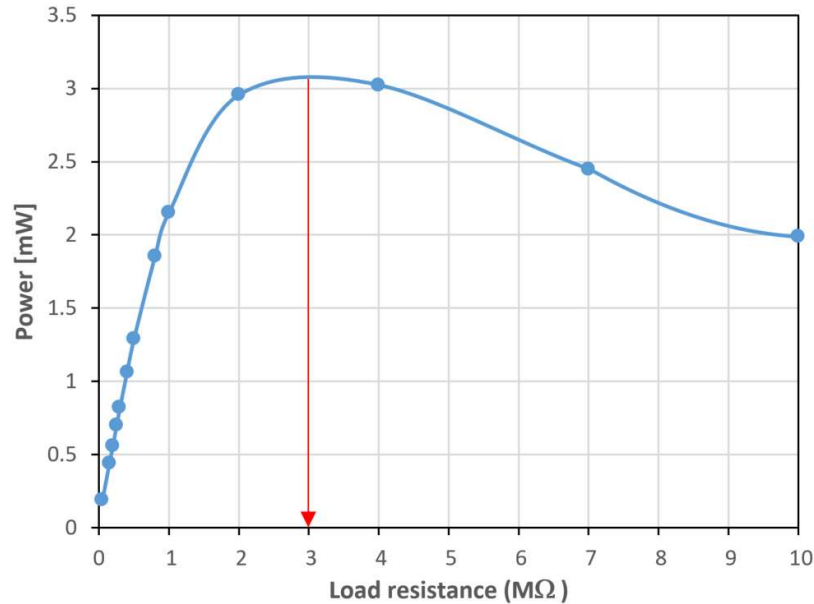


Figure 37. RMS power and electrical load for stack A under 3 kN 10 Hz sinusoidal load The matching impedance is 3 MΩ where the graph reaches its maximum.

Figure 39 (a) and (b) plot the power output for load levels of 1.1 and 6 kN, respectively, over a range of frequencies. These figures suggest that the external resistance required to maximize the power output decreases with increasing loading frequency. They also prove that for the same frequencies, the matching impedance is similar for different force amplitudes. Based on these results, more power can be harvested for higher loading frequencies. This reinforces the earlier observation that the output of the PZT stack needs to be established as a function of stress level, frequency and external impedance.

The effect of a rectifier connected in parallel to the PZT stack was investigated to determine its effect on the matching resistance. The rectifier was connected in parallel to the stack and the electrical load was connected in parallel to the stack and the rectifier. The results are shown for a 1.1 kN load in Figure 40. It was concluded that the presence of the rectifier doesn't influence the matching resistance nor the harvested power.

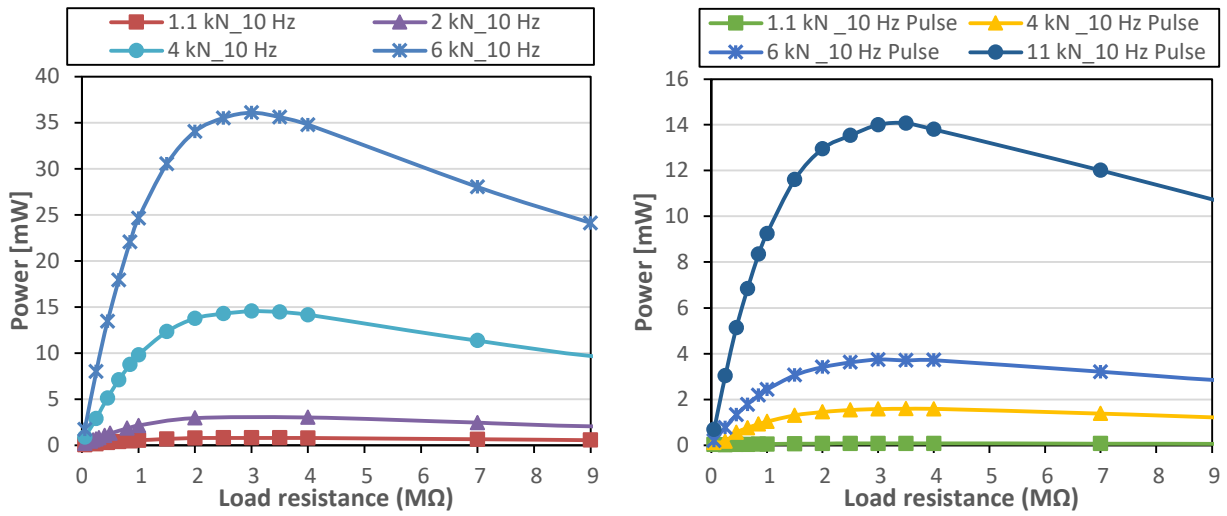


Figure 38. RMS power output versus electrical load resistance relationship at the same frequency for (a) sinusoidal excitation force (left) (b) pulsating excitation (right).

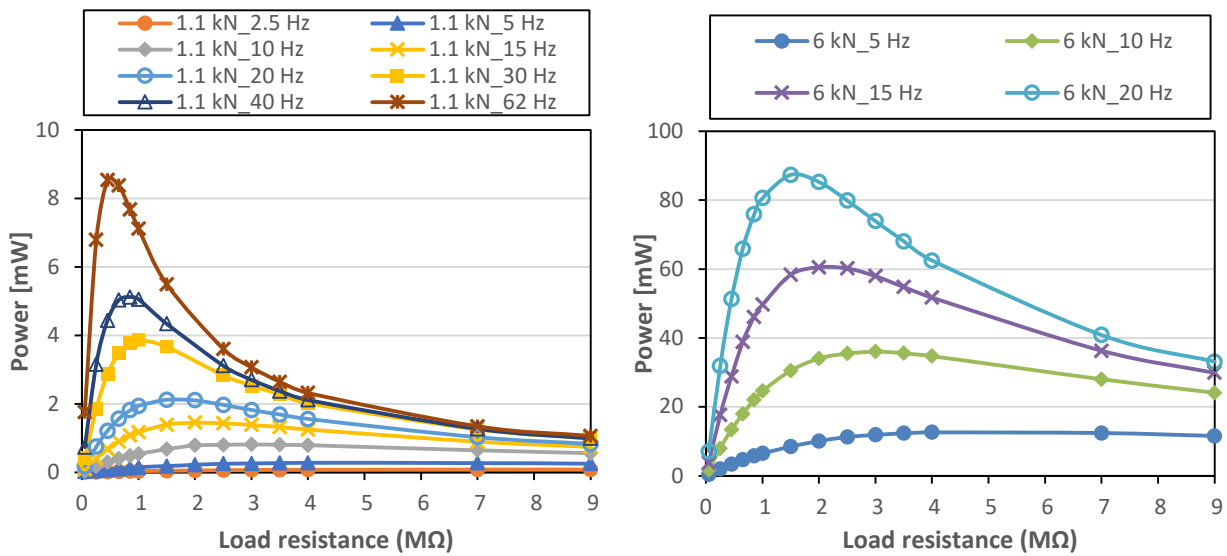


Figure 39. RMS power output versus electrical load resistance for various frequencies; (a) sinusoidal load with 1.1 kN peaks (left) (b) sinusoidal load with 6 kN peaks (right).

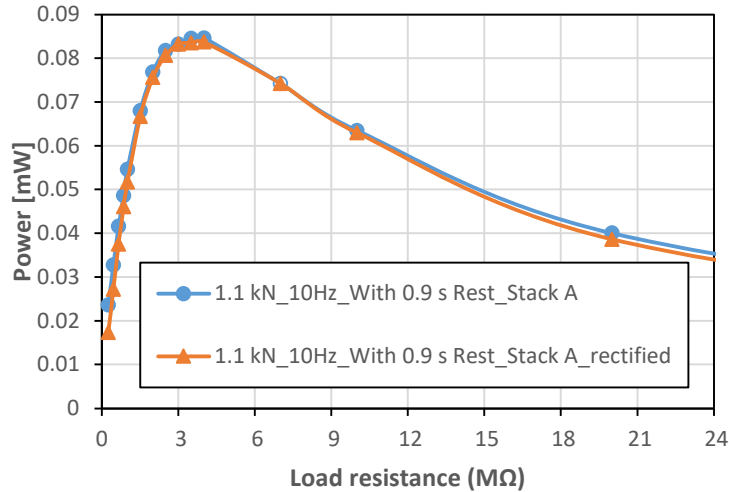


Figure 40. The influence of rectifying the piezoelectric output voltage.

4.1.5.3 Two PZT stacks connected in parallel without a rectifier

This test was done to assess the performance of the PZT stacks when they are connected in parallel and share the applied load. PZT stacks C and D were tested (Figure 41) under sinusoidal loads with amplitudes of 1.1 kN and 2.2 kN over frequencies that range from 2.5 Hz and 62 Hz for each load amplitude.

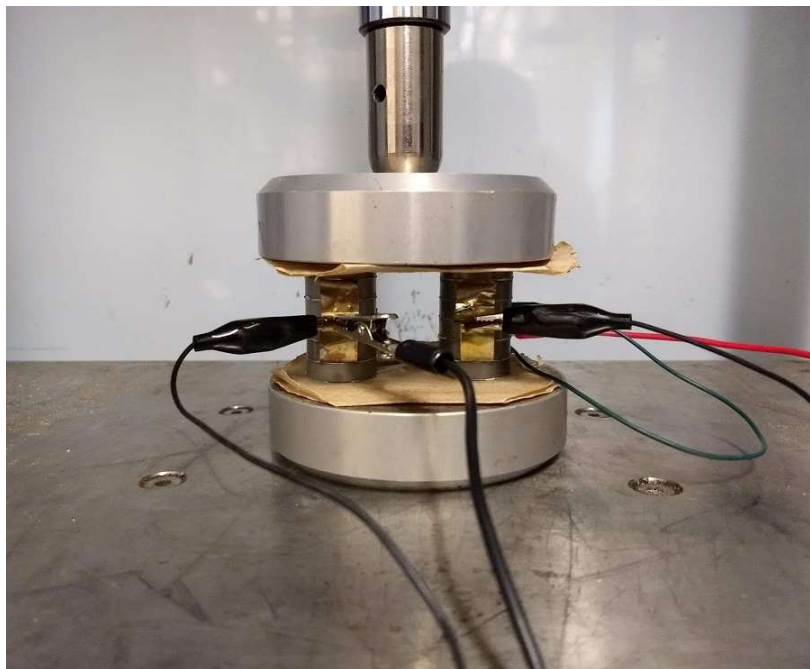


Figure 41. Testing two PZT stacks connected in parallel.

Assuming an equal split of load between the two PZT stacks, an applied load of 2.2 kN would result in 1.1 kN carried by each stack and roughly equal voltage outputs. However, this was not the case. For example, using an external resistance of 650 kΩ, the V_{rms} output of PZT Stack C was 12.2 V while that of PZT Stack D was 26.8 V. Similar testing under open-circuit conditions

generated outputs of 61.9 V and 134 V for PZT stacks C and D, respectively. These voltages are significantly different suggesting that the load is not equally distributed between the stacks despite the stiff plate used to apply the load. This was attributed to the fact that there were small differences in the height of the stacks due to the soldering process.

The output voltage amplitude and power generated versus the external resistance are plotted in Figure 42 and Figure 43, respectively. The maximum power values shown in Figure 43, allow estimating the matching impedance for each loading frequency. Theory suggests that the matching impedance of two stacks connected in parallel should be half that of a single stack. This was not the case however, as shown in Table 5 that summarizes the experimentally obtained impedances of one stack versus that of two stacks connected in parallel. It suggests that in general as the frequency increases, the impedance of the two stacks connected in parallel is slightly higher than half. This discrepancy can be explained by the unequal distribution of loads between the two stacks. As explained later, this slightly unequal distribution of load between stacks sharing the load is not detrimental to load measurement.

4.1.5.4 Two PZT stacks connected in parallel with a rectifier

Two stacks connected in a parallel were tested by adding a rectifier. Two alternative configurations were considered. The first involved a rectifier connected to each stack and the rectifiers connected in parallel (Figure 44(a)). The second involved a single rectifier (Figure 44(b)).

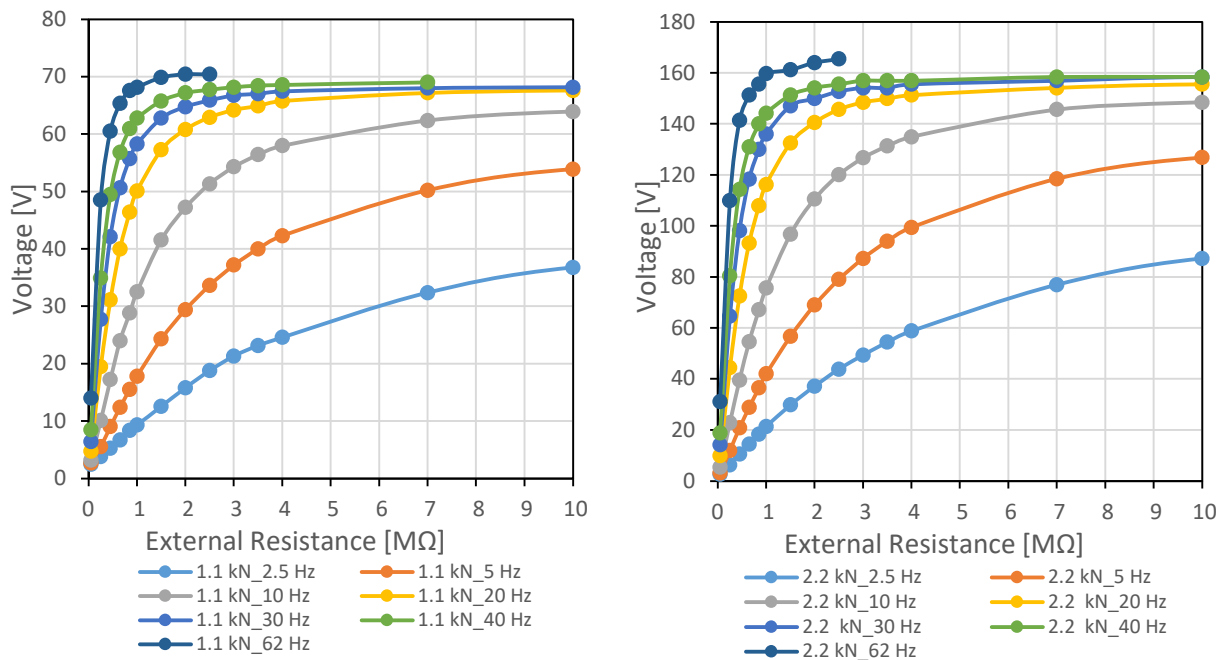


Figure 42. Voltage output versus external resistance; Two PZT stacks connected in parallel; sinusoidal loads, (a) 1.1 kN (left) and (b) 2.2 kN (right).

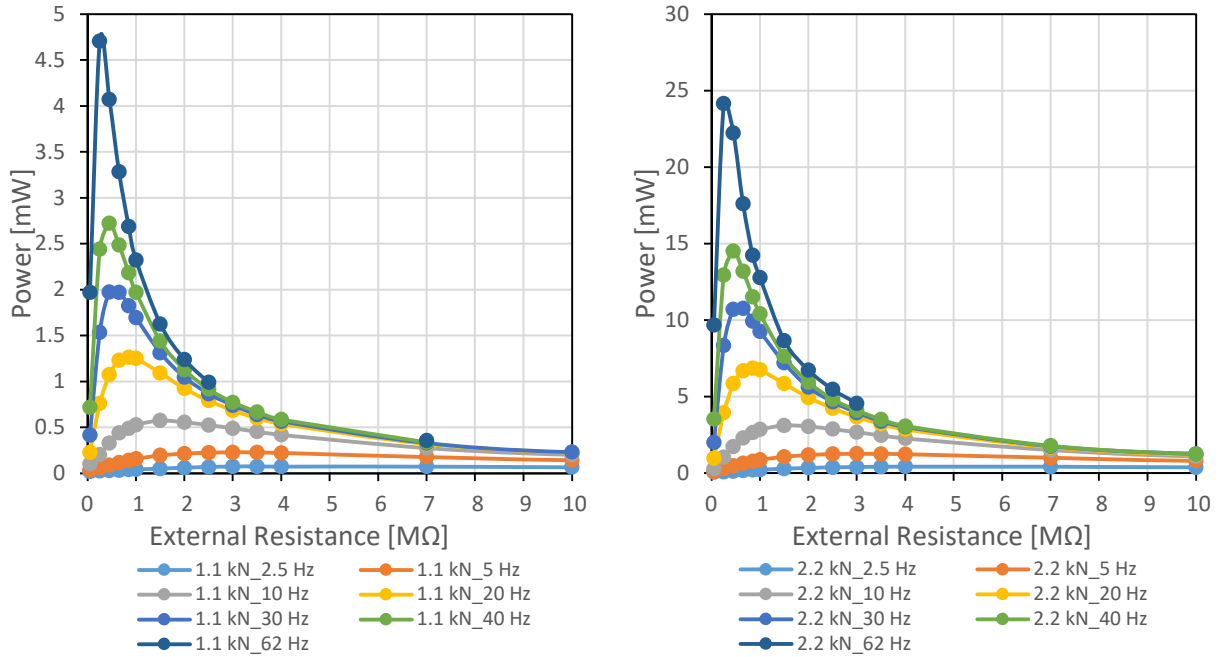


Figure 43. Power output versus external resistance; Two PZT stacks connected in parallel; Sinusoidal loads, (a) 1.1 kN (left) and (b) 2.2 kN (right).

Table 5. Experimentally obtained matching impedances of one versus two PZT stacks connected in parallel.

Frequency [Hz]	Matching Impedance (MΩ)		Ratio
	One Stack	Two Stacks connected in parallel	
2.5	7	3.5	0.500
5	4	3	0.750
10	3	1.5	0.500
20	1.5	0.850	0.567
30	1	0.650	0.650
40	0.850	0.450	0.529
62	0.450	0.250	0.556

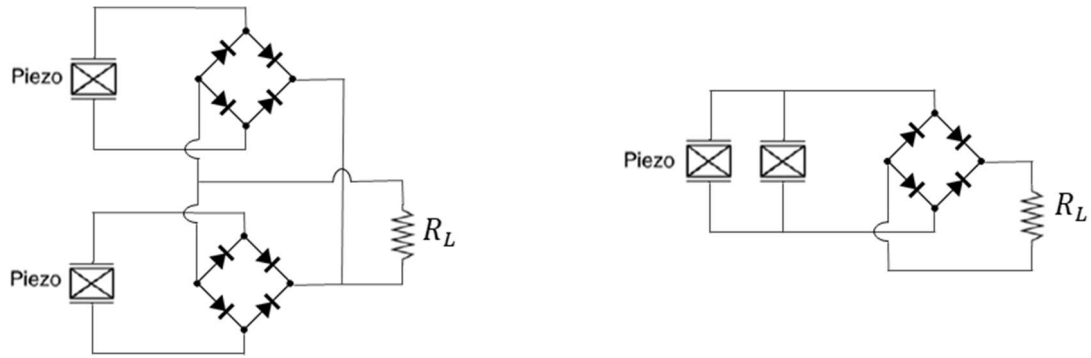


Figure 44. Different rectifier configurations (a) two rectifiers (b) one rectifier.

Testing showed that the two-rectifier design (i.e., Figure 44(a)) generated slightly higher voltage. As a result, the following experimental results correspond to this rectifier configuration. A continuous sinusoidal load was applied with a minimum value of 0.2 kN and a maximum value of 2.2 kN over a range of frequencies (i.e., 10 Hz to 62 Hz). In this test, the differences in stack height was corrected by inserting paper sheets over the shorter stack. This adjustment yielded a more even voltage output (e.g., Stack C generated 98.6 V and Stack D generated 86.5 V under a 2.2 kN shared load). The voltage amplitude and power output versus external resistance are plotted in **Error! Reference source not found.** for loading frequencies of 10 and 62 Hz. Figure 46 compares the power output of a pair of stacks with and without a rectifier. It proves that the rectifier does not affect significantly the power output. Furthermore, it shows that the output of the two stacks connected in parallel is not affected by the force distribution between them.

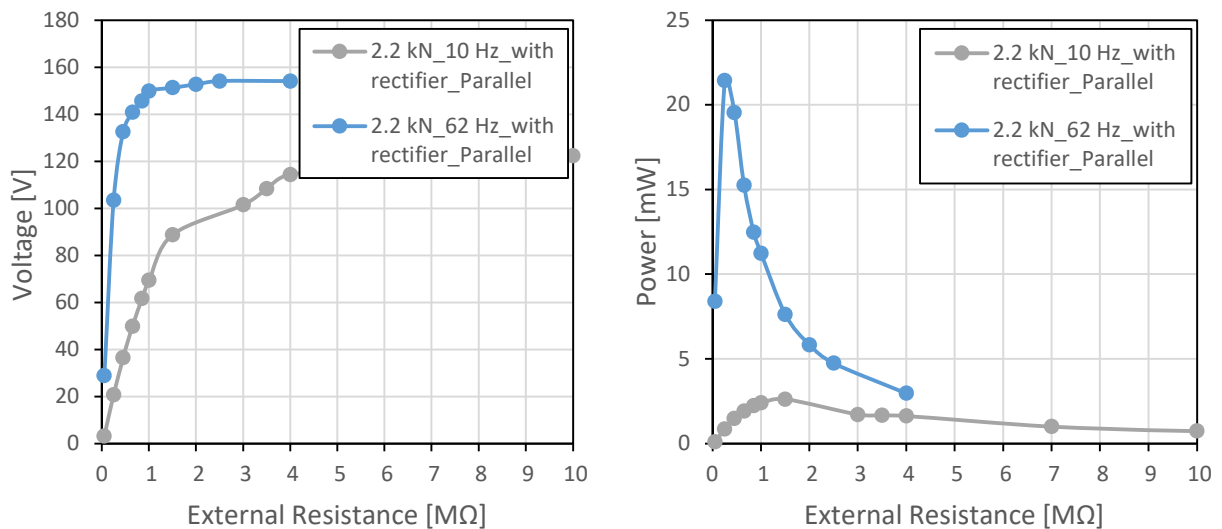


Figure 45. Two stacks connected to individual rectifiers connected in parallel (a) Voltage amplitude (left) (b) RMS power (right).

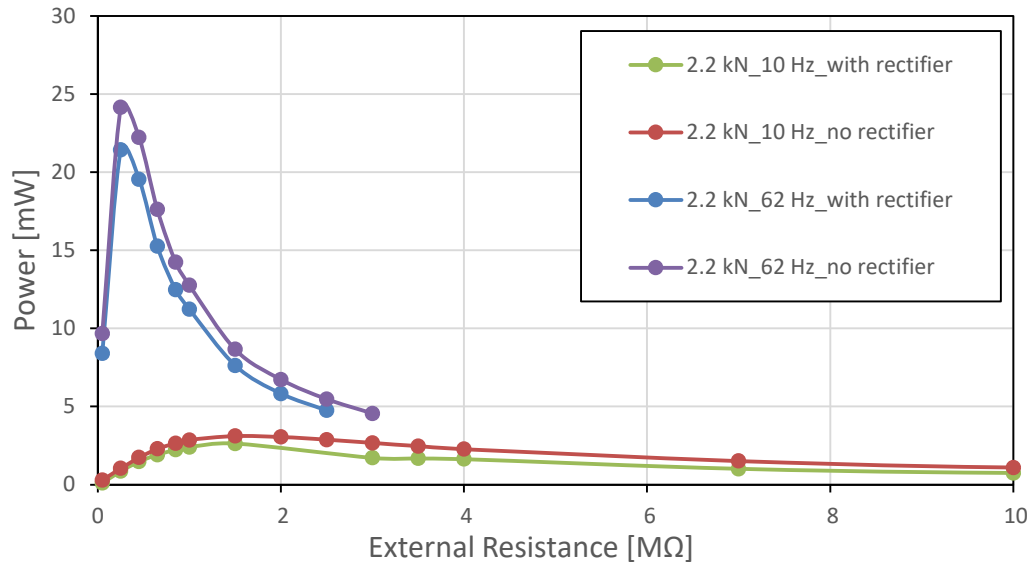


Figure 46. The comparison of the power from two parallel stacks with and without rectifier.

4.1.5.5 Two stacks connected in series

An alternative connection for the PZT stacks is in series. In order to compare the output of the parallel and series connection, two sets of tests were conducted on two PZT stacks, one without and another with a rectifier. The circuit configuration with the rectifiers is shown in Figure 47. A sinusoidal load was applied with a maximum value of 2.2 kN at 10 Hz.

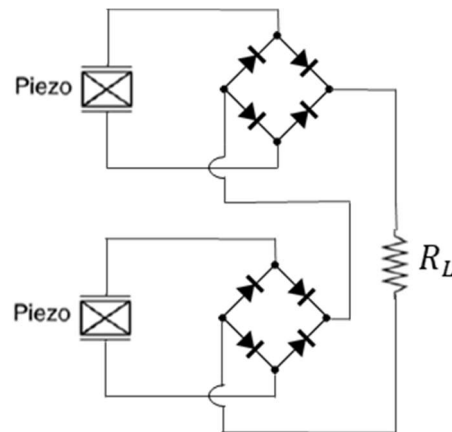


Figure 47. Circuit configuration for two stacks in series with rectifiers.

Figure 48 and Figure 49 show voltage and power output versus external resistance, respectively, for a 2.2 kN sinusoidal load applied at 10 Hz. Comparing these figures to those for the in parallel connection (i.e., Figure 42(b) and Figure 43(b)) suggests that the in parallel connection produces higher voltage and power output. This comparison is summarized in Table 6. So clearly, the in parallel connection of the stacks is better.

Another advantage of connecting the PZT stacks in parallel is that their combined voltage is the sum of the voltages of the individual stacks, which corresponds directly to the summation of the forces on the stacks. This solves the problem of the slight variations of load split on the stacks caused by their slight differences in height. Finally, Table 6 suggests, the in parallel connection reduces the impedance of the system and hence, reduces the magnitude of the external matching impedance required.

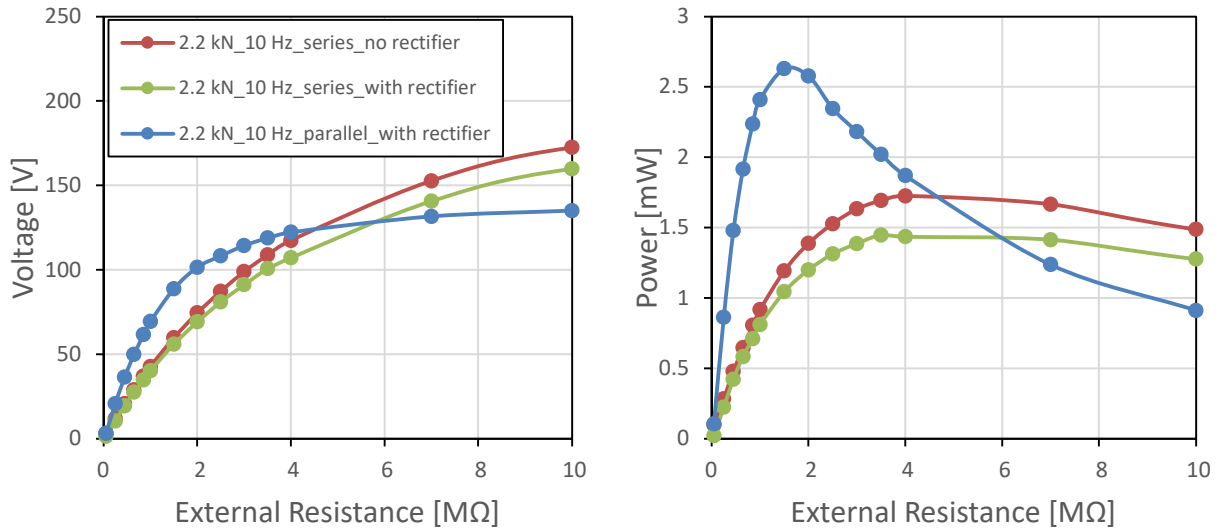


Figure 48. Output of two stacks for 10 Hz in series with and without rectifier compared to parallel a) Voltage amplitude (left) b) RMS power (right).

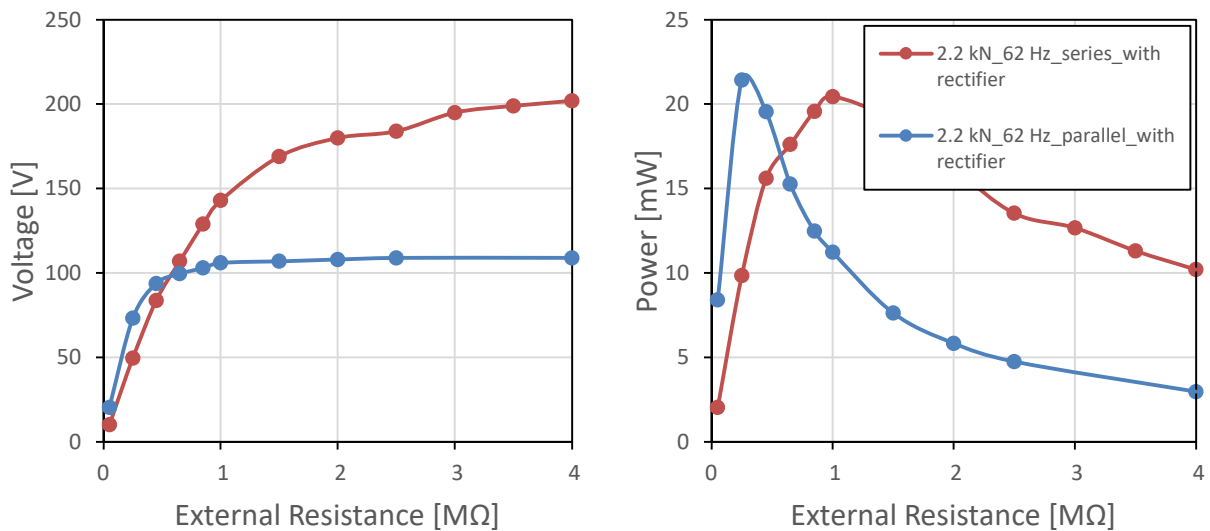


Figure 49. Output of two stacks for 62 Hz in series with rectifier compared to parallel a) Voltage amplitude (left) b) RMS power (right).

Table 6. Comparison of series and parallel connections in terms of maximum power and the matching impedance for low and high frequencies.

Frequency [Hz]	Max Power [mW]		Matching Impedance [$M\Omega$]	
	Series	Parallel	Series	Parallel
10	1.45	2.63	4	1.5
62	20.4	22.5	1	0.25

4.1.5.6 Three PZT stacks connected in parallel

In this test, three stacks connected in parallel were tested under three different mechanical load amplitudes of 1.1, 2.2 and 3.3 kN and frequencies of 10 Hz and 62 Hz representing low and high frequencies. The main reason for doing this experiment was to evaluate the effect of the number of stacks on the harvested power. The experimental results are shown in Figure 50. They show that three stacks connected in parallel behave similarly to the one stack (i.e., see section 4.1.5). The output voltage of the three stack increases linearly with force amplitude and can be expressed as shown in Equation [37]. This linear relationship is shown in Figure 51 for force magnitudes ranging from 1.1 kN to 3.3 kN at a frequency of 10 Hz. The figure shows that, although the relationship is linear, its slope is slightly lower than that corresponding to the single stack.

Figure 52 compares the power output of one stack, two stacks and three stacks under the same conditions described above. This comparison shows that increasing the number of stacks while keeping the same force amplitude, results in a lower power output and the only benefit being is a lower matching impedance. The matching impedance of three stacks is roughly equal to one third of an individual stack, confirming earlier findings. Figure 53 plots the maximum power output versus number of stacks. The maximum power decrease linearly with the number of stacks. The reason is that the power output from a PZT element is proportional to the square of the stress applied (18).

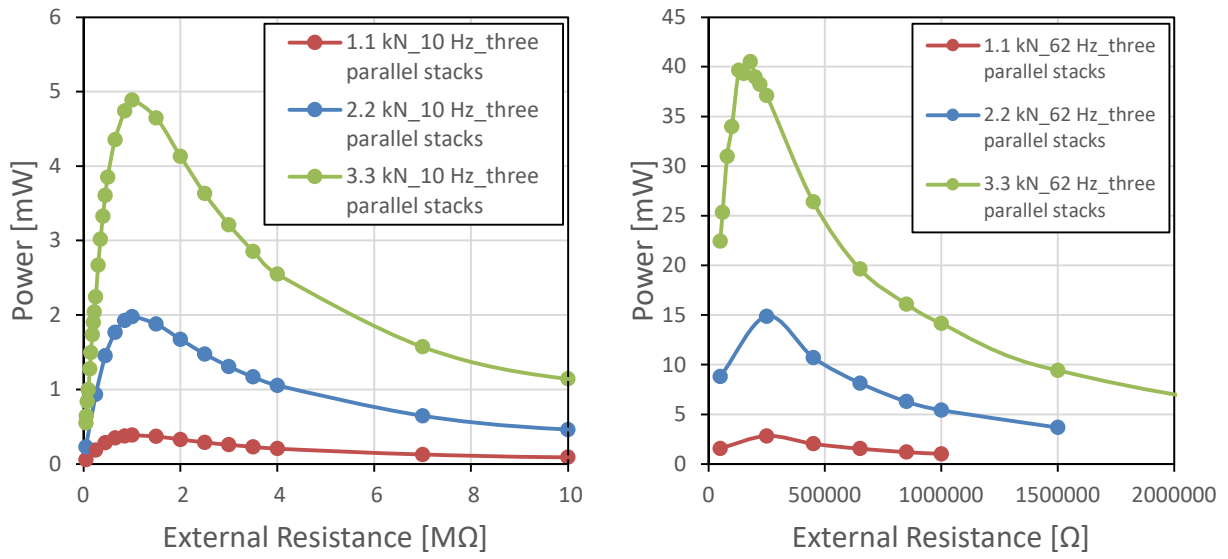


Figure 50. RMS power from three stacks in parallel for a) 10 Hz (left) b) 62 Hz (right).

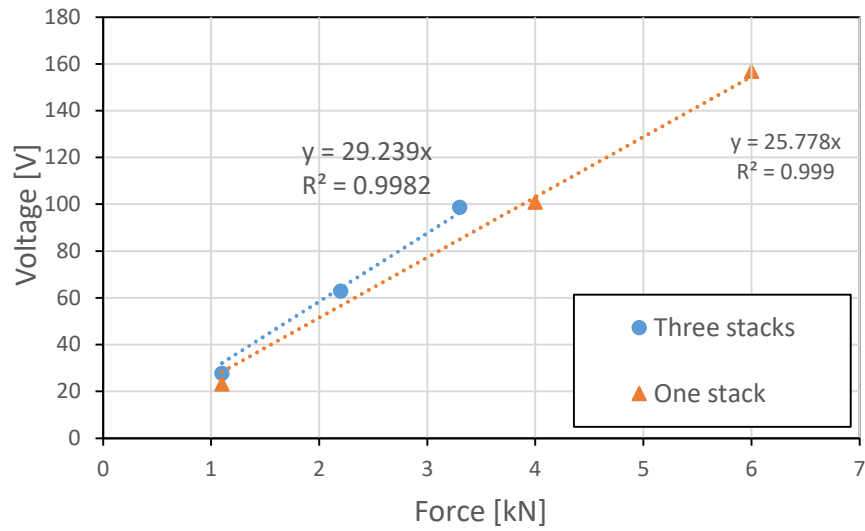


Figure 51. Voltage measured at $1M\Omega$ relationship to excitation force at 10 Hz for three stacks in parallel compared to one individual stack.

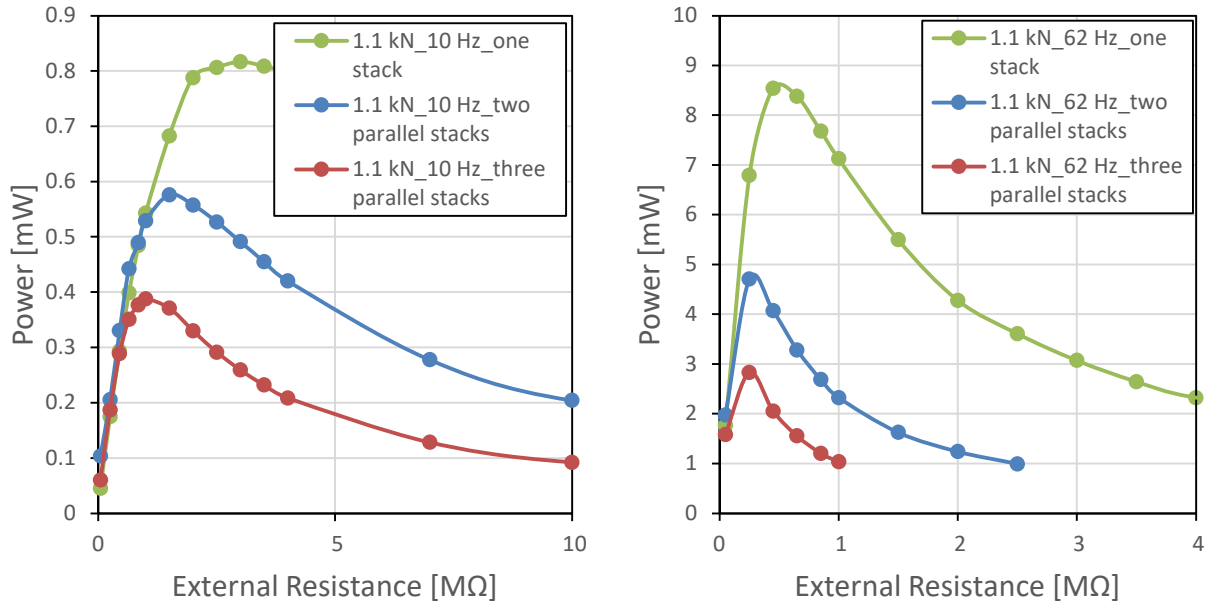


Figure 52. Power output of one, two and three stacks in parallel for a) 10 Hz (left) b) 62 Hz (right).

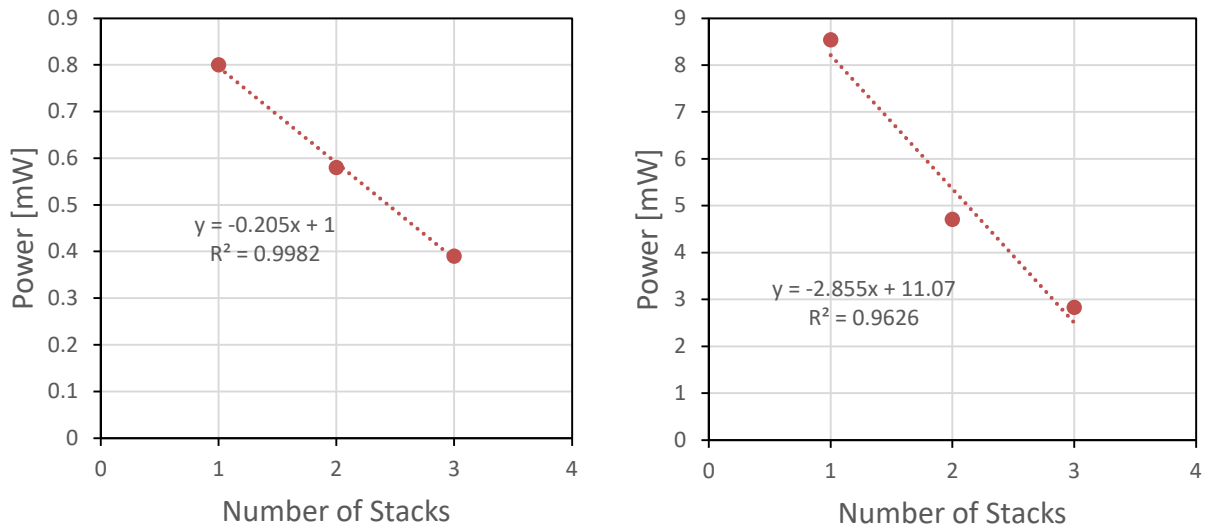


Figure 53. Power versus number of PZT stacks under a load of 1.1 kN (a) 10 Hz (left) (b) 62 Hz (right).

4.1.5.7 Four PZT stacks connected in parallel

Finally, four PZT stacks connected in parallel were evaluated because this is the final configuration envisioned for the PEH powering the WIM system. They were subjected to sinusoidal loads of 4.4 kN amplitude and frequencies ranging from 2.5 Hz to 62 Hz. The voltage and power output versus the external resistance are shown in Figure 54. Additional testing was carried out for this configuration to address the need for calibrating and validating the electromechanical model necessary for simulating the PEH, as described in the following Section 4.3. This included two

additional loading conditions, one involving a sinusoidal load with a peak of 2.2 kN at a frequency of 40 Hz and another involving a sinusoidal load of 6 kN at 62 Hz.

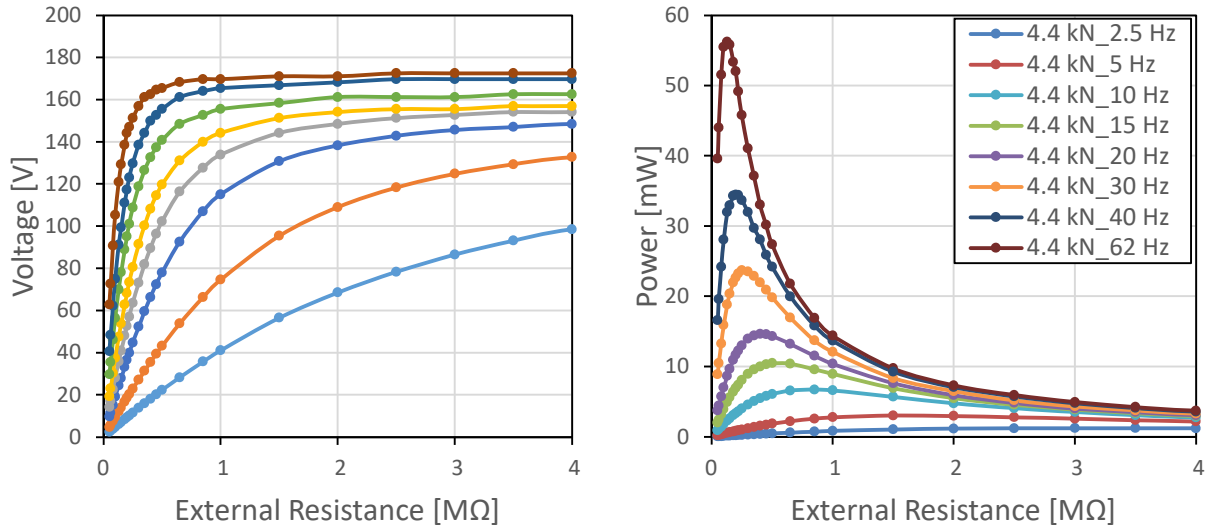


Figure 54. Output of four stacks connected in parallel (a) Voltage amplitude (left) (b) RMS Power (right).

Figure 55 compares the matching impedance (i.e., external resistance needed to maximize the power output) versus loading frequency for the 4 PZT stacks connected in parallel and a single PZT stack. It suggests that at higher loading frequencies (i.e., over about 15 Hz), the impedance of the set of 4 is indeed about 25% of the impedance of the single PZT stack.

The additive effect in connecting four PZT stacks together is shown in Figure 56 and Figure 57 for 10 Hz and 62 Hz respectively. Figure 58 plots the maximum power corresponding to the number of stacks for 10 and 62 Hz frequencies. The increase in power is linear but the rate of increase is higher for 62 Hz.

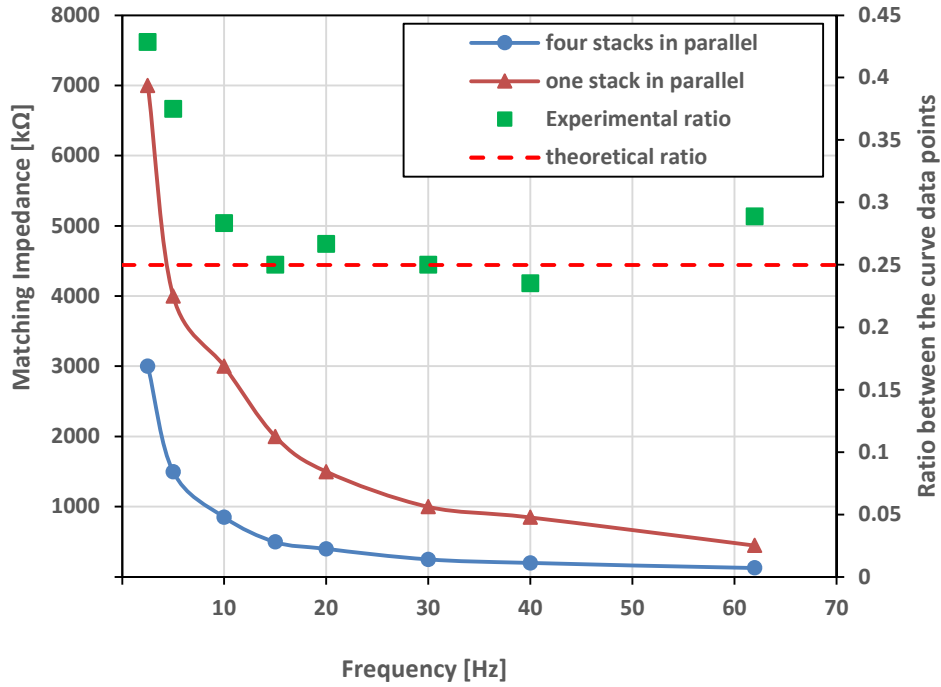


Figure 55. Matching impedance and frequency relationship; Four PZT stacks in parallel versus a single PZT stack.

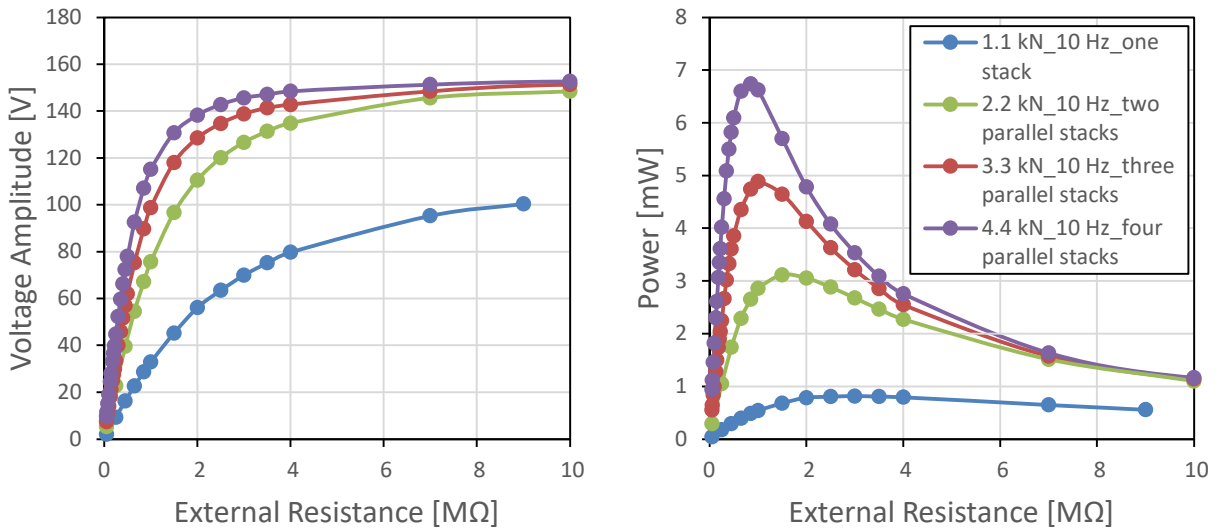


Figure 56. Effect of the number of stacks connected in parallel; Each stack carries the same load of 1.1 kN applied at 10 Hz (a) Voltage (left) (b) Power (right).

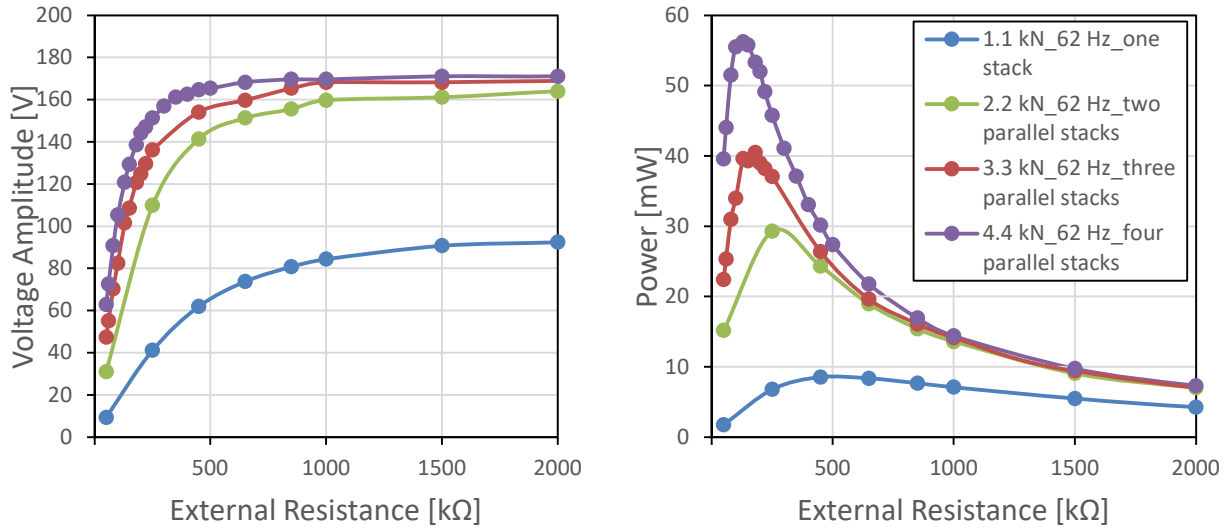


Figure 57. Effect of the number of stacks connected in parallel; Each stack carries the same load of 1.1 kN applied at 62 Hz (a) Voltage (left) (b) Power (right).

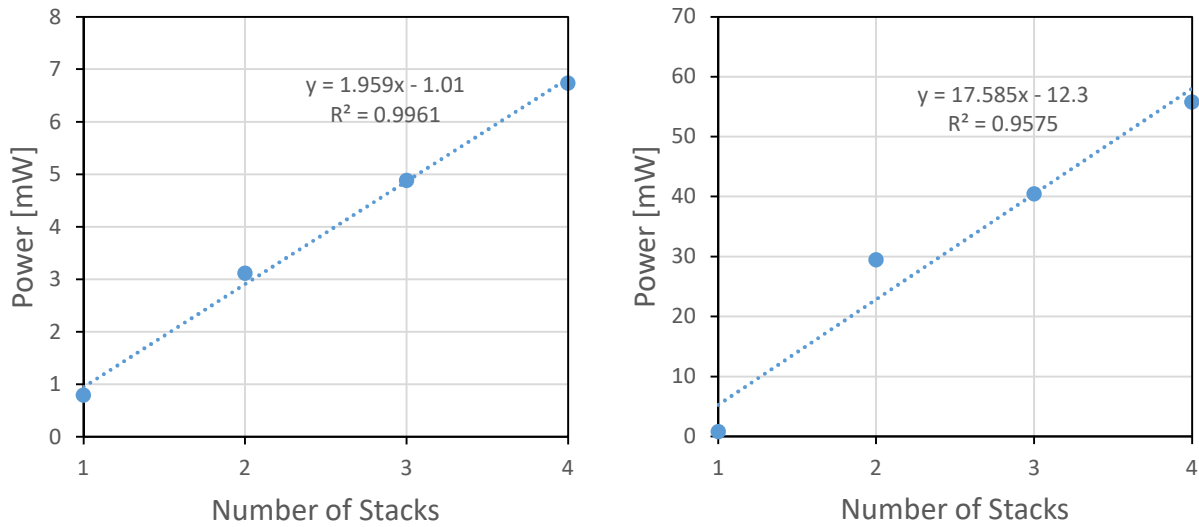


Figure 58. Power output versus number of stacks; Each stack carries 1.1 kN (a) Loading frequency of 10 Hz (left) (b) Loading frequency of 62 Hz (right).

4.1.6 Summary of Findings

The following presents an outline of the key finding of the laboratory testing of the PZT elements to be used for sensing and the PZT stacks to be used for energy harvesting:

- Given a loading frequency, the relationship between voltage output and stress is linear.
- The loading frequency affects the slope of the voltage output versus stress.
- The PZT stack output power is maximized when the external impedance matches the internal system impedance.

- The piezoelectric elements to be used for load sensing need to be electrically isolated from the PZT stacks.
- The in parallel connection of the sensing elements and the PZT stacks has several advantages over the in series connection. These include higher voltage and power under the same loading conditions, reduced matching impedances and direct summation of the sensing voltages, which leads to direct summation of the forces shared amongst the PZT stacks supporting the tire loads.
- The best rectifier configuration is connecting one rectifier to each PZT stack before connecting them in parallel.

The experimental data described here will be used in developing electromechanical models for the PZT stacks used for energy harvesting and the PZT elements used for load sensing, as described in the following Section.

4.2 Electromechanical Modeling

The electromechanical modeling of the PZT elements is essential in predicting their load sensing abilities and their capacity to generate power under roadway conditions. As discussed earlier (Section 3) and documented in the literature, PZT elements can be modeled as a voltage source combined with a capacitor connected in parallel (51) (21). An equivalent electrical circuit of the PZT was drawn providing a one-to-one correspondence between mechanical and electrical components as shown in Figure 59. Generally, mechanical force is analogous to the electrical voltage and the first derivative of displacement (i.e., velocity) is analogous to the electrical current.

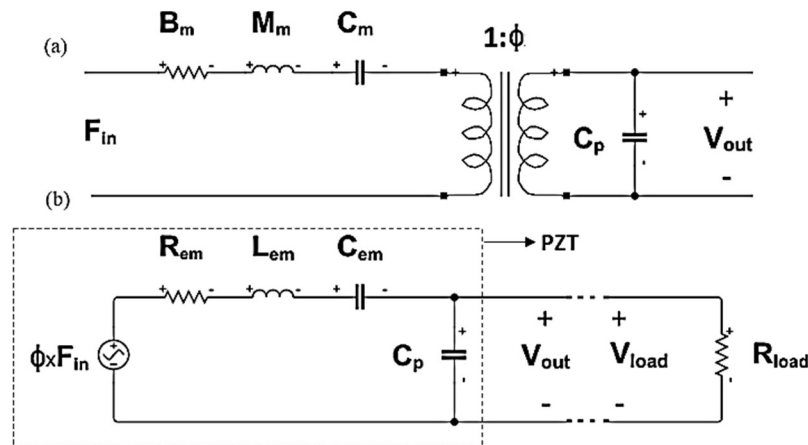


Figure 59. Electro-mechanical correspondence of piezoelectric materials: (a) Electromechanical model and (b) Equivalent electrical circuit.

4.2.1 Isolated PZT Disk Model

The electromechanical characterization of the PZT disks was done by comparing the predicted voltage amplitude as shown in Equation [36] to the voltage measured across an external resistance R_{Load} . The experimental tests on PZT materials suggested that their behavior depends on the loading frequency and the stress amplitude. The model was calibrated using laboratory data obtained by subjecting the PZT disks to a load amplitude of 1.1 kN with frequencies ranging from 2.5 to 62 Hz. The voltage output were measured under various external impedances ranging from 50 k Ω to 10 M Ω . Model fitting was carried out using two alternative techniques, a Matlab® error minimization routine and an Excel® Solver function. These two techniques resulted in similar

parameter values. It was observed that the R_{em} and L_{em} are relatively insensitive to frequency, but the ϕ , C_p and C_{em} fitted values varied with frequency, especially the factor C_p . The factor ϕ changed over the relatively narrow range as the loading frequency increased from 2.5 Hz to 62 Hz. Hence, the values of ϕ , L_{em} and R_{em} were assumed to be constant. This allowed fitting the two factors that are most sensitive to the loading frequency, namely C_p and C_{em} . C_{em} is assumed to change linearly with frequency and C_p relationship to frequency can be fitted to a curve as shown by Equation [38].

$$C_p = 10^{-9} \left(\frac{1}{(af + b)^c} + d \right) \quad [38]$$

Where a , b , c and d are constants which are calibrated to fit C_p in nF and f is the frequency.

As discussed earlier (Section 4.1.3), the experimental voltage amplitude under sinusoidal loading can be recorded by following two different methods, namely peak-to-peak divided by two and estimated from the RMS measurements. The values for ϕ , L_{em} and R_{em} were assumed to be constant and the same for these two methods (Table 7) but the C_p and C_{em} values were considered to be frequency dependent and different depending on the method used. The relationship of these parameters to frequency are shown in Figure 60 for the two methods.

Figure 60 suggests that the functional relationships between C_p and loading frequency are very similar for the two methods, while the one for C_{em} , although different, they have identical slopes (i.e., 0.00060).

Table 7. Fitted parameters of an isolated disk that was used to build the stacks.

Parameter	Values
R_{em} [Ω]	13.009
L_{em} [Henries]	0.011
C_p [Farads]	Refer to Figure 60 (a)
C_{em} [Farads]	Refer to Figure 60 (b)
ϕ [V/N]	0.55

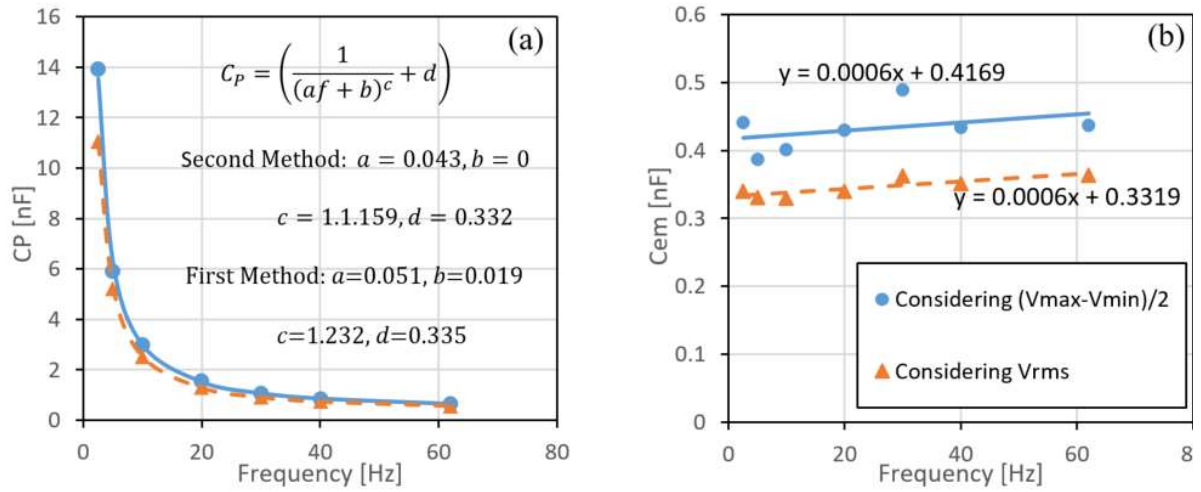


Figure 60. Frequency dependent model parameters for a single isolated disk.

4.2.2 PZT Stack Model

Modelling each PZT stack is essential in estimating the amount of power being produced under various traffic loads. The experimental data used for calibrating this model is shown in Figure 39(a). It was obtained under a sinusoidal load with amplitude of 1.1 kN. The fitted parameters are summarized in Table 8.

Table 8. Fitted parameters of the model of one individual stack.

Parameter	Values
R_{em} [Ω]	13.009
L_{em} [H]	0.033
C_P [F]	Refer to Figure 61(a)
C_{em} [F]	Refer to Figure 61(b)
ϕ [V/N]	0.55

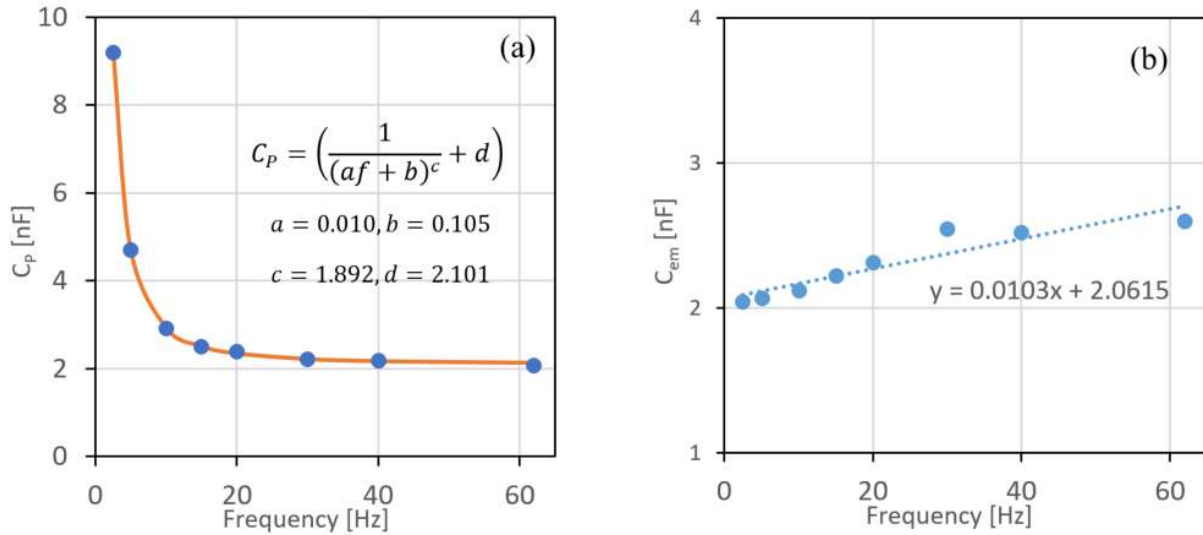


Figure 61. Frequency dependent electrical constants for one PZT stack; (a) C_p and (b) C_{em} .

The quality of the model was tested by comparing its voltage output predictions to the output voltages obtained measurements under different load magnitudes and frequencies. The results shown in Figure 62 suggest a very good agreement between model predictions and laboratory data. It is concluded that the electro-mechanical model fitted can reliably predict the electrical output from load input and vice-versa.

Figure 63(a) and Figure 63(b) show the dependence of the power output on the external impedance and the loading frequency for two magnitudes of load input, namely 1.1 kN and 11.1 kN, respectively. The ridge highlighted by the dots in each of these figures indicates the maximum harvested power and the matching impedance under each load magnitude. The maximum RMS power harvested from each PZT stack is 9 mW and 1400 mW for 1.1 kN and 11 kN, respectively. It is noted that the power output from four of these stacks connected in parallel, as envisioned for the PEH, will be at least four times as large as those shown in Figure 63, as discussed later. This power appears sufficient for powering a low consumption MCU, especially on roadways experiencing a large number of heavy truck axles.

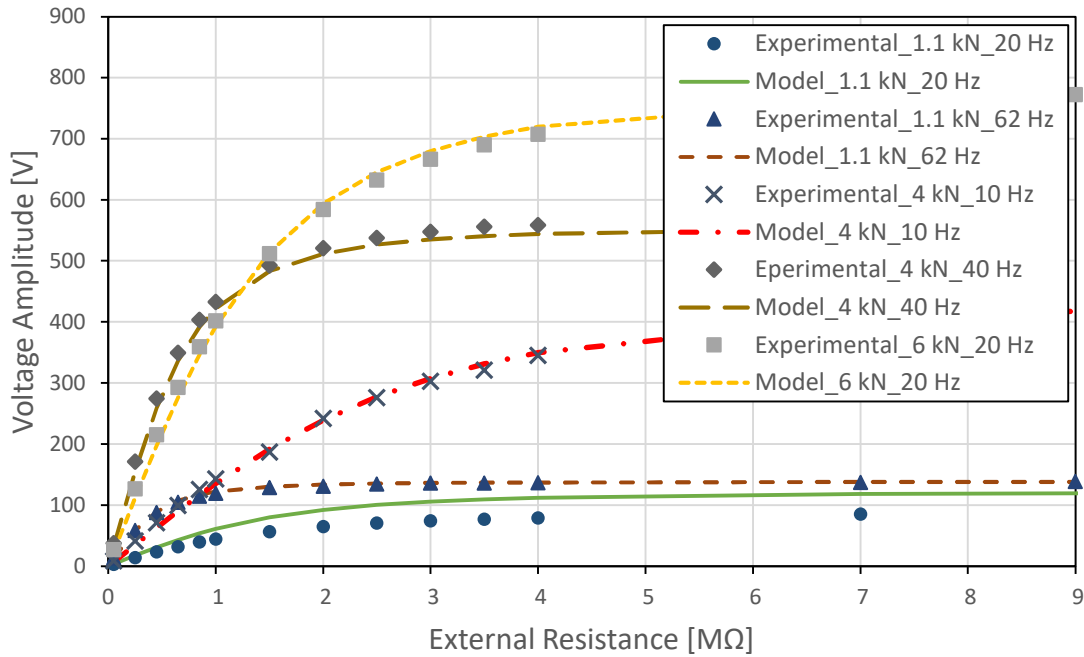


Figure 62. Electro-mechanical model verification using laboratory data obtained for various loads and frequencies.

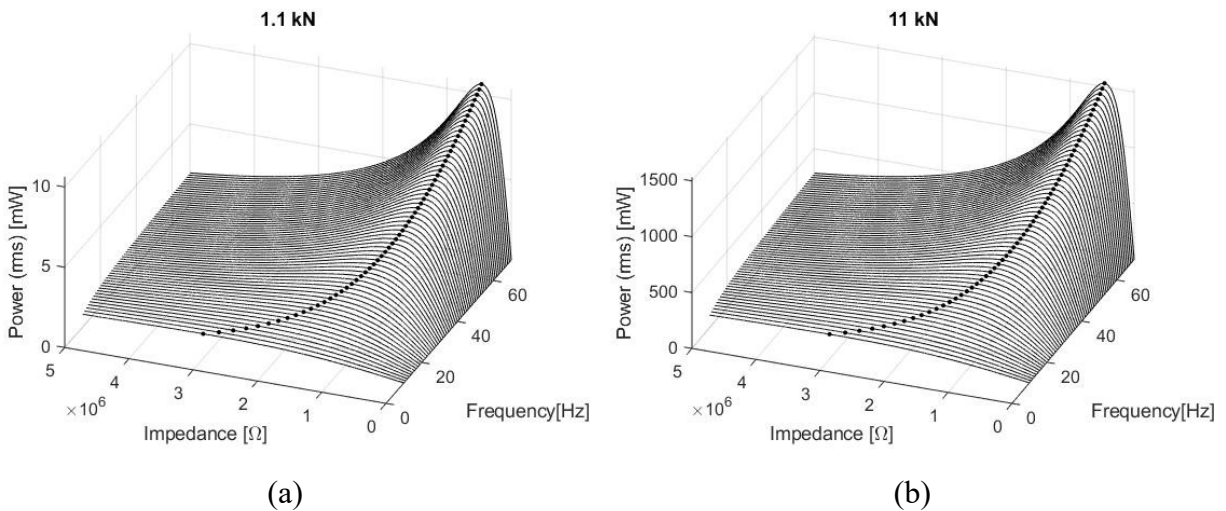


Figure 63. Power output versus impedance and frequency; (a) 1.1 kN load, (b) 11.1 kN load.

Testing four PZT stacks connected in parallel was carried out by subjecting them to a force excitation with an amplitude of 4.4 kN and a frequency of 10 Hz. The loads were applied using a stiff metal plate. Figure 64 shows the voltage output of each individual stack under such loading. Differences in the voltage output between stacks was due to the slight differences in heights between the stacks, as explained earlier. This, however, does not affect the summation of the forces on the four stacks. This was verified by the testing conducted next.

A 4.4 kN sinusoidal load at a frequency of 10 Hz was applied to all 4 PZT stacks connected in parallel. Figure 64 shows the relationship between voltage output and external resistance. Selecting an external resistance of 3 MΩ, allows computing the voltage output of each PZT stack, which in turn allow computing the corresponding forces (Equations [39]-[42]). Summing these four estimated forces (Equation[43 [43]) results in 4.788 kN, which is approximately equal to the 4.4 kN load applied.

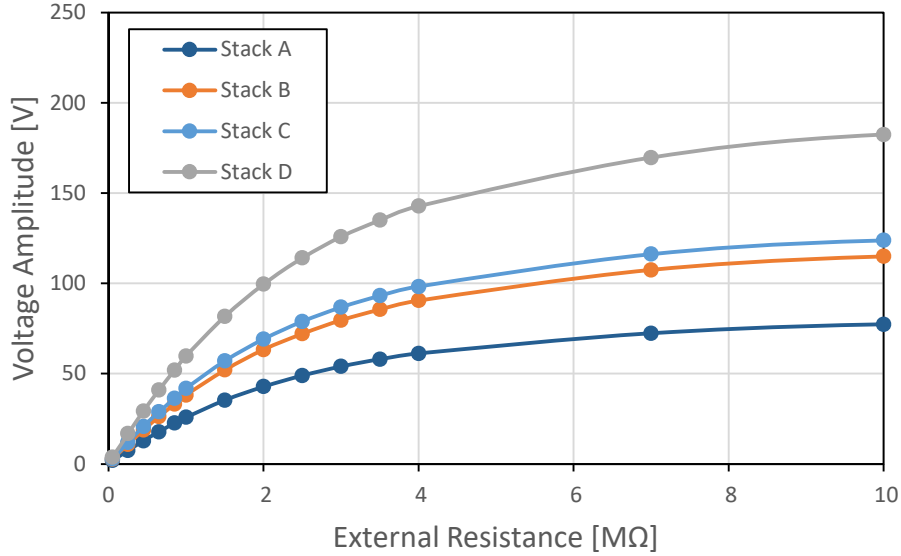


Figure 64. Individual PZT stack outputs subjected to a total load of 4.4 kN at 10 Hz; External resistance of 3 MΩ.

$$V_{Stack A}^{3 M\Omega} = 54.02 V, F_{Stack A} = 867 N \quad [39]$$

$$V_{Stack B}^{3 M\Omega} = 56.3 V, F_{Stack B} = 895 N \quad [40]$$

$$V_{Stack C}^{3 M\Omega} = 86.83 V, F_{Stack C} = 1272 N \quad [41]$$

$$V_{Stack D}^{3 M\Omega} = 125.86, F_{Stack D} = 1754 N \quad [42]$$

$$F_{Total} = F_{Stack A} + F_{Stack B} + F_{Stack C} + F_{Stack D} = 4,788 N \quad [43]$$

Utilizing lower external resistances, however, produces less accurate estimates of the 4.4 kN load applied. For example, using external resistances of 450 kΩ and 850 kΩ, produces summation of forces of 5.7 kN and 5.5 kN, respectively. The reason for this is that quality of fit of these

electromechanical models decreases as the external resistance becomes lower. This is another reason for separating the axle load measuring and the harvesting circuits of the system.

This model was also used to establish the relationship between matching impedance (i.e., the internal impedance of the model) and loading frequency (i.e., vehicle speed) as shown in Figure 65. As can be seen, the matching impedance computed with the model is in good agreement with the experimental data points presented earlier (Section 4.1.5).

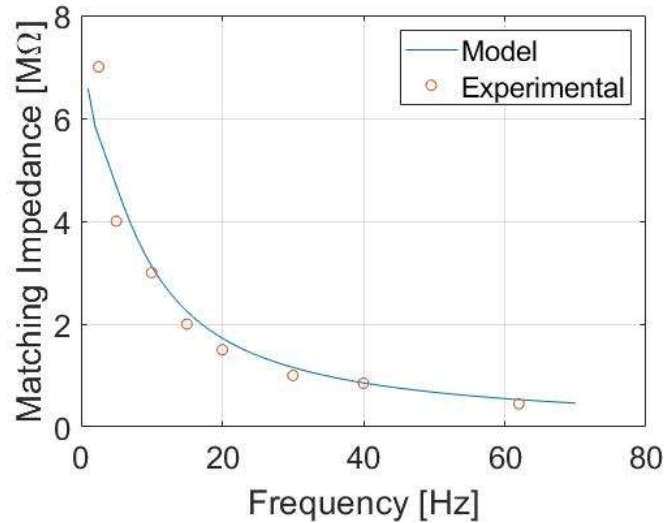


Figure 65. Matching impedance versus loading frequency of a PZT stack.

Figure 66 compare the values of the matching impedances for the isolated PZT disk and the PZT stack as a function of loading frequency. It can be seen that their differences become more pronounced as the frequency increases. As a matter of fact, for high loading frequencies, the impedance of the PZT stack tends to theoretical value of 1/6 that of the impedance of a single PZT element (Figure 67).

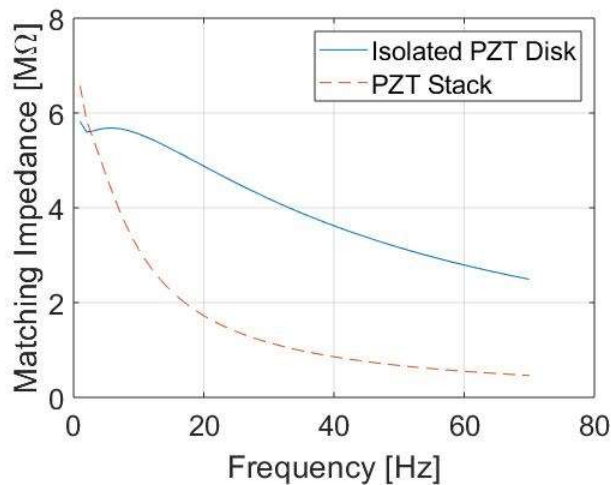


Figure 66. Comparison between the matching impedance of one disk and the stack.

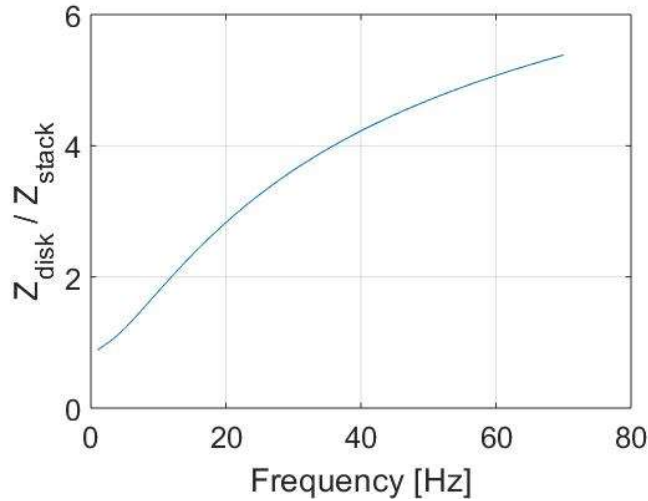


Figure 67. The ratio of matching impedance of disk and stack with respect to frequency.

4.2.3 Model for Four PZT Stacks Connected in Parallel

Fitting an electromechanical model to the output of four PZT stacks connected in parallel was necessary in simulating the energy harvesting circuitry of the WIM system envisioned. The experimental data presented in Section 4.1.5 was used for the model calibration. The fitted model parameters are summarized in Table 9. Two sets of data corresponding to sinusoidal loads of 6 kN at 62 Hz and 2.2 kN at 40 Hz were used for the validation of the model. As can be seen in Figure 69, the model shows good agreement with the experimental data. Figure 70 compares the frequency dependent parameters for the various combinations of PZT stacks considered. Both C_p and C_{em} have higher values for the 4 PZT stack model.

Table 9. Fitted parameters of the model for four PZT stacks connected in parallel.

Parameter	Values
R_{em} [Ω]	13.009
L_{em} [Henries]	0.033
C_p [Farads]	Refer to Figure 68 (a)
C_{em} [Farads]	Refer to Figure 68 (b)
ϕ [V/N]	0.55

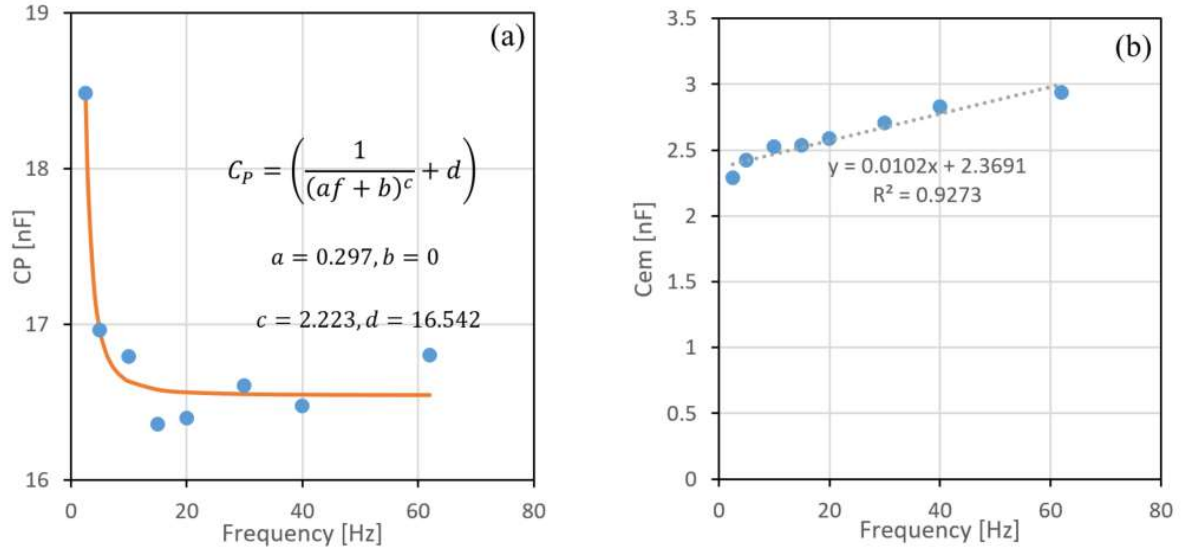


Figure 68. Frequency dependent electrical constants for four PZT stacks; (a) C_P and (b) C_{em} .

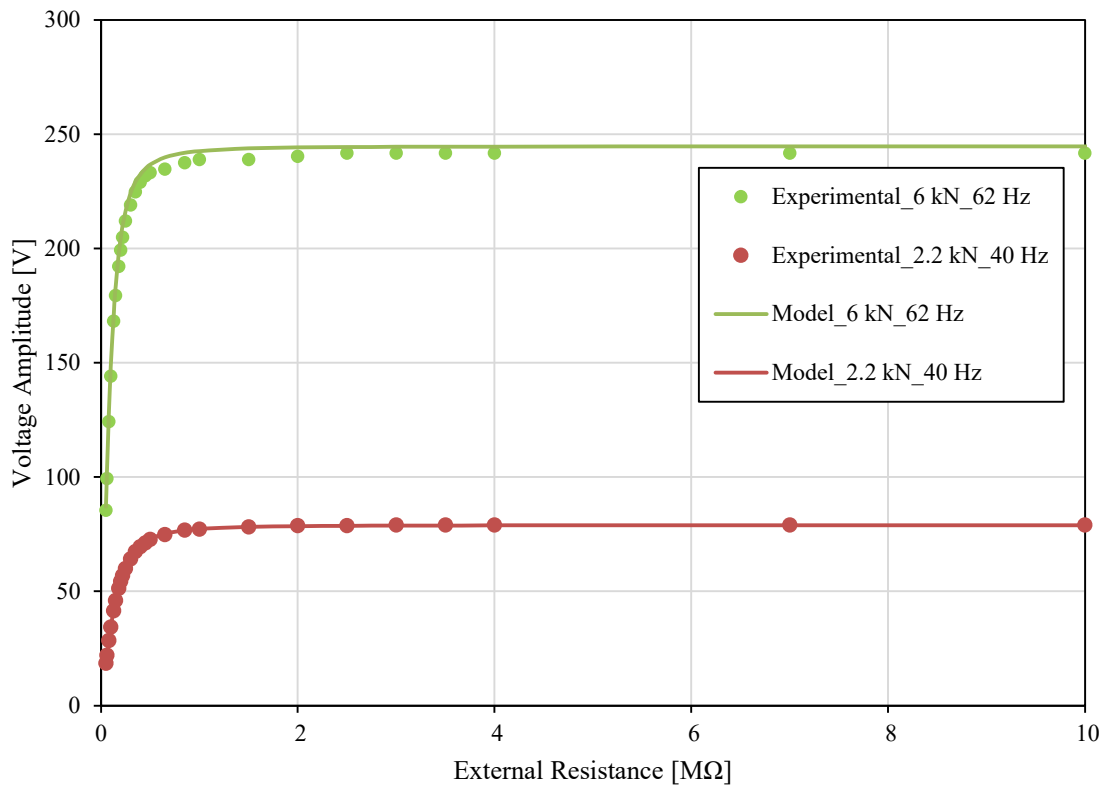


Figure 69. Electro-mechanical model verification using laboratory data obtained for various loads and frequencies for the 4 PZT stacks.

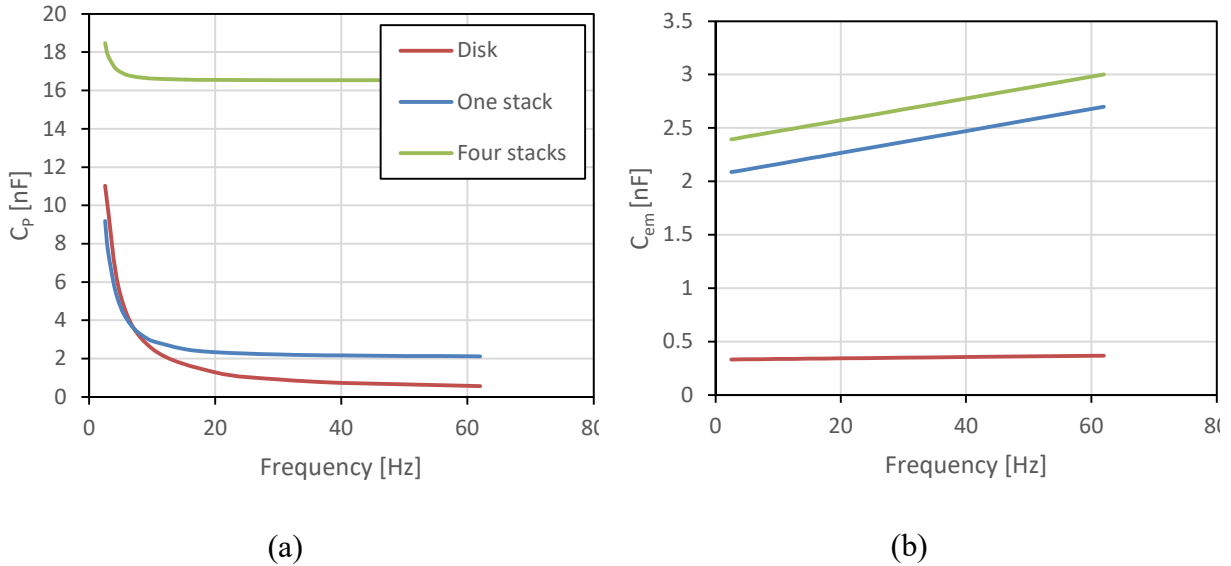


Figure 70. Comparison between the frequency dependent model parameters (a) C_p (b) C_{em} .

4.2.4 In Summary

Electromechanical models were fitted to isolated PZT disks to be used for sensing load and to PZT stacks connected in parallel to be used for energy harvesting purposes. These models were fitted using test data obtained for various loads and frequencies over a range of external resistances. Fitting was done using a Matlab® error minimization routine and the Excel® Solver function, which produced similar results. The quality of fit of the models was verified by predicting the output of the sensors/stacks for conditions different than those used for fitting the models. Details of this work were published by (52).

4.3 WIM Enclosure Design and PZT Sensing Model

4.3.1 WIM Enclosure Design

The WIM enclosure was conceived as a steel box made of AISI 1018 steel (i.e., yield stress of 53.7 ksi) with a top plate supported in each corner by a PZT stack (Figure 71). This box is to be embedded into the roadway pavement flush with the pavement surface. Its dimensions and design were dictated by the need to safely carry the entire load of half a truck axle (i.e., 1 wheel path) and transmit it to the PZT stacks (Figure 72). Its lateral placement in the driving lane is to be determined by well-established vehicle weaving patterns (53).

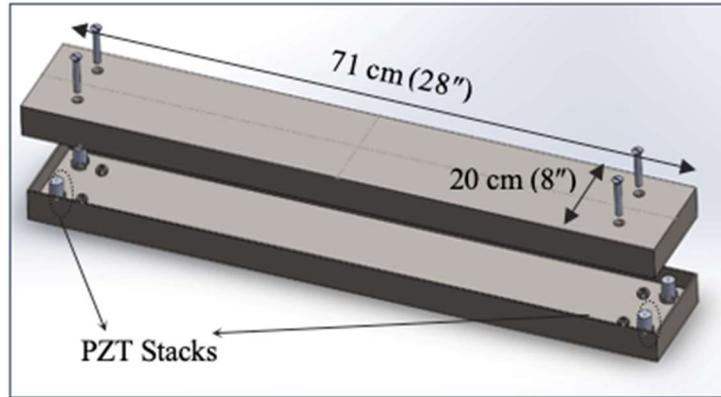


Figure 71. PEH Housing schematic illustrating the location of the 4 PZT stacks.

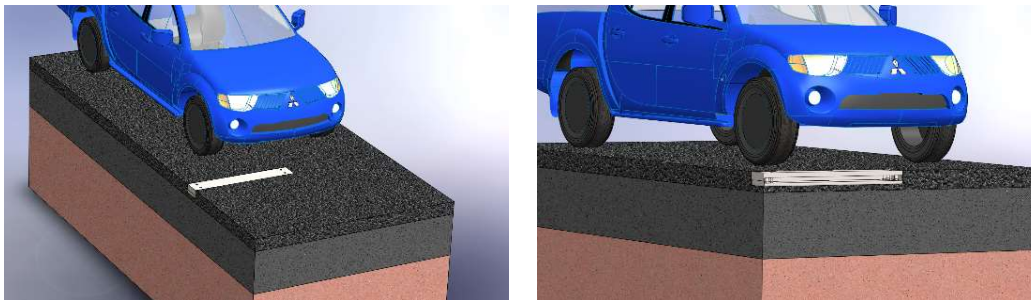


Figure 72. PEH box installed in the road schematic (a) top view (left) (b) section view (right).

The width of the PEH box was selected to be 28 inches in order to cover the right-hand side-wheel path of a driving lane and accommodate typical dual truck tires and their weaving pattern. Its length was selected to be 8 inches, which is sufficient for carrying typical heavy truck tire footprints. A 24 kips truck axle with dual tires and a 13.6 kips with single tires were used to design the thickness of the top plate of the box (Figure 73). It is noted that the first was purposely selected to be over the legal load limit of 20 kips, to account for unavoidable overloaded vehicles.

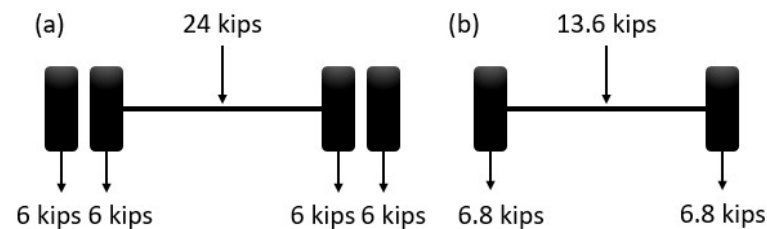


Figure 73. Design axles (a) dual tires (b) single tires.

The top plate under such a loading was analyzed as a simply supported beam (Figure 74). The support is provided by the four PZT stacks located at its corners. The effective width, (i.e., span carrying the tire loads) is 25 inches. The tire footprints were assumed to be square-shaped with dimensions of 8x8 inches carrying uniformly distributed load (Figure 74). The loads were located mid-span to maximize the stresses estimated.

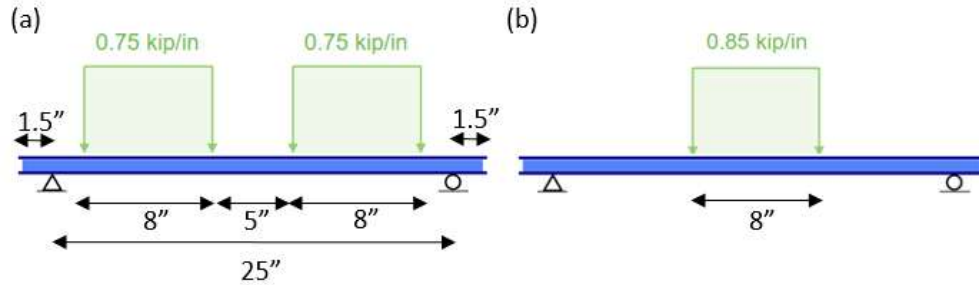


Figure 74. Top plate of the box modelled as simply supported beam a) loading from dual tires b) loading from single tire.

Assuming a thickness of 0.75 inches for the top plate, the maximum stress under the dual tires and the single tires were computed as 48 ksi and 47.6 ksi, respectively. These are below the yield stress of the AISI 1018 steel of 57.3 ksi.

Additional numerical analysis was conducted to refine the design of the PEH enclosure (54). This study performed three-dimensional finite element (FE) simulations of a flexible pavement structure comprising an energy-harvesting module embedded in an asphalt concrete layer using the commercial FE modeling program, i.e., ABAQUS (2015). A static FE simulation provides a structural analysis of the energy harvesting system, revealing stress distributions within the pavement layers, energy-harvesting module, and at their interfaces. The model dimensions were selected to capture the behavior of a typical flexible pavement structure. The model had a length of 6.1 m (20 ft.) and a width of 3.048 m (10 ft.). The thickness of the asphalt concrete layer, hasp, is 30.48 cm (12 in.). The layers below the asphalt layer included a 20.32 cm (8 in.) base, a 15.24 cm (6 in.) subbase, and a 127 cm (50 in) subgrade, as shown in Figure 75. The energy harvesting module dimensions were assumed as 30.48 cm. × 30.48 cm. × 5.08 cm (12in. × 12in. × 2in.), which were in agreement with the dimensions of one of the prototypes that was currently being developed at UTSA. The modules were conceived as two plates sandwiching four piezoelectric elements. The voids are filled by a material that is intended to provide integrity and insulation against water intrusion. For modeling purposes, it was assumed that the sandwiching plates were 0.254 cm (0.1 in.) thick. The FE mesh was designed to focus on the stress area around the module, as shown in Figure 75. The FE mesh was finer near the module and coarser away from it, providing higher resolution in and around the module area. All parts were meshed with 8-node brick elements (C3D8-continuum). A total of 38,160 elements and 44,293 nodes were used in the reference model. The material properties were assumed to be linear elastic. The standard Modulus of Elasticity, E , and Poisson's ratio, ν , values for the analysis are provided in Table 10.

The external boundary conditions were selected to replicate the behavior of an actual pavement structure. The surface of the asphalt concrete layer was free to deform, while the bottom of the subgrade layer was fixed in the vertical direction. The vertical surfaces of all layers were fixed along the x and y directions. Non-slip (i.e., tie) constraints were used between the different layers of the pavement structure (e.g., between asphalt concrete and base layers) and between the faces of the energy-harvesting module and the asphalt layer. This eliminated the numerical complexity in dealing with slip contact algorithms.

The loading cases considered included typical truck tires i.e., single and dual tires and passenger car tires. The truck tires applied a contact load of 44.5 kN (10,000 lbs), under contact pressures of 827.4 kPa and 896.3 kPa (120 and 130 psi) for dual and single tires, respectively. The typical loading for a passenger car tire is 4.45 kN (1,000 lbs), under a contact pressure of 344.74 kPa (50

psi). The contact areas were assumed rectangular with dimensions calculated accordingly as 21.03 cm. × 16.95 cm. (8.25 in. × 6.67 in.), 44.45 cm. × 14.27 cm. (17.5 in. × 5.62 in.) and 19.48 cm. × 7.26 cm. (7.67 in. × 2.86 in.), respectively. The distance between the dual truck tires was assumed as 31.75 cm (12.5 in).

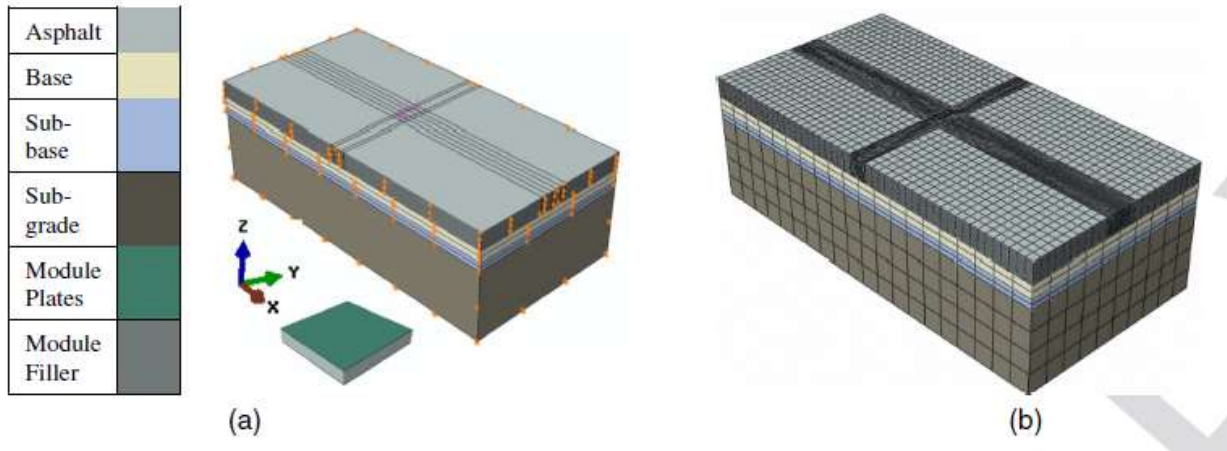


Figure 75. (a) FE model for the static pavement system and the energy-harvesting module (not to scale); and (b) mesh of the pavement structure.

Table 10. Material Properties for the FE Static Analysis

Parts	Elastic Modulus (MPa) ¹	Poisson's ratio (ν)
Asphalt Layer (E_{asp})	3,447 (500)	0.35
Base Layer	552 (80)	0.4
Subbase Layer	276 (40)	0.4
Subgrade Layer	103 (15)	0.45
Module (E_{Mod})	3,447 (500)	0.35
Packing Cover Plates (E_{PC})	6,895 (1,000)	0.4

NOTE: ksi values are provided in parenthesis

The FE analysis suggested that vertical stresses vary with depth in the pavement structure as shown in Figure 76 for each of the static tire loads. It can be observed that the vertical stresses are maximum near the top surface of the pavement and diminish with depth, as expected given Boussinesq's (1855) classic solution. The slight tensile vertical stresses observed near the bottom of the layer are due to the tie constraints imposed between the asphalt concrete layer and the base. Given these results, the top cover of the module should be placed at the top surface of the pavement surface. The design of the top cover of the module should be such that it provides smooth riding conditions for the driver. On the other hand, it is recognized that the module needs to be installed deep enough to allow unimpeded pavement rehabilitation. This is typically in the form of 5.08 cm. (2 in.) milling and overlaying. For this reason, it was assumed that the modules will be installed 5.08 cm. below the pavement surface for the rest of this study.

Figure 76 plots vertical stresses at the top packing plate of the module, given an installation depth of 5.08 cm. (2 in.). It is observed that the maximum vertical stresses are distributed over a wider area than the contact area of the tire, but they are lower in magnitude compared to the surface contact stress, i.e., 710, 765, and 200 kPa (103, 111, and 29 psi) for tires inflated at 827.4, 896.3, and 344.74 kPa (130, 120 and 50 psi), respectively. The maximum corresponding stress on each

PZT stack were calculated as 26,843 kPa, which is well below the 940,000 kPa compressive strength of these materials (47).

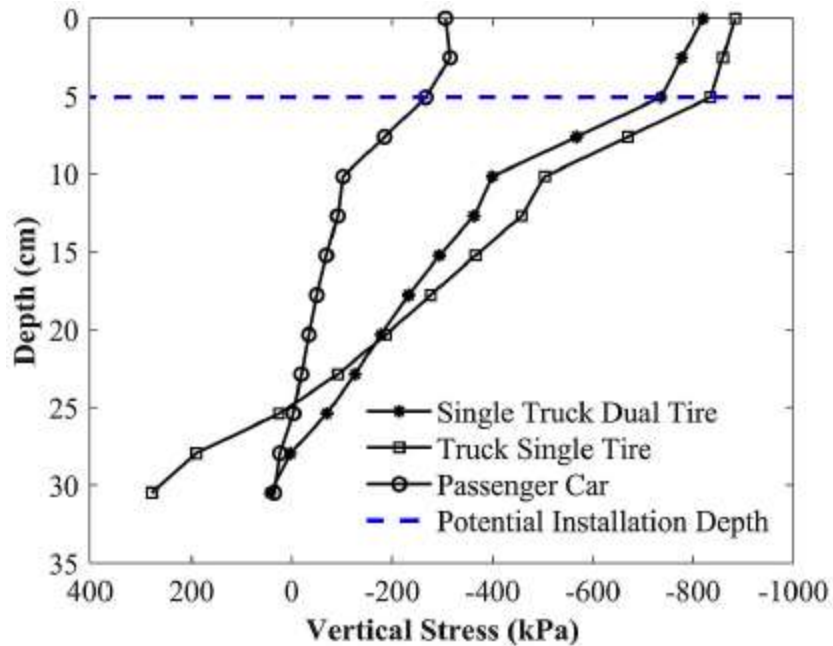


Figure 76. Vertical stresses in the asphalt concrete under the center axis of the load.

Based on conducting various parametric studies (54) , it was concluded that:

- The module should be placed at shallow depths. Ideally, the top cover of the module will be placed at the surface of the pavement surface. Nonetheless, it is recognized that the module should be installed deep enough to allow unimpeded pavement rehabilitation; thus, a 5.048 cm. (2 in.) depth was proposed.
- The numerical analyses revealed that vertical stresses decreased as the thickness of the asphalt layer decreased, suggesting that thick asphalt layers are preferable for the installation of energy harvesting devices.
- The top plate should be rigid enough in order to distribute the stresses evenly over a wide area of the module. However, the FE analyses demonstrated that modules with stiffer upper plates tend to generate tensile stresses close to the edge of the module, which can propagate micro-cracks in this region.
- A soft filler material around the perimeter of the module should be used in order to maximize the load carried by the piezoelectric elements. The FE simulations revealed that the percentage load carried by the piezoelectric elements decreased in an exponential manner as the elastic modulus of the perimeter material increased.

Figure 77 shows the fabricated box housing the four PZT stacks. Its side elements were bolted on because welding would have created warping. For each post, special supports were designed to hold the PZT stacks in place (Figure 78). Each of the sensing PZT elements is to be placed on top of each of the PZT stacks. The thickness of the bottom plate was 0.5 in. As it will described next, the stiffness of the upper plate is critical in limiting its deformation under load to avoid eccentric loading of the stacks supporting the plate.

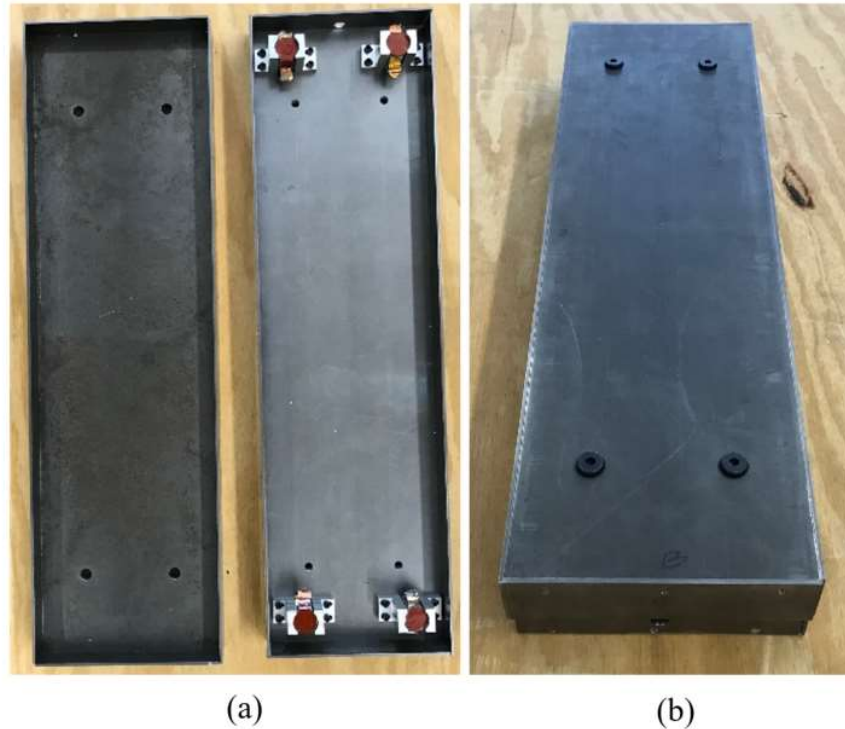


Figure 77. Fabricated PEH box and PZT posts (a) Top/bottom parts (b) Fully assembled box.

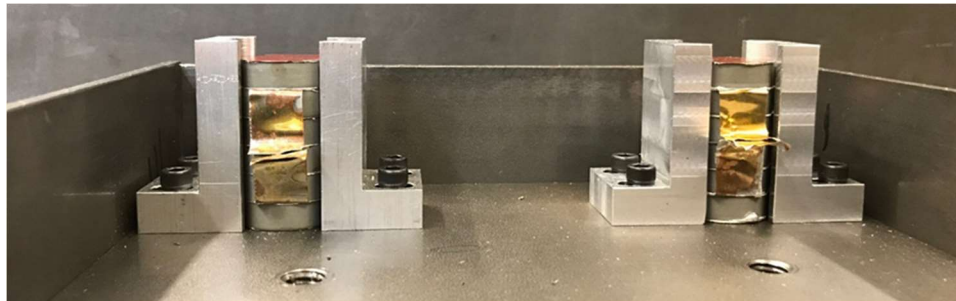


Figure 78. Detail of the PZT stacks and their support inside the PEH enclosure.

4.3.2 Laboratory Testing and PZT Sensor Model Calibration

For laboratory testing purposes, it was necessary to design a scaled-down version of the PEH enclosure that would fit in the UTM testing apparatus. This had dimensions of 16 inches in width by 8 inches in length. The reduced size allowed using a 0.5 inch thick upper plate. The PZT elements selected for sensing the load were slightly different than the ones used for assembling the PZT stacks. Their diameters were the same (i.e., 25.1 mm), but their thickness was slightly lower, that is 6.4 mm as opposed to the 6.8 mm of the PZT stacks. Therefore, it was decided to refit the electromechanical model for the four PZT sensing elements connected in parallel.

The box was subjected to both continuous and pulse loading with an amplitude of 4.4 kN and frequencies ranging from 2.5 Hz to 62 Hz. Figure 79 shows the box inside the UTM. Different diameter plates were used to transfer the load from the actuator, which in effect varied the stiffness of the upper plate. For visual access, one of the side plates of this box was removed. Inside the box, four PZT sensor elements were placed on top of four aluminum columns having the same

dimensions as the PZT stacks. The experimental data from this testing was used to calibrate the electromechanical model with the same methodology described in Section 4.2.

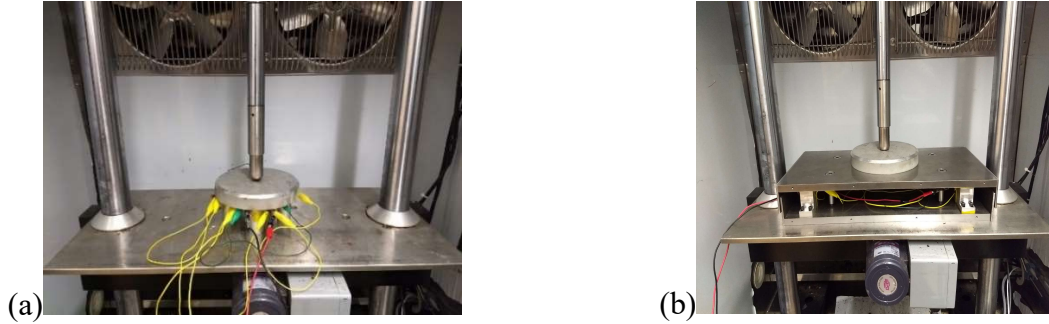


Figure 79. Testing 4 PZT sensors in parallel; (a) Rigid plate, (b) Scaled-down PEH enclosure.

Two approaches were used for fitting the model. The first was identical to the approach used for fitting the PZT stack models (i.e., considering only C_{em} and C_p as frequency dependent). The second explored the idea of allowing ϕ also to be frequency dependent. The voltage output were measured under various external impedances ranging from 50 k Ω to 10 M Ω .

4.3.2.1 Model fitting where ϕ is considered frequency independent

Data for fitting this model was generated with the experimental set up shown in Figure 79(a). The model fitting results from considering only C_{em} and C_p as frequency dependent are shown in Figure 80. The remaining fitted constants, namely R_{em} and L_{em} , and ϕ were 13.009 Ω , 0.033 H, and 0.55, respectively.

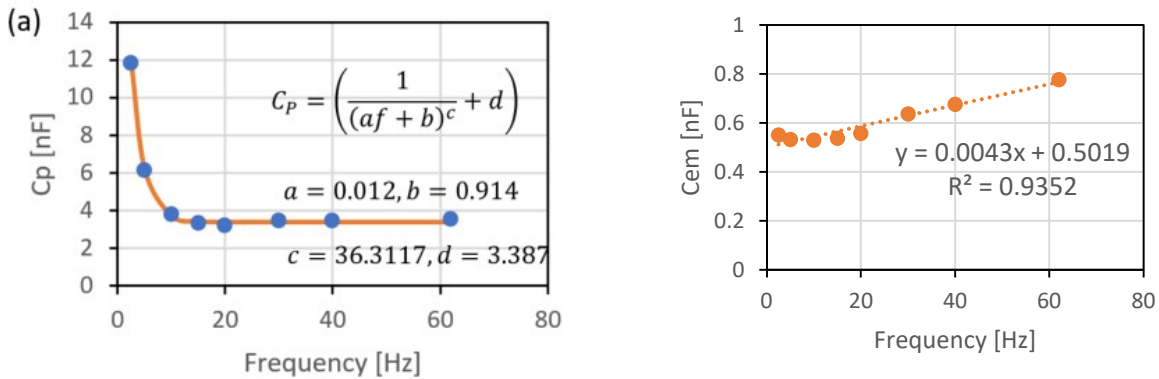


Figure 80. Frequency dependent parameters for PZT sensors; (a) C_p and (b) C_{em} ; ϕ frequency independent.

4.3.2.2 Model fitting where ϕ is considered frequency dependent

Data for fitting this model was generated with the experimental set up shown in Figure 79(b). The model fitting results for the frequency dependent parameters C_{em} and C_p and ϕ are shown in Figure 81 and Figure 82. The remaining fitted constants, namely R_{em} and L_{em} , were 13.009 Ω and 0.033 H, respectively.

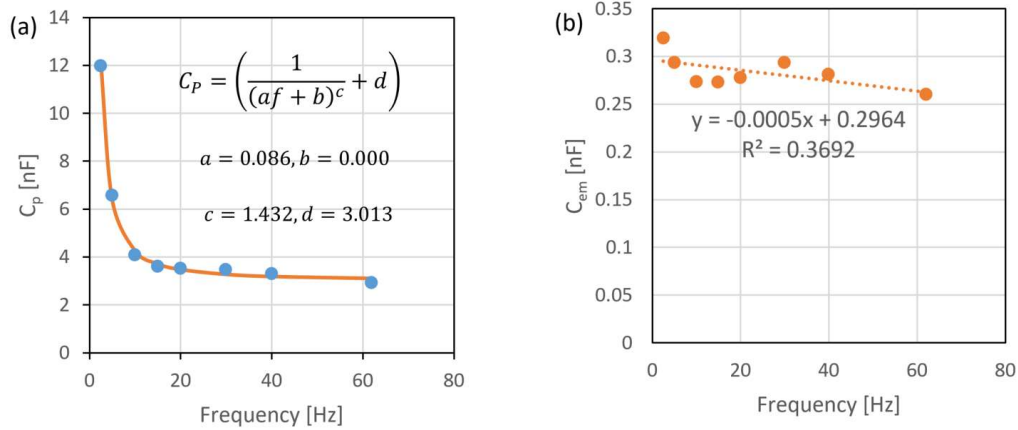


Figure 81. Frequency dependent parameters for PZT sensors; (a) C_p and (b) C_{em} ; ϕ frequency dependent.

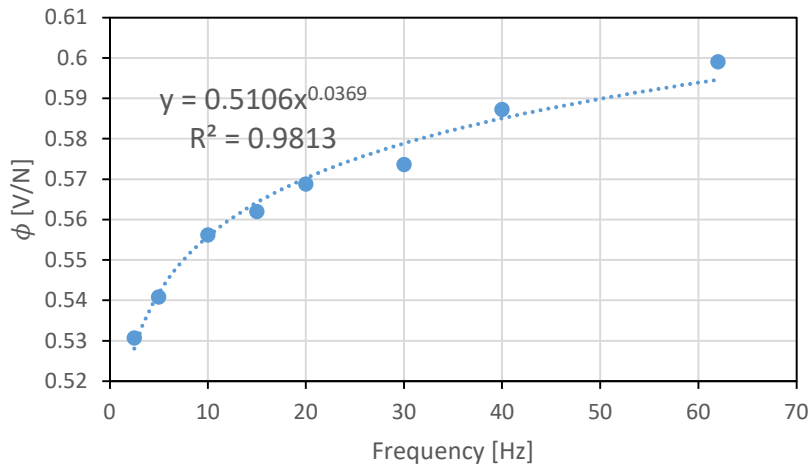


Figure 82. The fitted parameter ϕ as a function of loading frequency.

4.3.2.3 Model verification

The fitted models were verified by comparing their output to experimental data obtained under load and frequency conditions different than the ones used for calibration. The quality of fit of the first model (Section 4.3.2) is excellent as shown in Figure 83. This, however, was not the case for the second model (also shown in Section 4.3.2), although it allowed for ϕ to be frequency dependent (Figure 84). The poor fit of the second model was attributed to the flexibility of the upper plate shown in Figure 79(b), which resulted in a non-uniform distribution of stresses on the top of the 4 PZT sensing elements. This in turn produced a nonlinear relationship between output voltage and applied force (Figure 85). As discussed earlier, this relationship is expected to be linear regardless of the external resistance and the loading frequency (Figure 33 and Figure 35). The quality of fit of the second model improved when the data used was generated using an experimental set up that provided additional stiffness through the insertion of a rigid beam (

Figure 86). This set up restored the linearity in the relationship between force and voltage output (Figure 87). This analysis pointed out the importance of having a very stiff PEH enclosure upper plate.

4.3.2.4 Selecting a PZT sensor model

To conclude this analysis, the PZT sensor model with the frequency dependent ϕ was refitted using the rigid plate experimental set up shown in Figure 79(a). Its quality of fit was compared to that for the model considering ϕ as being frequency independent. Figure 88 shows that under these testing conditions, the quality of fit of these two models is practically identical. Therefore, it was decided to select the simpler model for implementation (i.e., the one where the ϕ was frequency independent (i.e., the model described in Section 4.3.2). This model is hence referred to as PZT sensor Model 1. As explained in Section 4.4, there were some differences between the nominal frequencies input into the UTM machine and the ones actually applied, which necessitated refitting the PZT sensor model.

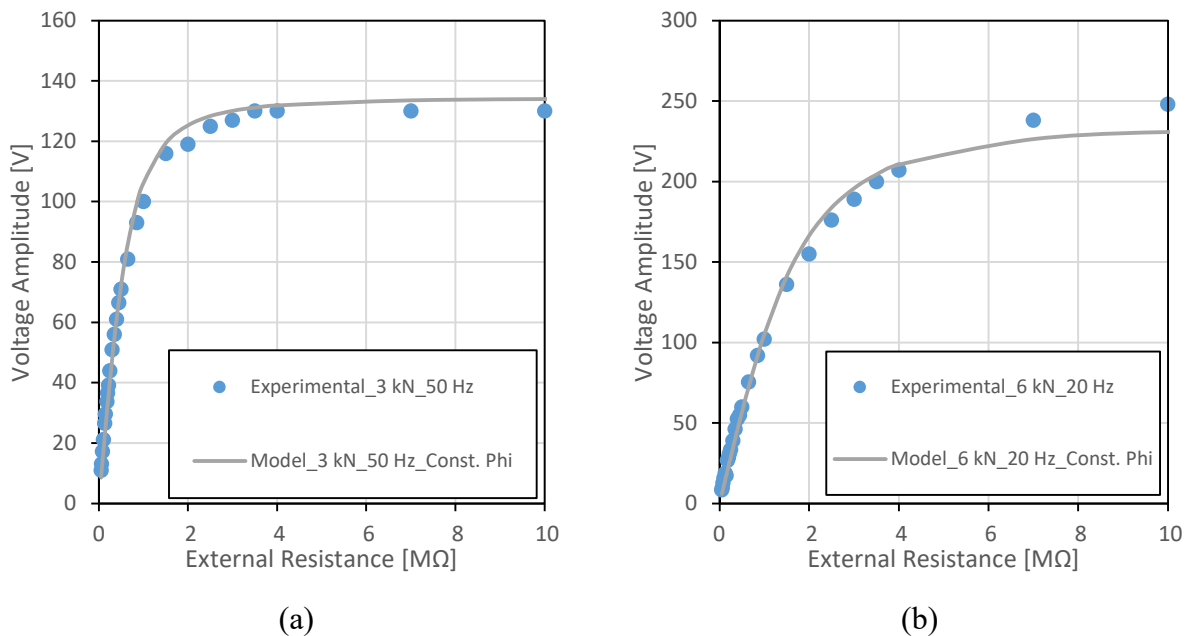
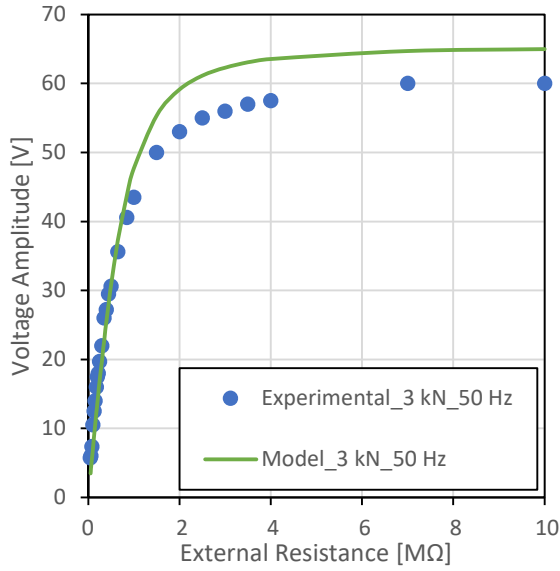
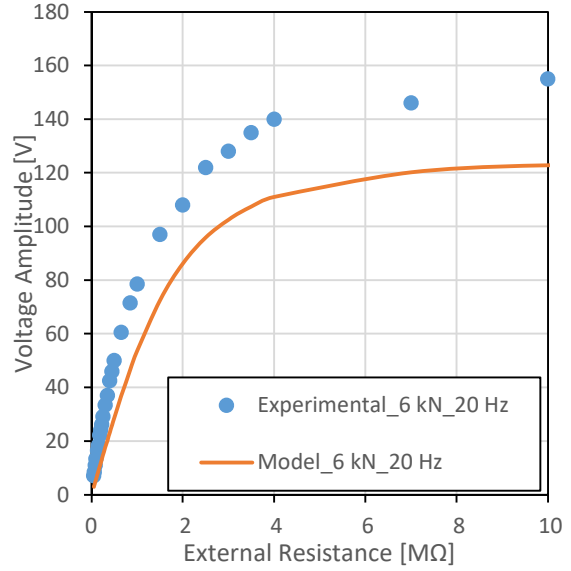


Figure 83. Sensors model verification for (a) 3 kN 50 Hz (b) 6 kN 20 Hz.



(a)



(b)

Figure 84. Sensors model verification for (a) 3 kN 50 Hz (b) 6 kN 20 Hz.

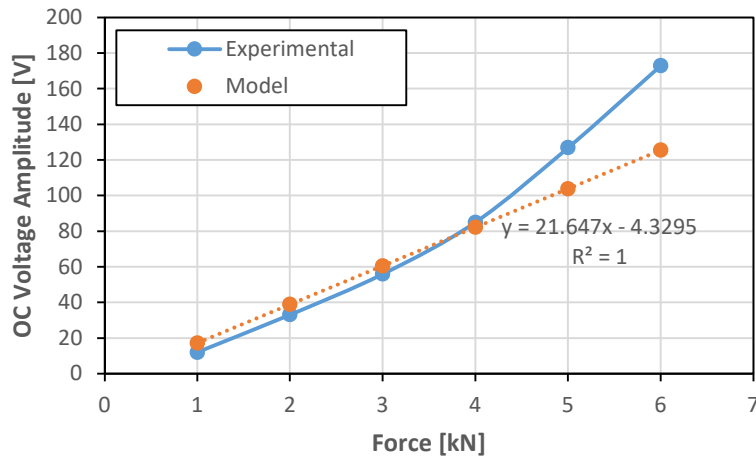


Figure 85. OC voltage versus force for four PZT sensors under 20 Hz for the experimental set up in 5-7(b).



Figure 86. Test setups in order to evaluate the effect of rigidity of the top plate.

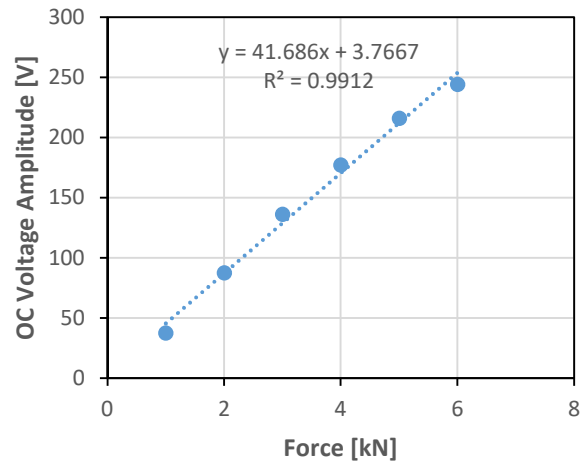


Figure 87. Voltage versus force for the experimental set up in 5-7(a).

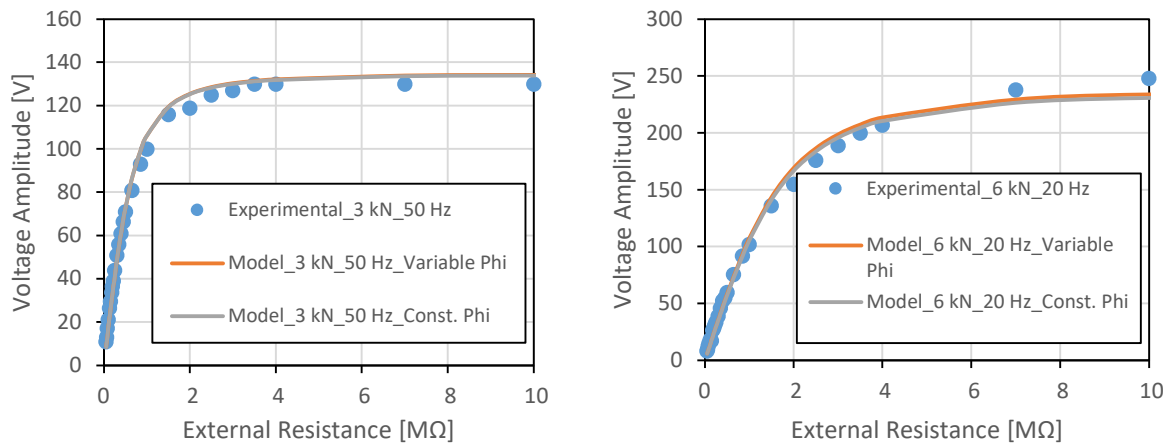


Figure 88. Four PZT Sensor model comparison using data generated from the experimental set up in Figure 79(a); (a) 3 kN 50 Hz (b) 6 kN 20 Hz.

4.3.3 In Summary

This section described the design considerations in developing the WIM system enclosure. It included a detailed analysis of its dimensions and structural components in conjunction with the fitting of the electromechanical model for the 4 PZT elements connected in parallel that will serve as the WIM sensors. It pointed out the need for a very stiff enclosure upper plate to limit flexing that cause eccentric loads on the sensors which skew their linearity. As a result, it was decided to add another 0.75 inch bolt-on plate on top of the WIM enclosure box, as described later (i.e., this brings the total thickness of the upper plate to 1.5 inches). Finally, it was concluded that the simpler model shown in Figure 80 involving a frequency independent electromechanical coefficient ϕ is preferable. This model will be referred to as PZT sensor Model 1, because as explained later several variations of this model were tested. This model, after being revised for the actual frequencies applied by the UTM system, will be implemented into the load sensing algorithm described next.

4.4 WIM AND CLASSIFICATION ALGORITHMS

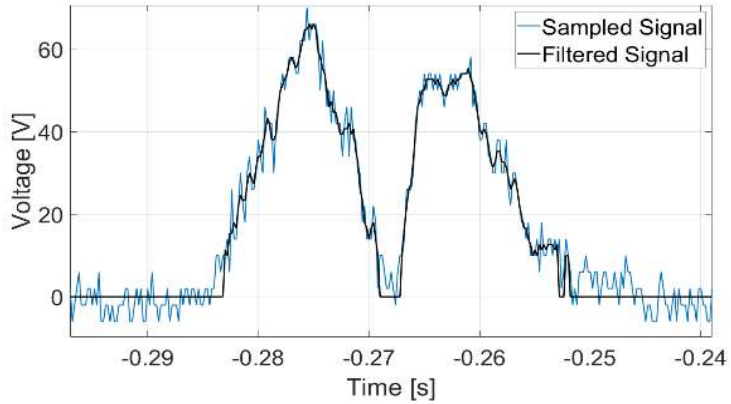
This section describes the algorithms used for conditioning the output of the 4 PZT sensors connected in parallel and subsequently using it in estimating loading frequency/vehicle speed, axle spacing, axle load and finally vehicle class. An external resistor of 450 k Ω was used. Loads were applied with the UTM machine and voltages were measured with the oscilloscope described earlier using a sampling rate of 5 kHz and a 500x attenuation voltage probe. Two methods were used for implementing this algorithm:

- A code written in Matlab®, which allowed refining the algorithm through laboratory testing.
- A code written in C by translating the Matlab® code mentioned above into a format suitable for loading into the MCU, which serves as the DAQ for the WIM system and allowed further laboratory and field testing.

4.4.1 Signal Conditioning

The analogue PZT sensor voltage output is rectified to reverse its negative component, filtered to reduce its noise and scaled down to the 0 to 3.3 Volt input range of the MCU. The rectifying and scaling down of the signal is shown schematically in Figure 89. The raw signal from the passage of an axle has a positive and a negative component. Its negative component is reversed to positive using a rectifier. Then the signal is filtered using a 3-point moving average to reduce electronic noise. This step may be unnecessary, if the actual MCU noise is shown to be negligible. Finally

the signal is scaled down to the 0 to 3.3 Volt range using a voltage divider. Examples of rectified



and filtered signals are shown in

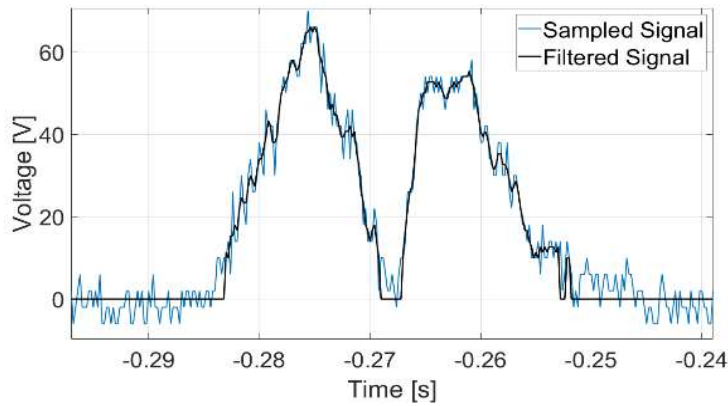


Figure 90(a) and

Figure 90(b) for 4.4 kN load at 30 Hz and a 11 kN load at 62 Hz, respectively. These represent loadings from a slow moving passenger car tire and a fast moving light truck tire, respectively.

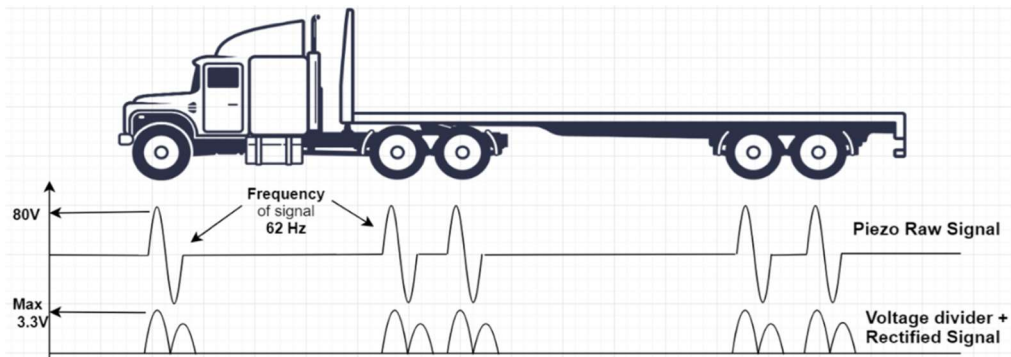


Figure 89. Schematic of the raw voltage output, the rectified and scaled down voltage.

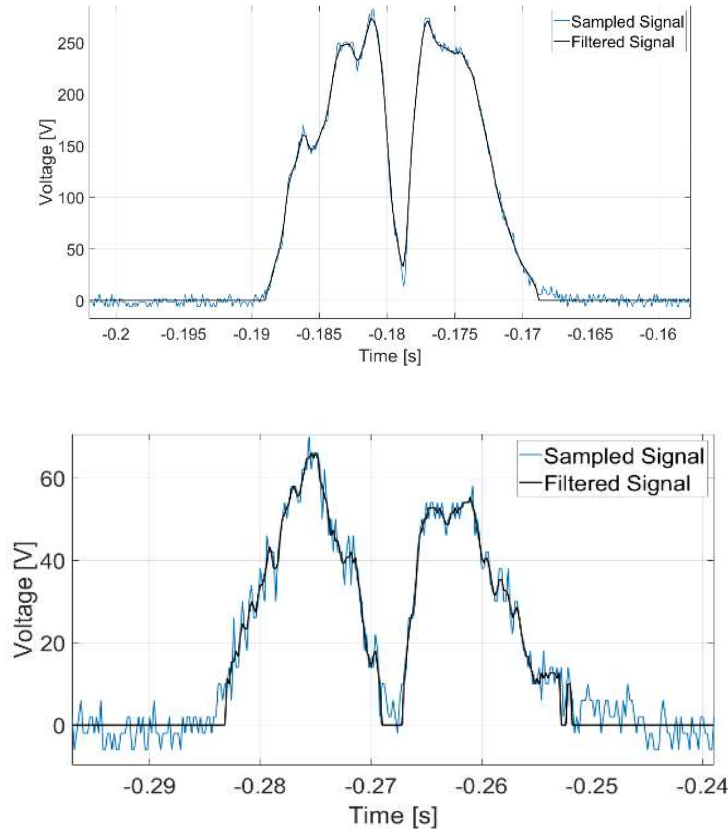
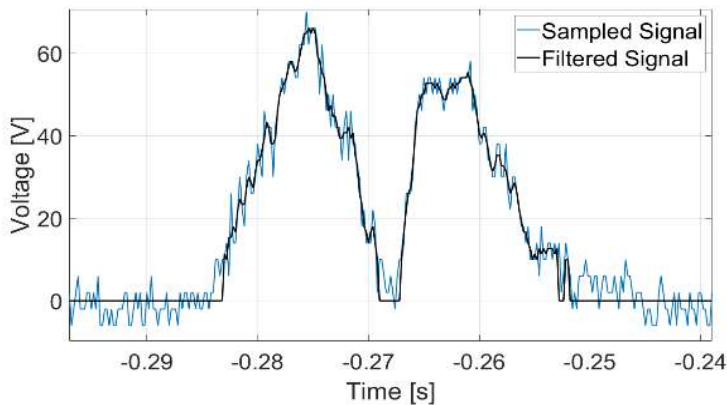


Figure 90. Signal before and after the filtering; (a) 4.4 kN at 30 Hz (b)11 kN at 62 Hz.

Figure 91 shows the oscilloscope reading for repeated pulses of the 4.4 kN, 30 Hz load. These figures suggest the need to filter and analyze the electronic noise level. After filtering the signal using a 3-point moving average, noise was analyzed by considering signals over a 0.1 sec period before the load was applied (Figure 92). Noise statistics are shown in Table 11, which suggests that post-filtering the oscilloscope generates maximum noise levels of about 8 Volts. As a result, it was decided to set the noise level cutoff at 9 Volts and set measurements lower than that to zero



(e.g.,
Figure 90).

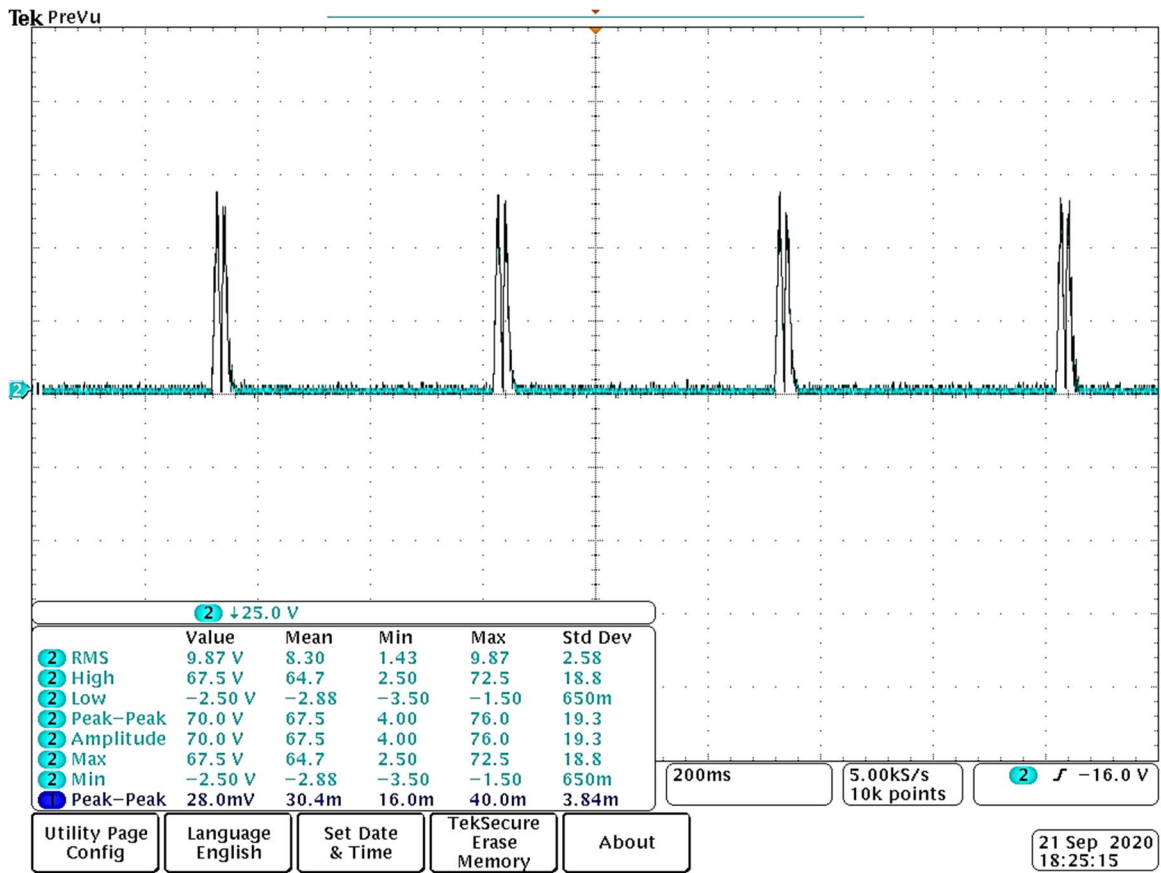


Figure 91. Oscilloscope measurement for a 4.4 kN 30 Hz load; Oscilloscope resolution of 25 V/division.

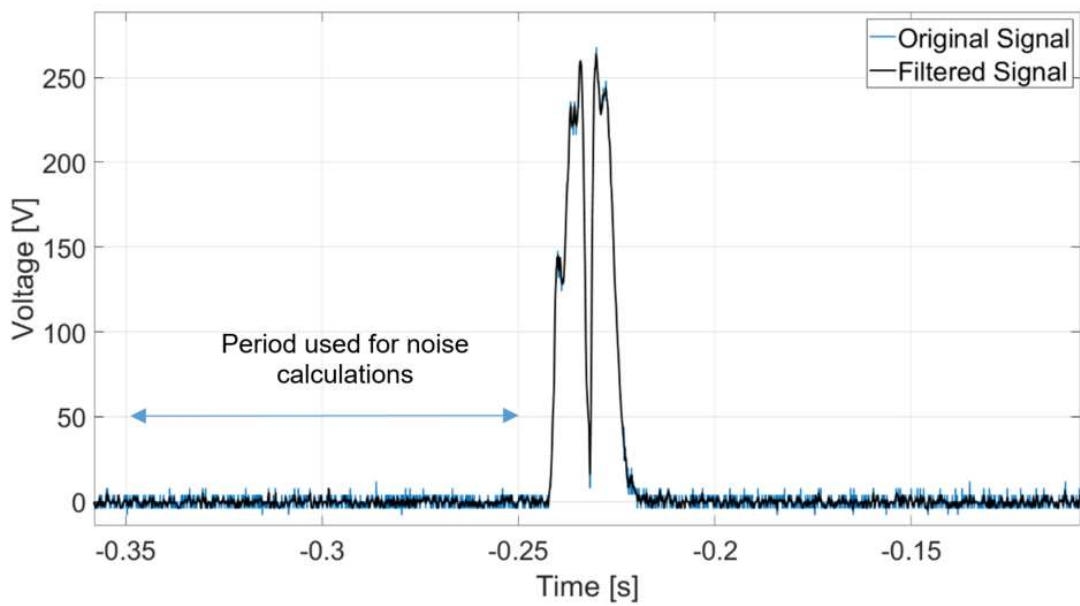


Figure 92. Rectified four PZT sensor output in response to a load of 11 kN at 62 Hz.

Table 11. Oscilloscope electronic noise.

Noise (Volts)	Average	Standard Deviation	Minimum	Maximum
Before Filtering	-0.30	3.16	-8	12
After Filtering	-0.30	1.83	-5.33	8

Accordingly, the signal to noise ratios for the signals in

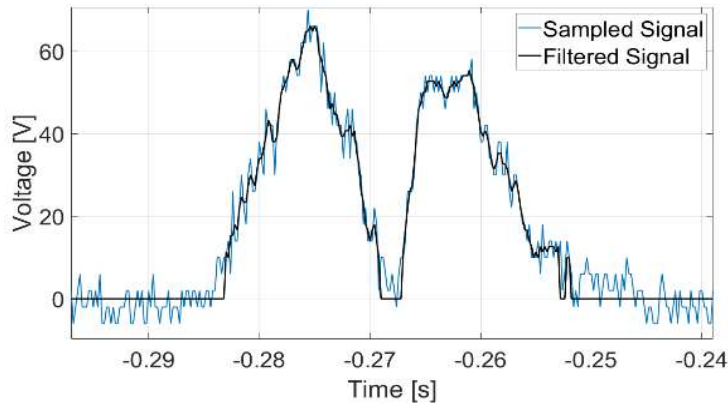
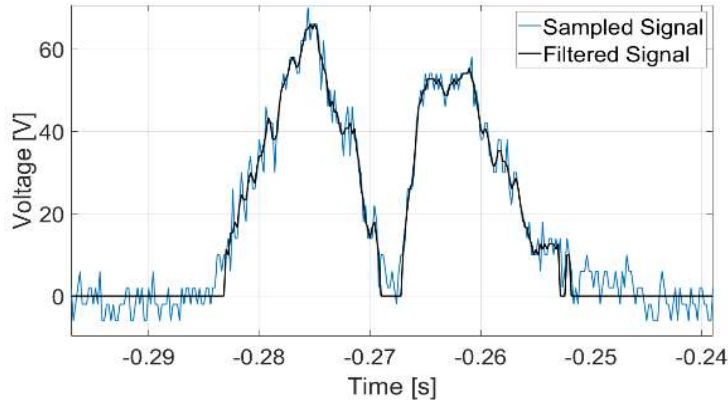


Figure 90(a) and

Figure 90(b) are in the order of $70/8$ and $300/8$, which are considered significant for weighing even light passenger car tires.

The processed signal was scaled down using a voltage divider. In selecting resistances for this divider, the extreme voltages estimated from the PZT sensor model were considered. These were estimated for the lightest/slowest tire (i.e., passenger moving at 30 mph) to the heaviest/fastest tire (i.e., overloaded truck moving at 60 mph). The corresponding loads and frequencies were 4.4 kN at 33 Hz and 44 kN at 66 Hz and the estimated voltage amplitudes were 58.4 Volts and 1,392 Volts. Details of calculating loading frequency from vehicle speed are given in the next Section. Scaling down this maximum voltage to 3.3 Volts requires splitting the 450 k Ω resistor into two parts, one 1,066 Ω and the other 448,934 Ω . These values need to be rounded to the nearest commercially available resistor values, while keeping the maximum voltage below 3.3 Volts. Voltage measurements across the smaller resistor are input into the MCU.

4.4.2 Frequency/Vehicle Speed Estimation

An essential input in estimating tire loads is the loading frequency f , which can be calculated as the inverse of the time duration Δt of the load pulse applied by tires. This in turn is directly related to the vehicle speed and allows estimating axle spacing and hence vehicle classification. Assuming a circular tire footprint of a diameter of 8 inches, Δt is the time it takes for this footprint to traverse the 8-inch long WIM enclosure (i.e., a combined distance of 16 inches). For example, a tire travelling at 50 mph (73.33 ft/sec) takes 0.01818 sec to traverse the combined distance of 16 inches. This corresponds to a loading frequency f of 55 Hz. As described in Section 4.5, the time it takes for a state-of-the-art MCU to “wake up” and begin recording is in the order of 15 μ s, which allows the WIM system to accurately record the speed of even the first axle of a vehicle after a long time of inaction. This allows the proposed WIM system to “wake up” and detect vehicle speed without resorting to inductive loops, which represents considerable savings over conventional WIM systems.

An important consideration in processing the PZT sensor signals for estimating loading frequency and in turn load is the sampling frequency allowed by the MCU. Clearly, the higher the sampling frequency, the higher the memory required for storing the data and consequently, the higher the power requirements for the MCU. As described in Section 4.5, two MCU types were tested, one with a sampling frequency of 1.2 kHz and another with 2.5 kHz. These frequencies are lower than the 5 kHz sampling frequency of the oscilloscope. Therefore, the digital oscilloscope signals were processed to simulate the MCU sampling frequency (e.g., reading every second data point of the rectified signal artificially reduced the sampling frequency from 5 to 2.5 kHz).

Figure 93 and Figure 94 show examples of rectified oscilloscope pulses under a 4.4 kN load at 30 Hz and a 8 kN load at 62 Hz, respectively. These figures also include the simulated sampled signal obtained using a 2.5 kHz MCU sampling frequency and the filtered simulated signal using the 3-point moving average. The time interval Δt was estimated analytically from the full signal width. The beginning and end of the filtered signal were identified by voltages exceeding zero. For light loads, (i.e., the 4.4 kN applied by car tires), the effect of the noise could be significant and affect the estimation of the Δt and hence, lower the accuracy in predicting frequency and in turn load as shown in Figure 93.

Another issue related to light loads at low speeds is that the voltage measurements between the two peaks of the rectified and filtered signal generated by a tire may fall below the 9 Volts noise cut off (e.g., Figure 93). The algorithm considers these as a single peak, if the duration of this noise-level voltage is very short. A duration of 0.0034 sec was selected as the cut off value. This value was established experimentally by testing a wide range of tire loads and frequencies. It is noted, that this time cutoff is much lower than the time interval between the peaks generated by two closely spaced axles. For example, the time interval between the peaks generated by a set of tandem axles spaced 6 feet apart moving at 30 mph, is 0.106 sec. Hence, the algorithm can differentiate between the pulses generated by single versus double axles even at low speeds.

Processing the data shown in Figure 93 and Figure 94 yields Δt values of 0.0292 sec and 0.0196 sec, which translate to loading frequencies of 34.24 Hz and 51 Hz, respectively. There is clearly a discrepancy between the frequencies dialed in the UTM and the ones detected by the algorithm. As discussed next, this was due to the limitations of the UTM in applying high loads at high

frequencies and necessitated the differentiation between nominal (i.e., frequencies dialed into the UTM) and actual frequencies (i.e., frequencies actually applied to the sensors).

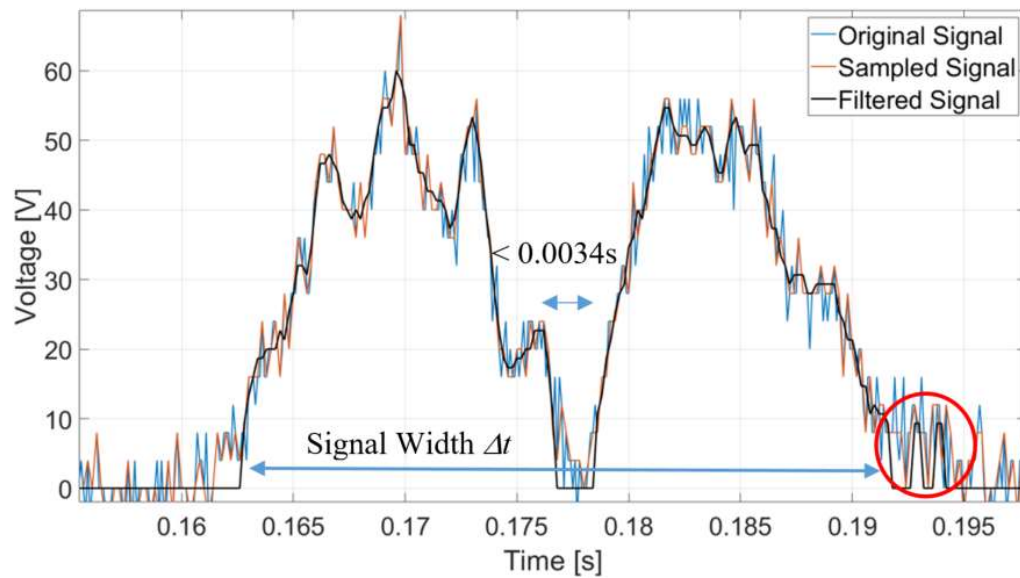


Figure 93. Sensor output of a 4.4 kN 30 Hz load.

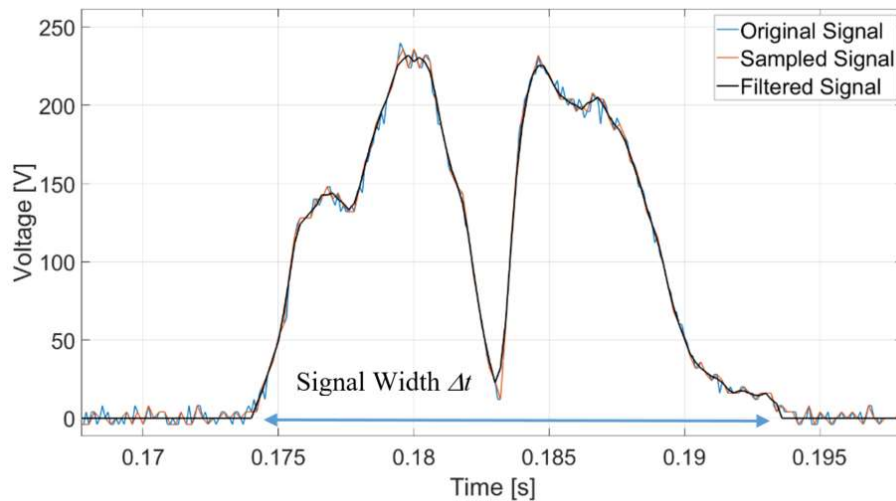


Figure 94. Sensor output for an 8 kN load at 62 Hz.

4.4.3 Nominal versus Actual Test Frequencies

The differences between nominal and actual frequencies were established by two methods. First, manually by estimating the Δt of pulses from the oscilloscope readings and second by the algorithm developed. The results are shown in Table 12 and Table 13 respectively. They confirm the pattern that as the loads applied are increased, the actual frequencies applied by the UTM are gradually reduced. This is an inherent limitation of servo-hydraulic testing systems. Considering that the manual method for measuring Δt is accurate, it was used as the reference for evaluating

the accuracy of the algorithm output in estimating loading frequency and hence, loading speed. The resulting errors are shown in Table 14.

Table 12. Nominal versus actual frequencies established from manual Δt measurements.

	Nominal Frequencies Hz			
	30	40	50	62
Load Amplitude kN	Average Actual Frequencies (Manual calculation of 4 tests)			
4.4	32.89	43.1	51.55	57.47
11	31.05	39.37	49.02	47

The oscilloscope resolution was set at 100 V

Table 13. Nominal versus actual frequencies established from the algorithm.

	Nominal Frequencies Hz			
	30	40	50	62
Load Amplitude kN	Average Actual Frequencies (Algorithm calculation of 4 tests)			
4.4	35.88	44.26	53.04	59.19
6	33.78	40.98	43.10	42.37
11	31.75	40.90	48.92	50.50

Table 14. Estimated algorithm errors in estimating vehicle speed.

	Nominal Frequencies Hz			
	30	40	50	62
Load Amplitude kN				
4.4	9.09%	2.69%	2.89%	2.99%
11	2.25%	3.89%	-0.20%	7.45%

4.4.4 Refitting the PZT Sensing Model Using Actual Frequencies

The discrepancy between nominal and actual loading frequencies discussed above necessitated refitting the electromechanical models of the 4 PZT sensor elements using the actual loading frequencies applied (Table 12). As for Model 1 (i.e., Section 4.3.2), testing for Model 2 was done under the rigid UTM disk and the range of external resistances used were 50 k Ω to 10 M Ω . The fitted model, referred to as Model 2, is shown in Figure 95. The corresponding fitted constants, namely R_{em} and L_{em} , and ϕ were the same as for Model 1 (i.e., 13.009 Ω , 0.033 H, and 0.55, respectively).

One additional model was fitted using the actual frequencies and the 4 PZT sensors placed inside a scaled-down version of the WIM box. A narrower range in external resistances was used (i.e., 50 k Ω to 1 M Ω), to better match the external 450 k Ω resistance used. The fitted model, referred to

as Model 3, is shown in Figure 96. As for Models 1 and 2, Model 3 fitted constants, namely R_{em} and L_{em} , and ϕ were the same (i.e., 13.009 Ω , 0.033 H, and 0.55, respectively). The accuracy of these models in measuring loads will be further discussed in Section 5.1 of this report.

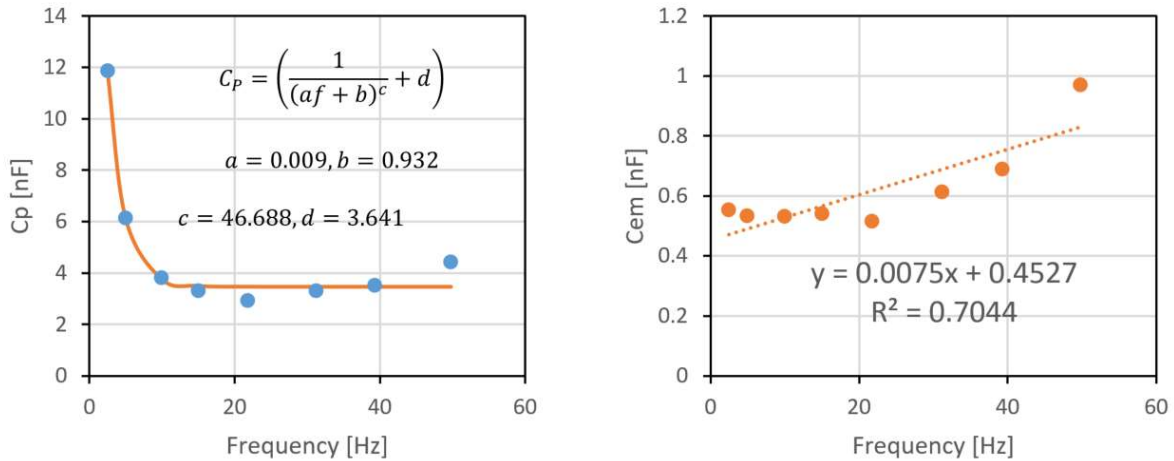


Figure 95. Model 2 fitted using actual frequencies; External resistances 50 k Ω to 10 M Ω .

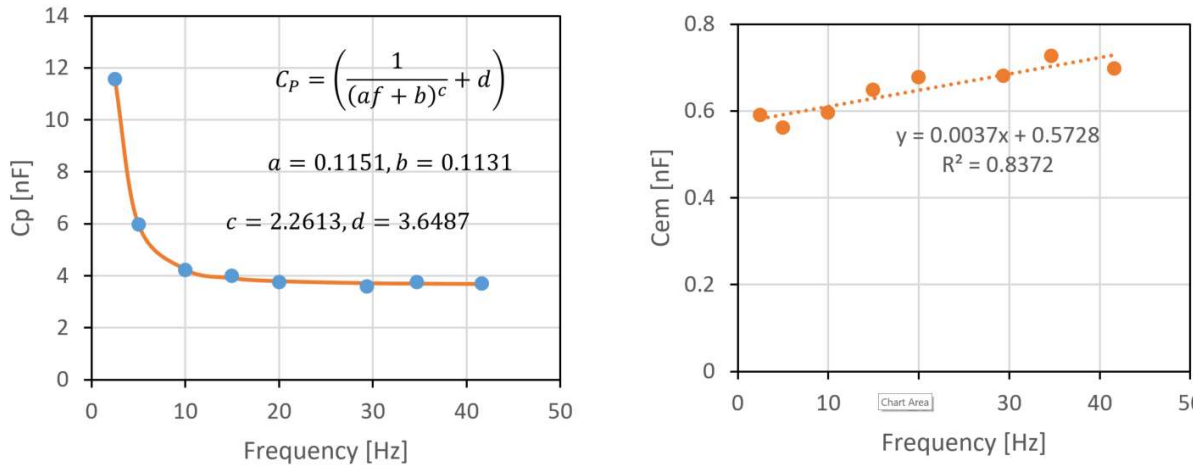


Figure 96. Model 3 fitted using actual frequencies; External resistances 50 k Ω to 1 M Ω .

4.4.5 Classification Algorithm

The vehicle classification algorithm implemented is based on axle spacings and axle loads. It takes into account the:

- Number of axles on the vehicle.
- Spacing between those axles.
- Weight of the first axle on the vehicle.
- Gross vehicle weight of the vehicle.

It was developed for the Long-Term Pavement Performance (LTPP) and adopted by the AASHTO Expert Task Group in 2006 (Table 15). It is considered to be more accurate than the simpler classification scheme that relies only on axle spacing (i.e., Figure 2) because it can differentiate

between classes of vehicles with similar axle space “signatures” (e.g., a pickup truck towing a boat trailer and a truck with 4 axles).

Table 15. Vehicle Classification Algorithm (55).

Class	Vehicle Type	No. of Axles	Spacing (ft) Between Axles 1 and 2	Spacing (ft) Between Axles 2 and 3	Spacing (ft) Between Axles 3 and 4	Spacing (ft) Between Axles 4 and 5	Spacing (ft) Between Axles 5 and 6	Spacing (ft) Between Axles 6 and 7	Spacing (ft) Between Axles 7 and 8	Spacing (ft) Between Axles 8 and 9	GVW Min-Max (Kips)	Axle 1 Weight Min(Kips)¹
1	Motorcycle	2	1.00-5.99	----	----	----	----	----	----	----	0.10-3.00	----
2	Passenger Car		6.00-10.10	----	----	----	----	----	----	----	1.00-7.99	----
3	Other (Pickup/Van)		10.11-23.09	----	----	----	----	----	----	----	1.00-7.99	----
4	Bus		23.10-40.00	----	----	----	----	----	----	----	12.00 >	----
5	2D Single Unit		6.00-23.09	----	----	----	----	----	----	----	8.00 >	2.5
2	Car with 1 Axle Trailer	3	6.00-10.10	6.00-25.00	----	----	----	----	----	----	1.00-11.99	----
3	Other with 1-Axle Trailer		10.11-23.09	6.00-25.00	----	----	----	----	----	----	1.00-11.99	----
4	Bus		23.10-40.00	3.00-7.00	----	----	----	----	----	----	20.00 >	----
5	2D with 1-Axle Trailer		6.00-23.09	6.30-30.00	----	----	----	----	----	----	12.00-19.99	2.5

6	3-Axle Single Unit		6.00-23.09	2.50-6.29	----	----	----	----	----	----	12.00 >	3.5
8	Semi, 2S1		6.00-23.09	11.00-45.00	----	----	----	----	----	----	20.00 >	3.5
2	Car with 2-Axle Trailer	4	6.00-10.10	6.00-30.00	1.00-11.99	----	----	----	----	----	1.00-11.99	----
3	Other with 2-Axle Tr.		10.11-23.09	6.00-30.00	1.00-11.99	----	----	----	----	----	1.00-11.99	----
5	2D with 2-Axle Trailer		6.00-26.00	6.30-40.00	1.00-20.00	----	----	----	----	----	12.00-19.99	2.5
7	4-Axle Single Unit		6.00-23.09	2.50-6.29	2.50-12.99	----	----	----	----	----	12.00 >	3.5
8	Semi, 3S1		6.00-26.00	2.50-6.29	13.00-50.00	----	----	----	----	----	20.00 >	5.0
8	Semi, 2S2		6.00-26.00	8.00-45.00	2.50-20.00	----	----	----	----	----	20.00 >	3.5
3	Other with 3-Axle Trailer	5	10.11-23.09	6.00-25.00	1.00-11.99	1.00-11.99	----	----	----	----	1.00-11.99	----
5	2D with 3 Axle Trailer		6.00-23.09	6.30-35.00	1.00-25.00	1.00-11.99	----	----	----	----	12.00-19.99	2.5
7	5-Axle Single Unit		6.00-23.09	2.50-6.29	2.50-6.29	2.50-6.30	----	----	----	----	12.00 >	3.5

9	Semi, 3S2			6.00-30.00	2.50-6.29	6.30-65.00	2.50-11.99	----	----	----	----	20.00 >	5.0
9	Truck+Full Tr. (3-2)			6.00-30.00	2.50-6.29	6.30-50.00	12.00-27.00	----	----	----	----	20.00>	3.5
9	Semi, 2S3			6.00-30.00	16.00-45.00	2.50-6.30	2.50-6.30	----	----	----	----	20.00 >	3.5
11	Semi+Full Trailer, 2S12			6.00-30.00	11.00-26.00	6.00-20.00	11.00-26.00	----	----	----	----	20.00 >	3.5
10	Semi, 3S3		6	6.00-26.00	2.50-6.30	6.10-50.00	2.50-11.99	2.50-10.99	----	----	----	20.00 >	5.0
12	Semi+Full Trailer, 3S12			6.00-26.00	2.50-6.30	11.00-26.00	6.00-24.00	11.00-26.00	----	----	----	20.00 >	5.0
13	7-Axle Multi-trailers		7	6.00-45.00	3.00-45.00	3.00-45.00	3.00-45.00	3.00-45.00	3.00-45.00	----	----	20.00 >	5.0
13	8-Axle Multi-trailers		8	6.00-45.00	3.00-45.00	3.00-45.00	3.00-45.00	3.00-45.00	3.00-45.00	3.00-45.00	----	20.00 >	5.0
13	9-Axle Multi-trailer		9	6.00-45.00	3.00-45.00	3.00-45.00	3.00-45.00	3.00-45.00	3.00-45.00	3.00-45.00	3.00-45.00	20.00 >	5.0

4.4.6 Data output format

Data is stored in a Secure Digital (SD) memory card following the standardized “W-record” format specified by the FHWA (56) (Table 16). This is the format used by most commercial WIM systems. It includes the number, spacing, and weight of axles by vehicle, as well as vehicle class and GVW. The length of the data corresponding to individual vehicles is defined by the number of axles per vehicle. The maximum record size is 268 columns that can accommodate a 25 axle vehicle. Using the 16 MB internal memory of the MCU and 4 byte sized columns, data from a total of 60,000 individual vehicles can be stored. Hence, traffic data size is not an issue for the RAM storage available nor for the expandable SD memory card.

Table 16. Standardized Vehicle W-Record Format (TMG 2016).

Field	Columns	Width	Description	Type
1	1	1	Record Type	C
2	2-3	2	FIPS State Code	C
3	4-9	6	Station ID	C
4	10	1	Direction of Travel code	C
5	11	1	Lane of Travel	C
6	12-15	4	Year of Data	C
7	16-17	2	Month of Data	C
8	18-19	2	Day of Data	C
9	20-27	8	Time of Data	C
10	28	1	W	C
11	29-32	4	Vehicle Signature/Other Use	O
12	33-36	4	Vehicle Speed	C
13	37-38	2	Vehicle Classification	C
14	39-40	2	Number of Axles	C
15	41-44	4	Total Vehicle Length (bumper to bumper)	O
16	45-47	3	Pavement Temperature	O
17	48-52	5	Axle Weight 1	C
18	53-56	4	Axles 1-2 Spacing	C
19	57-61	5	Axle Weight 2	C
20	62-65	4	Axles 2-3 Spacing	C/O
21	66-70	5	Axle Weight 3	C/O
22	71-74	4	Axles 3-4 Spacing	C/O
⋮	⋮	⋮	⋮	⋮
38	143-146	4	Axles 11-12 Spacing	C/O
39	147-151	5	Axle Weight 12	C/O
40+	Additional spaces in 4-digit incr. up to 25 axles			C/O
41+	Additional weights in 5-digit incr. up to 25 axles			C/O

Note: C=Critical, C/O=Critical/Optional, O=Optional

4.4.7 Algorithm for Load Estimation

The algorithm for tire load estimation analyzes the rectified, filtered and scaled-down voltage output of the 4 PZT sensors connected in parallel. It computes the average value of the voltage output of the two peaks of the signal, as for example shown in Figure 97. This average value and the actual frequency estimated from the time interval Δt are entered into the PZT sensor model fitted (i.e., Models 1, 2 or 3 described earlier under Section 4.4.4) and the tire load estimated is doubled to compute the axle load. Axle spacing is computed from the time interval between the beginning of pulse and the next one. A 2 sec headway between successive vehicles was assumed for the purpose of separating the output from successive vehicles. This is the typical minimum time interval between successive vehicles. In addition, it allows capturing extremely long vehicles

that move slowly. For example, a triple-trailer truck with a wheel base of 24.4 m (80 ft) traveling at 43 km/hr (26 mph) takes about 2 seconds to traverse the PEH harvester. In effect, the system records voltage versus time data for a period of 2 seconds, analyzes and stores the WIM data then clears the memory. This traffic stream property allows separating vehicles without using inductive loops, which represents a significant innovation compared to conventional WIM systems. Additional algorithm details are given next.

4.4.8 Algorithm Implementation

The main steps of the entire algorithm are highlighted below (i.e., the terms in quotes indicate the variable names used in the code):

1. Read the voltage signal values and the corresponding time.
2. Store the data in two arrays, “voltage” array and “time” array. The time interval between successive voltage readings is defined by the sampling frequency of the two MCUs used

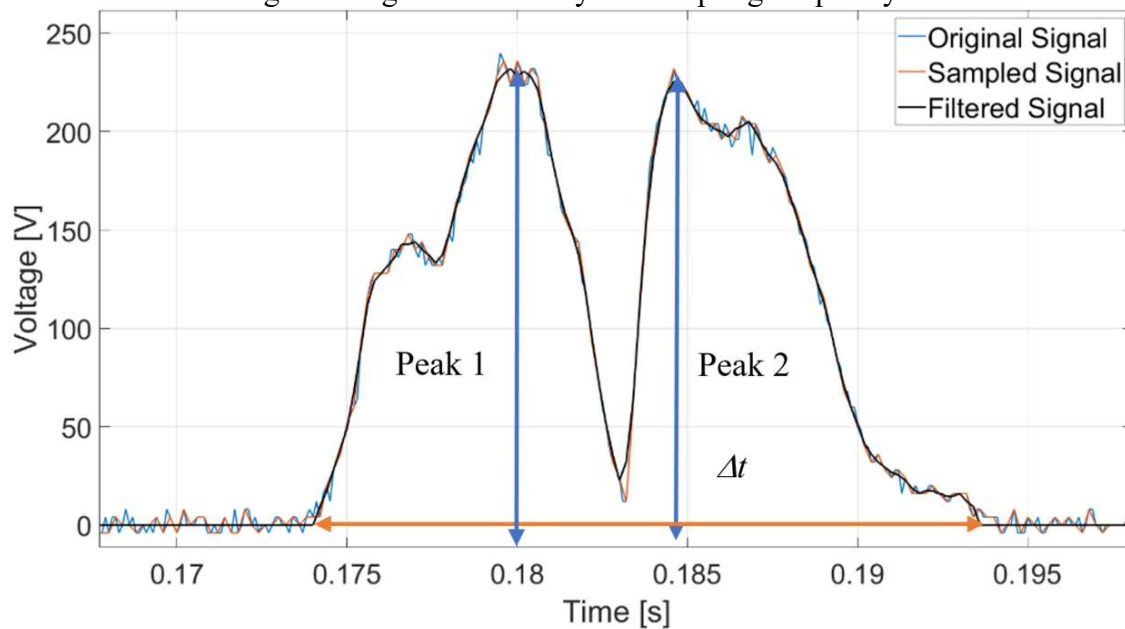


Figure 97. Example of estimating voltage amplitude; 8 kN load at a 62 Hz nominal frequency.

(i.e., either 1,200 or 2,500 Hz). Hence, the number of voltage readings corresponds to the time within the 2 sec interval allotted to each vehicle.

3. Filter the voltage array using a 3-point moving average.
4. Set to zero any voltage values lower than the noise level (i.e., 9 Volts for the oscilloscope).
5. Identify the points in time when the voltage begins to be larger than zero and store them in the “sarr” array. Then, identify the points in time when the voltage goes back to zero and store them in the “earr” array. These numbers are checked to make sure they satisfy two conditions. First, that the duration between two consecutive start and end points (i.e., pulse width) is longer than 0.004 s (i.e., this eliminates noise such as that pointed with a red circle in Figure 93). Second, check that the time elapsed between two consecutive “sarr” and “earr” pairs is shorter than 0.0034 sec (i.e., this identifies inter-pulse noise, as shown Figure 93). The finalized starting and ending points are indexed as “sarr(i)” and “earr(i)”, respectively.

6. Compute the number of axles per vehicle from the counter “i” in the “sarr(i)” array.
7. Analyze each signal and compute the corresponding number of voltage data points by computing the corresponding “earr(i)” minus sarr(i)”. Take the average of each resulted value and multiply it by the sampling interval to compute the average signal width of all vehicle axles and invert it to calculate the loading frequency. A variation of this algorithm was developed to allow for faster processing, whereby frequency was sensed using the data from the 2nd axle only.
8. Use the “sarr” and “earr” arrays for computing the highest maximum points between the first half portion of each signal and the second half of each signal. Compute the average of these two voltage peaks for each axle (Figure 97).
9. Use the loading frequency (Step 7) and the voltage amplitude computed (Step 8) as input to one of the electromechanical models fitted (i.e., either Models 1, 2 or 3) to compute the tire load and multiply it by 2 to obtain the axle load.
10. Use the frequency (Step 7) to estimate the vehicle speed and use the time difference between each consecutive ending point stored in “earr(i)” to compute the axle spacings.
11. Use the vehicle classification algorithm described in Section 4.4.6 to obtain the class of each vehicle.
12. Store the data in the standardized format described in Section 4.4.5.

Figure 98 shows a flowchart of these steps and illustrates how the classification algorithm. It was first implemented in Matlab® and then it coded in C for uploading into the MCU. A copy of the computer code is available for internal review, pending an intellectual property disclosure application submitted on March 13th 2020 (<http://research.utsa.edu/research-funding/commercialization/disclose-an-invention/>).

4.4.9 In Summary

This section described the algorithms used for estimating loading frequency, vehicle speed, axle spacing, axle load and vehicle classification. It is based on calculations of the rectified, filtered and scaled-down voltage versus time generated from each tire. The time interval Δt a tire occupies the WIM enclosure yields the loading frequency. The average of the two peaks of the processed voltage and the loading frequency are input into one of the electromechanical models developed to yield tire and axle load. The time lapsing between successive axles allows estimating the axle spacing and finally the data is stored in the standardized W-record format.

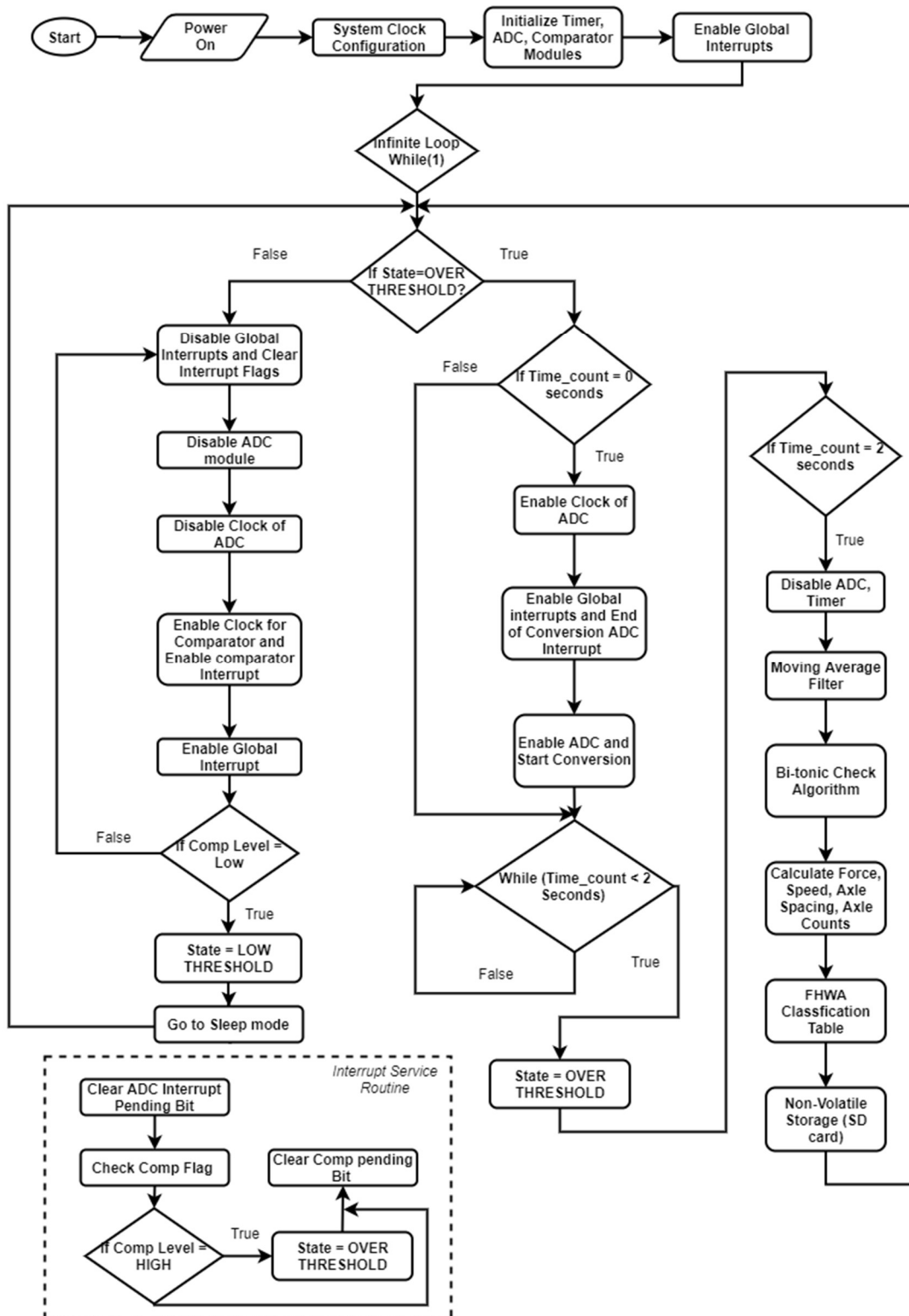


Figure 98. Flowchart logic for implementing the algorithm.

4.5 Circuitry Design

The electronic circuitry developed has three main circuitry components. First a voltage processing circuit for the 4 PZT sensing elements. Second, an energy harvesting circuit that manages the electrical power generated by the 4 PZT stacks connected in parallel. Third a MCU that serves as the DAQ for the WIM system. These components are shown schematically in Figure 99.

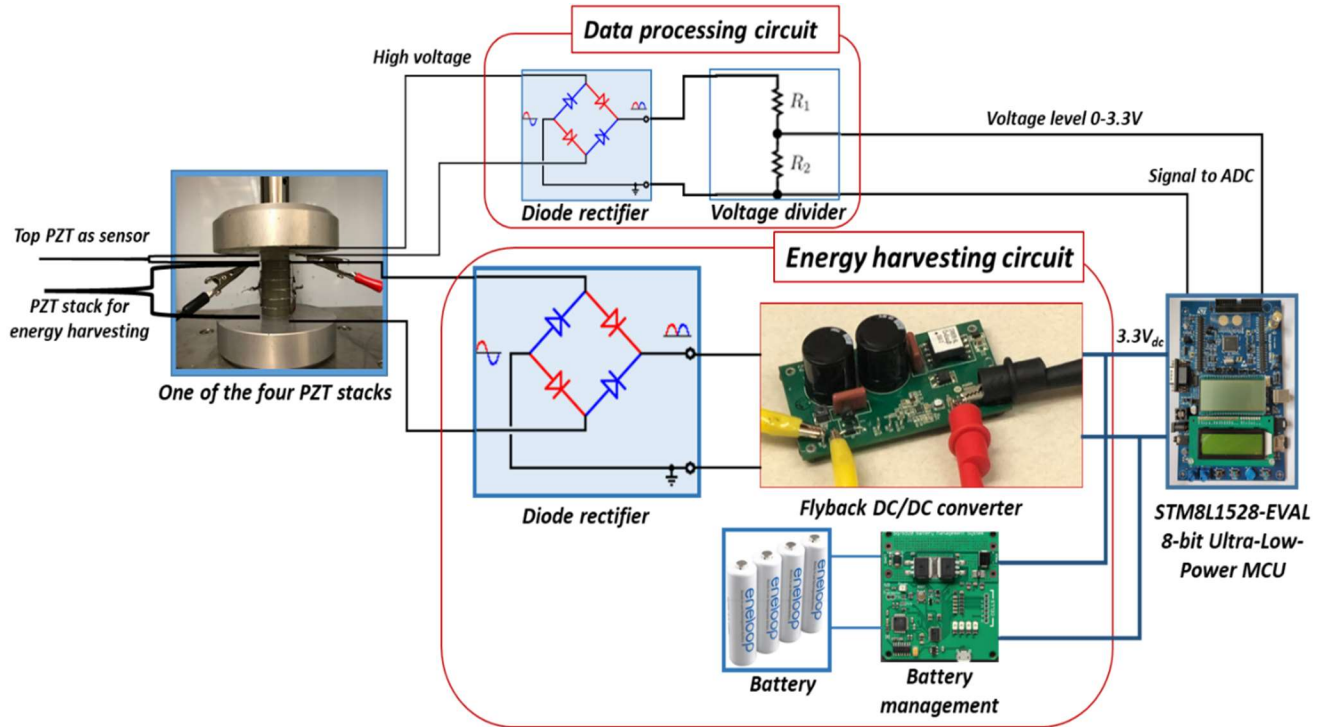


Figure 99. Block diagram of the electronic circuitry.

4.5.1 PZT Sensing Element Circuit

The main components of the circuit designed for processing the output of the 4 PZT sensing elements connected in parallel are the diode rectifier and the voltage divider (i.e., upper block of Figure 99). The rectifier reverses the sign of the negative part of loading pulses, while the voltage divider scales down the voltage output to the 0 to 3.3 Volt range suitable for input into the analog ports of the MCU.

4.5.2 Energy Harvesting Circuit

The energy harvesting circuit consists of the four PZT stacks, described in Section 4.3, connected in parallel, which in effect adds the currents produced by each of them. Their output is connected to a diode rectifier and a smoothing capacitor to convert their AC signal output to a DC signal. The DC voltage is then scaled down using an isolated flyback DC/DC converter with a customized transformer winding to match the internal impedance of the PZTs and control the output voltage to a level suitable for powering the MCU (i.e., 3.3 V). In parallel, there is a rechargeable battery system that can power the MCU when there is insufficient energy harvested from the traffic. Conversely, when there is excess energy harvested, it recharges the battery. This circuit is shown in the lower block of Figure 99.

4.5.3 The MCUs Considered

Two MCUs were considered for the DAQ system:

- An ultra-low power STM8L152M8T6 MCU with a 16 MHz, 8-bit ARM Cortex M3 core processor with a 4 kB RAM, a 64 kB flash memory, a 16 MB serial flash memory and an expandable SD card slot with 2GB memory. Its power operating range is between 1.8 and 3.6 Volts (Figure 100). This is referred to as MCU #1.
- A higher power consumption LPC54018-IoT-Module + OM4006 base board MCU with a 32-bit ARM Cortex M4 processor with 360 kB SRAM allowing a sampling frequency of up to 180 MHz, a high-speed USB device/host + PHY, a full-speed USB device/host, a 12-bit 5Msamples/s ADC, a secure Boot Feature, AES-256 encryption/decryption engine an SD Card slot. Its power operating range is between 1.71 and 3.6 Volts (Figure 101). This is referred to as MCU #2.

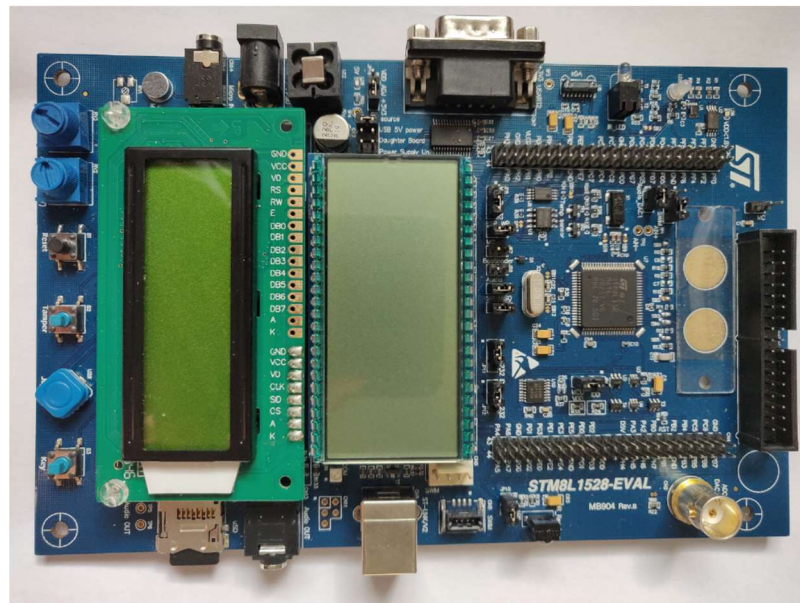


Figure 100. Original MCU Unit; STM8L152M8T6 (57).



Figure 101. Alternative MCU unit; LPC54018-IoT-Module + OM4006 base board (58).

The tradeoff between these two MCUs is their power consumption versus their ability to handle high sampling frequencies and parallel calculations. As described next, the MCU #1 is capable of a max sampling frequency of 1.2 MHz and can handle a single stream of calculations. This necessitates processing and saving the data after the 2 second interval allotted for sensing a vehicle has lapsed. Processing and saving each vehicle takes an additional 1.5 seconds (i.e., total time for processing 3.5 sec), which prevents capturing closed-spaced vehicles in the traffic stream. The MCU #2, consumes more power, but allows very high sampling frequencies and can process tire data and save them in memory simultaneously. This reduces drastically the time for processing each vehicle. These differences are explained in detail next.

4.5.3.1 The STM8L152M8T6 MCU

MCU #1 (Figure 100) has a very high memory density footprint and low power consumption. In “sleep” mode, it draws 0.9 mA, while in “awake” mode it draws 2.9 mA. Its Analog to Digital Converter (ADC) comparator is configured to “wake up” the controller from its “sleep” mode. The MCU wakes up in in 0.015 msec in response to detection of a selectable voltage change. By comparison, it takes 14 msec for a tire moving at 60 mph (88 ft/sec) to traverse the combined length of 16 inches (i.e., PEH enclosure length plus tire imprint diameter). As a result, even the steering axle of each vehicle can be captured without relying on inductive loops to “wake up” the system.

The C version of the algorithm described in Section 4.4 was uploaded into the RAM memory of this MCU. Its RAM memory limited the sampling frequency to 1.2 kHz. The algorithm was implemented to perform single track calculations. The WIM data generated is initially stored in the flash memory and then transferred to the SD memory card that has a capacity of 2 GB. Once the MCU is “awaken”, its timer is initialized. The timer is configured to read and store the digital equivalent of the analog signal in the RAM memory for a period 2.0 seconds. The 2.0 seconds interval was selected to allow separation between vehicles, as described earlier. Data processing

and storage takes place after this 2.0 second period and lasts approximately 1.5 seconds. After the data for a vehicle is recorded, the memory is cleared and the timer is reset. This points out the main limitation of this MCU. It requires approximately 3.5 seconds to process each vehicle, which is longer than the typical minimum headway between vehicles in the traffic stream. These limitations point out the need for a more capable MCU as the one described next.

4.5.3.2 The NXP OM40006 MCU

The MCU #2 has similar footprint as the one described above but has larger RAM memory and its ADC converter allows higher processing and sampling frequencies. In “sleep” mode, it draws 8.3 mA, while in “awake” mode it draws 35 mA at a processing frequency of 180 MHz. These power requirements are higher than those of MCU #1 but it allows for higher sampling frequency and parallel processing. A sampling frequency of 2.5 kHz was selected, which was half the sampling rate used in the oscilloscope evaluation. This MCU uses a multithreaded Freetos Operating System, which allows parallel processing (i.e., executing concurrent tasks). Parallel processing allows reading, processing and saving the data for each tire on the flash memory at the same time, thus reducing the time it takes to process each vehicle. To implement this, a modified version of the algorithm described in Section 4.4 was developed and uploaded into its RAM memory. Another advantage of this MCU is its wifi capability, which makes possible remote data recovery, although this stage of system development is beyond the scope of this Report.

4.5.4 In Summary

This Section described the circuitry developed for the load sensing and energy harvesting parts of the WIM system. The loading sensing circuit conditions the voltage output the 4 PZT elements, while the energy harvesting circuit maximizes the electrical energy being harvested. The harvested energy powers the MCU directly and recharges a 3.3 Volt battery. Two alternative MCUs were described and it was explained why the second was preferable. It allowed a sampling rate of 2.5 kHz which was deemed sufficient for estimating the duration of each voltage pulse and its average amplitude. Furthermore, it allowed parallel processing of reading, processing and saving the data at the same time, which effectively reduces the time it takes to process each vehicle. The results of evaluating the system developed are presented in the next Section.

5 ANALYSIS AND FINDINGS

5.1. WIM System Testing

5.1.1. Algorithm Performance

The performance of the WIM system was determined in terms of its precision and accuracy in predicting loading frequency/vehicle speed, axle load and vehicle class. Testing was initially conducted using the Matlab® code and subsequently using the MCU #1 in the laboratory. Testing the WIM system using the MCU #2 in the field will be part of the implementation of the project to take place over the next six months. The laboratory testing was conducted using the UTM machine described in Section 4.1.2. Preliminary results on the performance of the system in measuring loading frequency/vehicle speed were presented earlier (Section 4.4.2). The following sections focus on the performance of the system in measuring tire loads and determining the vehicle class, which both depend on accurate speed sensing. In interpreting the laboratory results, it is noted that the oil pump of the UTM machine was switched from its low to its high setting for generating loads higher than 6 kN.

5.1.1.1 Testing the Matlab® code in the laboratory

For this testing, the Matlab® algorithm was set to sample the voltage output of the 4 PZT sensing elements connected in parallel at two different sampling frequencies, namely 2.5 kHz and 5 kHz (i.e., the latter was the sampling frequency used for the oscilloscope testing). Load was estimated by the methodology described in Section 4.4.8. The estimated versus applied loads are shown in Figure 102 and Figure 103, respectively. It is noted that these figures list the nominal loading frequencies. The corresponding percent errors in measuring load are summarized in Table 17 and Table 18 respectively. They were computed with respect to the UTM loads applied, without performing a calibration of the output.

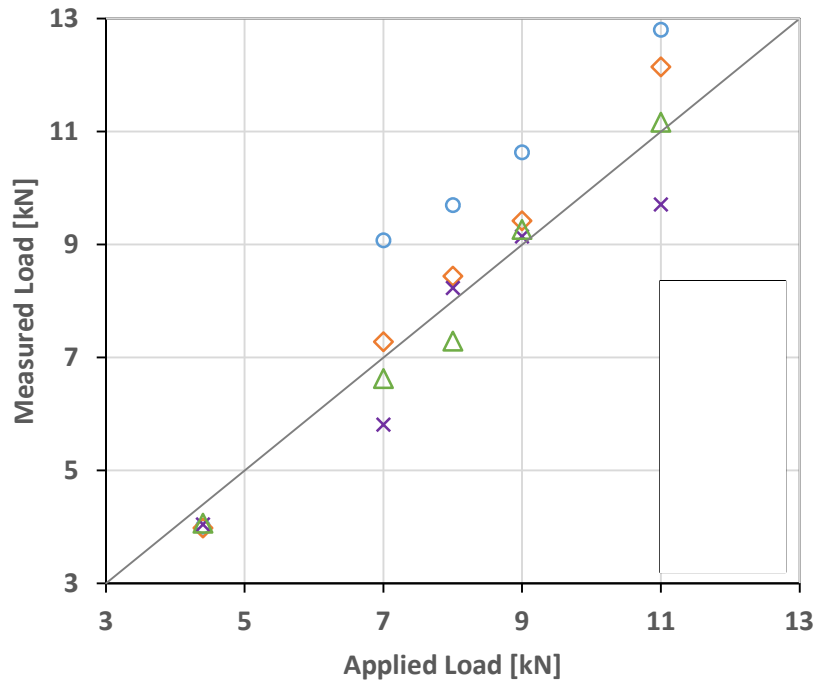


Figure 102. Matlab® algorithm measured versus applied loads; Sampling at 2.5 kHz.

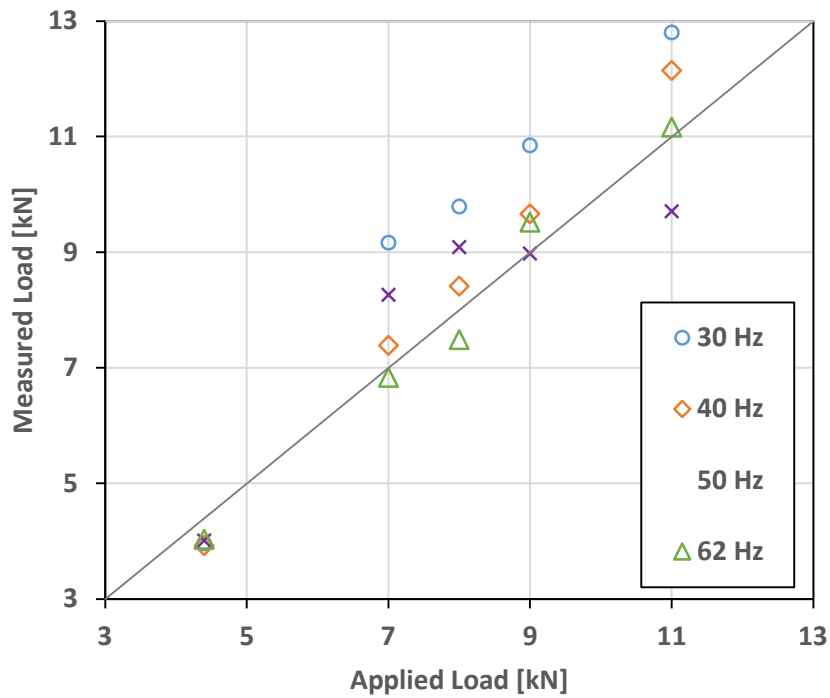


Figure 103. Matlab® algorithm measured versus applied loads; Sampling at 5 kHz.

Table 17. Load measurement error statistics of Matlab® algorithm; Sampling at 2.5 kHz.

Applied Load [kN]	4.4			
Nom. Frequency [Hz]	30	40	50	62
Mean Meas. [kN]	4.00	3.98	4.04	4.06
SD [kN]	0.11	0.15	0.13	0.09
Mean Error [%]	-9.03	-9.62	-8.13	-7.65
Error Range [%]	-9.03 to -7.65			
Applied Load [kN]	7			
Nom. Frequency [Hz]	30	40	50	62
Mean Meas. [kN]	9.07	7.27	5.81	6.62
SD [kN]	0.40	0.22	1.64	0.18
Mean Error [%]	29.61	3.90	-17.01	-5.40
Error Range [%]	-17.01 to +29.61			
Applied Load [kN]	8			
Nom. Frequency [Hz]	30	40	50	62
Mean Meas. [kN]	9.70	8.44	8.23	7.29
SD [kN]	0.19	0.49	1.86	0.09
Mean Error [%]	21.20	5.44	2.83	-8.91
Error Range [%]	-8.91 to + 21.20			
Applied Load [kN]	9			
Nom. Frequency [Hz]	30	40	50	62
Mean Meas. [kN]	10.63	9.42	9.14	9.27
SD [kN]	0.30	0.39	0.08	0.08
Mean Error [%]	18.14	4.65	1.56	2.95
Error Range [%]	+1.56 to +18.14			
Applied Load [kN]	11			
Nom. Frequency [Hz]	30	40	50	62
Mean Meas. [kN]	12.80	12.15	9.71	11.17
SD [kN]	0.31	0.83	0.09	0.26
Mean Error [%]	16.39	10.41	-11.76	1.50
Error Range [%]	+1.50 to +16.39			

These results lead to the following conclusions:

- Comparing Figure 102 and Figure 103 suggests that the differences in accuracy between these two sampling frequencies is negligible, reinforcing the decision to use a sampling frequency of 2.5 kHz in programming the MCU #2.
- There is a marked difference in the errors observed between the 4.4. kN loads and the higher loads. This was due to the switching of the UTM pump from its low to high settings, which was necessary for applying high loads at high frequencies.

Table 18. Load measurement error statistics of Matlab® algorithm; Sampling at 5 kHz.

Applied Load [kN]	4.4			
Nom. Frequency [Hz]	30	40	50	62
Mean Meas. [kN]	3.96	3.92	4.01	4.03
SD [kN]	0.14	0.18	0.09	0.12
Mean Error [%]	-10.03	-10.89	-8.85	-8.33

Applied Load [kN]	4.4			
Error Range [%]	-10.03 to -8.33			
Applied Load [kN]	7			
Nom. Frequency [Hz]	30	40	50	62
Mean Meas. [kN]	9.16	7.39	8.26	6.83
SD [kN]	0.51	0.26	0.20	0.14
Mean Error [%]	30.93	5.54	18.04	-2.39
Error Range [%]	-2.39 to +30.93			
Applied Load [kN]	8			
Nom. Frequency [Hz]	30	40	50	62
Mean Meas. [kN]	9.79	8.41	9.08	7.49
SD [kN]	0.17	0.48	0.07	0.03
Mean Error [%]	22.34	5.11	13.56	-6.41
Error Range [%]	-6.41 to +21.20			
Applied Load [kN]	9			
Nom. Frequency [Hz]	30	40	50	62
Mean Meas. [kN]	10.85	9.66	8.97	9.52
SD [kN]	0.37	0.12	0.48	0.03
Mean Error [%]	20.56	7.36	-0.29	5.74
Error Range [%]	-0.29 to +20.56			
Applied Load [kN]	11			
Nom. Frequency [Hz]	30	40	50	62
Mean Meas. [kN]	12.80	12.15	9.71	11.17
SD [kN]	0.31	0.83	0.09	0.26
Mean Error [%]	16.23	13.14	-10.38	3.50
Error Range [%]	-3.50 to +16.23			

- For a loading frequency of 30 Hz, loads higher than 7 kN were consistently overestimated. This was attributed to the tendency of the electromechanical model to overpredict loads at lower frequencies.
- Regardless, except for one of the measurements for the 7 kN load at 30 Hz, all measurements were within the $\pm 25\%$ tolerance of Type I WIM systems in measuring wheel loads (Table 1).
- Regardless of the test conditions, the standard deviation (SD) of the measurements was low (i.e., the highest value computed was 0.51 kN). This suggests that the Matlab® code precision in measuring loads is high.
- For higher loads and frequencies, which are of interest in monitoring trucks at highway speeds, mean errors were in the range between 1.5% and 5.7% suggesting acceptable accuracy of the Matlab® algorithm in measuring load.

5.1.2. Testing the MCU #1 in the laboratory

For this testing the MCU #1 was set up to read directly the voltage output of the four PZT sensors connected in parallel (Figure 104). As mentioned earlier, the limited RAM capacity of MCU #1 allowed a signal sampling frequency of only 1.2 kHz. For comparison purposes, the accuracy of MCU #1 was compared to the accuracy of the Matlab® code at a sampling frequency of 2.5 kHz.

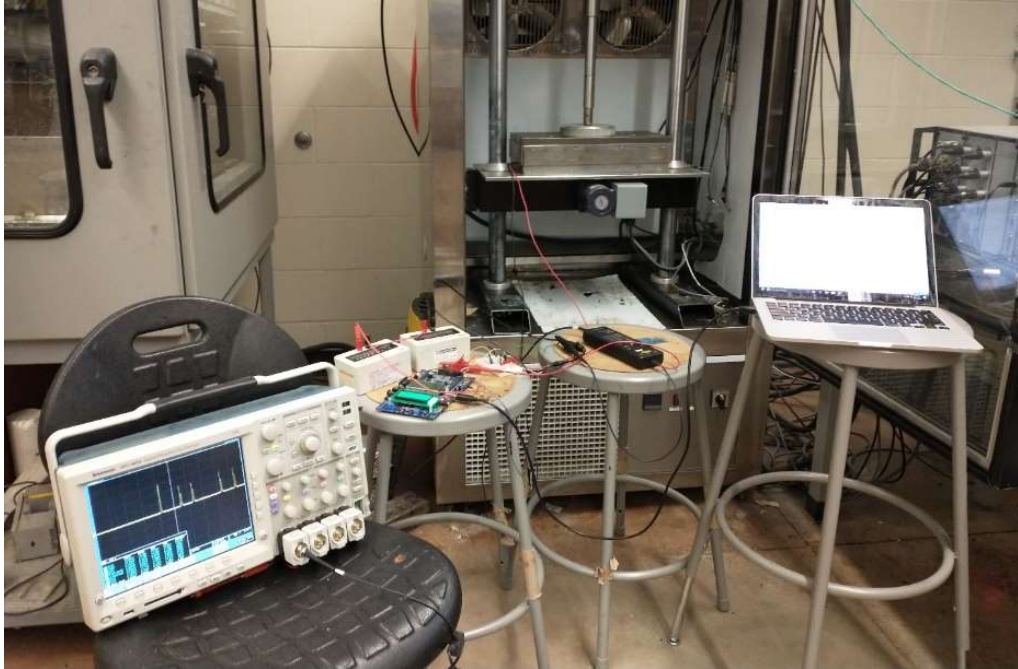


Figure 104. Experimental set up for testing the MCU #1.

Testing involved the application of sequences of load pulses through the UTM to simulate various vehicle classes, such as class 3, 5, 6 and 9 (Figure 2). The evaluation included accuracy in measuring vehicle speed, load, and identifying vehicle class. Vehicle speed accuracy was estimated with reference to manual measurements of Δt , as done earlier (Section 4.4.3). Examples of the loading sequences input are shown in Figure 105, Figure 106, Figure 107 and Figure 108 respectively. The corresponding error statistics are shown in Table 19, Table 20, Table 21, and Table 22, respectively.

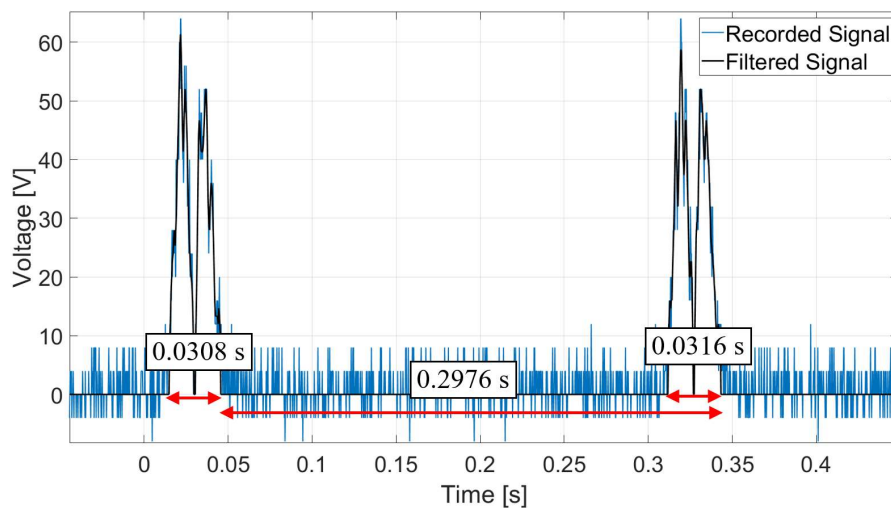


Figure 105. Simulated loading sequence for a Class 3 vehicle.

Table 19. Error statistics for the simulated Class 3 vehicle shown in Figure 105.

Data Item	Input	Matlab® @ 2.5 kHz	Matlab® % Error	MCU #1, @ 1.2 kHz	MCU #1 % Error
Frequency [Hz]	32.05	32.05	0	29.66	-7.46
Speed [ft/s]	37.43	37.43	0	34.65	-7.43
Axle Count	2	2	0	2	0
Half Axle 1 Load [kN]	4.4	3.71	-15.68	3.69	-16.14
Half Axle 2 Load [kN]	4.4	3.62	-17.73	3.91	-11.14
Axle 1 – 2 Distance [ft]	11.15	-	-	10.349	-7.184
Classification	Class 3	-	-	Class 3	-

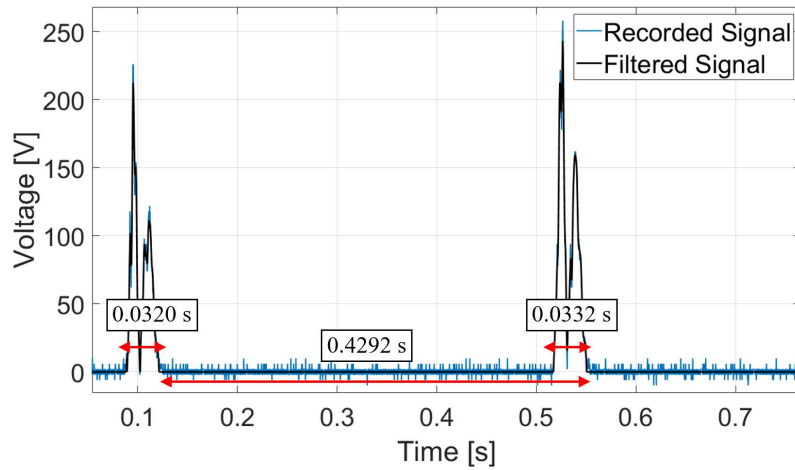


Figure 106. Simulated loading sequence for a Class 5 vehicle.

Table 20. Error statistics for the simulated Class 5 vehicle shown in Figure 106.

Data Item	Input	Matlab® @ 2.5 kHz	Matlab® % Error	MCU #1, @ 1.2 kHz	MCU #1 % Error
Frequency [Hz]	30.67	30.49	-0.59	29.66	-3.29
Speed [ft/s]	35.83	35.61	-0.61	34.65	-3.29
Axle Count	2	2	0	2	0
Half Axle 1 Load [kN]	8	10.85	35.63	14.6	82.50
Half Axle 2 Load [kN]	10	13.44	34.40	13.94	39.40
Axle 1 – 2 Distance [ft]	15.39	-	-	14.88	-3.31
Classification	Class 5	-	-	Class 5	-

These results suggest the following:

- The 2.5 kHz sampling frequency yields much higher accuracy in predicting loads than the 1.2 kHz sampling frequency. This confirms the decision to use a 2.5 kHz sampling frequency in programming the MCU #2.
- For loads higher than the 4.4 kN, all the prediction errors except one (i.e., that for the 12 kN steering axle load of the class 9 vehicle), were positive (i.e., loads were over-predicted). Assuming that the loads applied by the UTM are correct, load measuring accuracy can be improved by calibration. However, as mentioned earlier, it should be kept in mind that there are limits to the ability of the UTM to accurately apply high loads at high frequencies (Section 4.1.2).
- Even without calibration, the load measurement errors for all vehicles, except those of the slow class 5 vehicle (Figure 106), were within the $\pm 25\%$ range of ASTM E1318 (Table 1). The low accuracy in estimating the loads from the class 5 vehicle is likely due to the tendency of the electromechanical model to overpredict load at low loading frequencies.

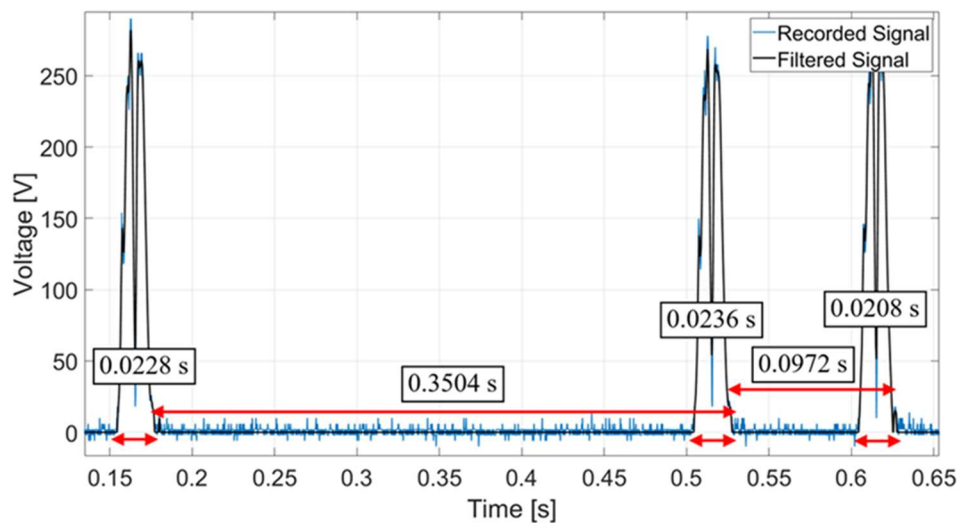


Figure 107. Simulated loading sequence for a Class 6 vehicle.

Table 21. Error statistics for the simulated Class 6 vehicle shown in Figure 107.

Data Item	Input	Matlab® @ 2.5 kHz	Matlab® % Error	MCU #1, @ 1.2 kHz	MCU #1 % Error
Frequency [Hz]	44.64	44.64	0	41.15	-7.82
Speed [ft/s]	52.13	52.14	0.02	48.06	-7.81
Axle Count	3	3	0	3	0
Half Axle 1 Load [kN]	10	11.46	14.60	13.94	39.40
Half Axle 2 Load [kN]	10	11.13	11.30	13.16	31.60
Half Axle 3 Load [kN]	10	11.52	15.20	13.47	34.70
Axle 1 – 2 Distance [ft]	18.27	-	-	16.88	-7.61

Axle 2 –3 Distance [ft]	5.05	-	-	4.82	-4.55
Classification	Class 6	-	-	Class 6	-

- Finally, even at the lower sampling frequency used for MCU #1, the vehicle speed was estimated with an error lower than about 7%, while the vehicle class was always predicted correctly. At the higher sampling frequency, vehicle speed was detected with an error lower than 1.42%, which at highway speeds (e.g., 120 km/h) is roughly in the ± 1.6 km tolerance range specified by ASTM E1318 (Table 1).

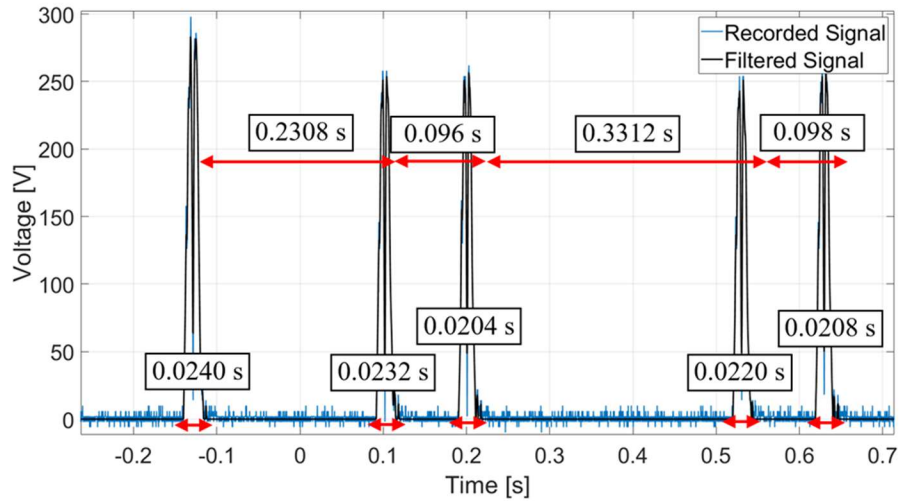


Figure 108. Simulated loading sequence for a Class 9 vehicle.

Table 22. Error statistics for the simulated Class 9 vehicle shown in Figure 108.

Data Item	Input	Matlab® @ 2.5 kHz	Matlab® % Error	MCU #1, @ 1.2 kHz	MCU #1 % Error
Frequency [Hz]	45.29	44.64	-1.44	43.98	-2.89
Speed [ft/s]	52.89	52.14	-1.42	51.38	-2.85
Axle Count	5	5	0	5	0
Half Axle 1 Load [kN]	12	11.93	-0.58	13.06	8.83
Half Axle 2 Load [kN]	9	10.7	18.89	11.74	30.44
Half Axle 3 Load [kN]	9	10.74	19.33	11.6	28.89
Half Axle 4 Load [kN]	9	10.47	16.33	11.3	25.56
Half Axle 5 Load [kN]	9	10.86	20.67	11.74	30.44
Axle 1 – 2 Distance [ft]	12.21	-	-	11.84	-3.03
Axle 2 – 3 Distance [ft]	5.08	-	-	4.95	-2.56
Axle 3 – 4 Distance [ft]	17.52	-	-	17.12	-2.28

Axle 4 – 5 Distance [ft]	5.18	-	-	4.91	-5.21
Classification	Class 9	-	-	Class 9	

5.2. PEH Power Generation

This part of the WIM system evaluation dealt with the power harvesting performance of the PEH (i.e., the 4 PZT stacks connected in parallel). It involved two parts, namely simulating the electrical power output of the PEH using Matlab/Simulink®, and actual laboratory testing of the power harvested by subjecting the PEH to UTM loading.

5.2.1. PEH Matlab/Simulink® simulation

The electromechanical model of the PZT stack described in Section 4.2 was implemented into an electric circuit model using Matlab/Simulink® (Figure 109). This allowed predicting its output over the wide range of conditions anticipated under in-service roadway traffic. These include variable loading frequencies (i.e., vehicle speeds) and traffic axle loads. Extensive testing of this simulated circuit was undertaken to validate the accuracy of its output. An example is shown in Figure 110 that plots the estimated and measured voltage output as a function of time for open circuit and for a 650 kΩ external impedance under a sinusoidal load of 4 kN at a 62 Hz frequency. This model produced a very good quality of fit. This electro-mechanical model for the PZT stack is to be used in designing the circuitry of the PEH that powers the microprocessor. The electromechanical model was then subjected to a pulse load input of 6 kN at a 62 Hz frequency to simulate the passage of a light truck tire moving at approximately 60 mph. This single PZT stack harvester produced 400 V_{rms}, 0.9 mA and a power of 0.38 W as shown in Figure 111. These results were validated by the experimental testing of the PZT stack.

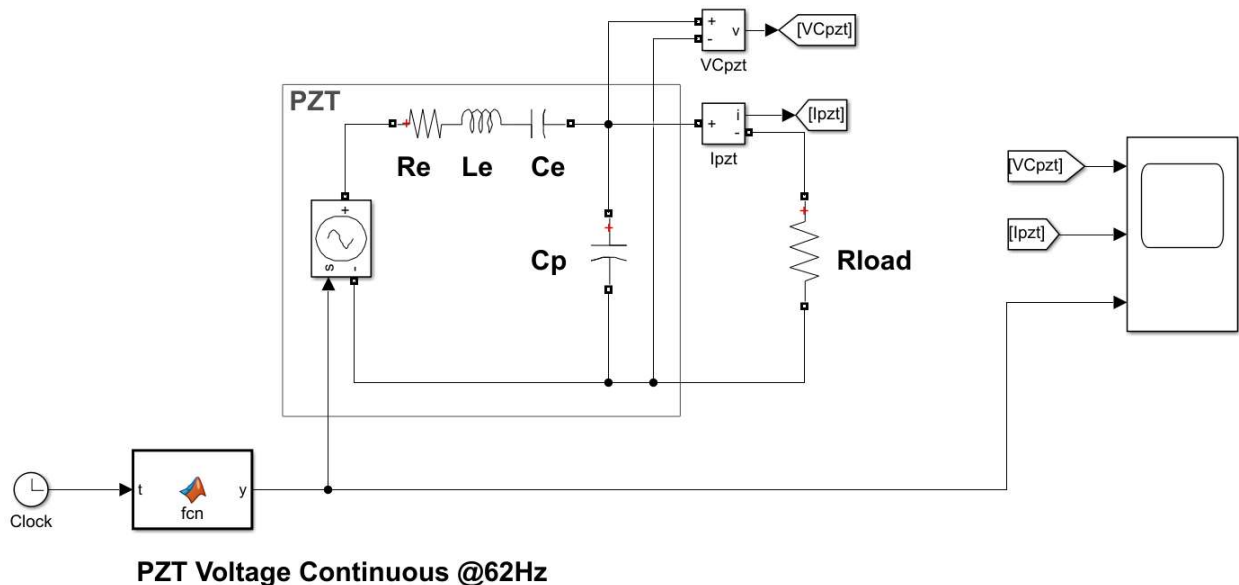


Figure 109. Equivalent PZT circuit in Matlab/Simulink®.

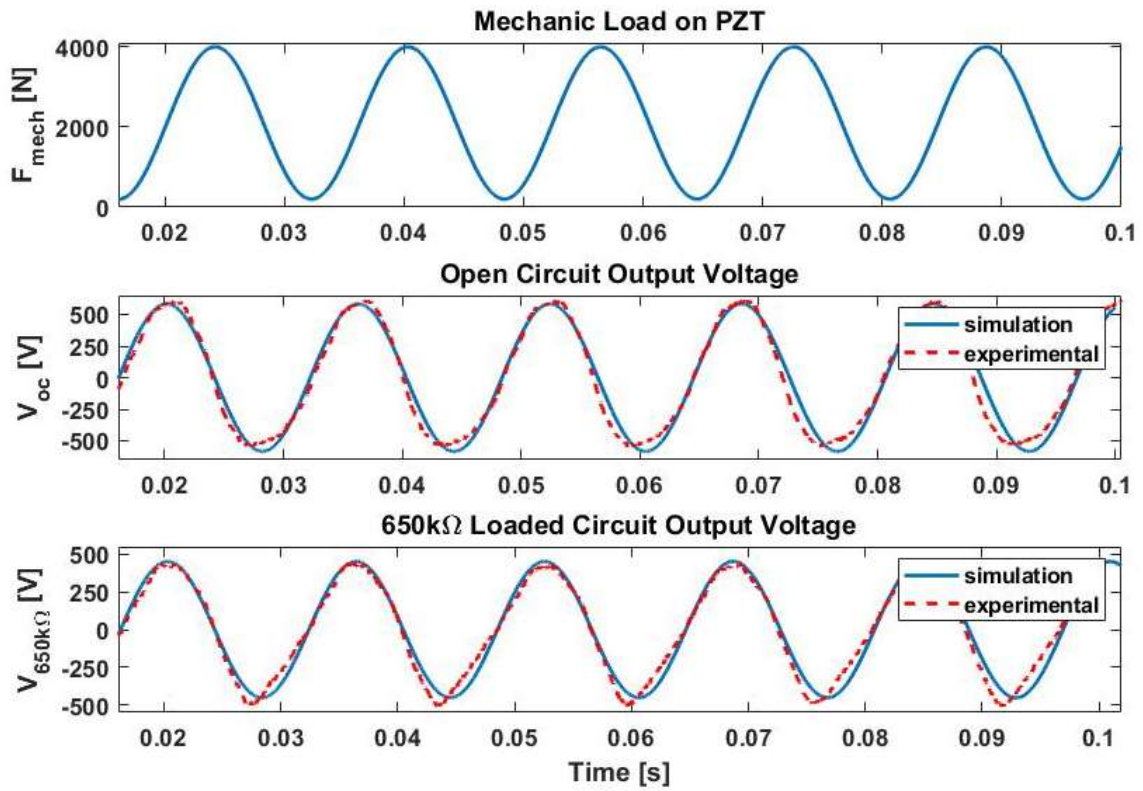


Figure 110. Example of Matlab/Simulink® model validation results.

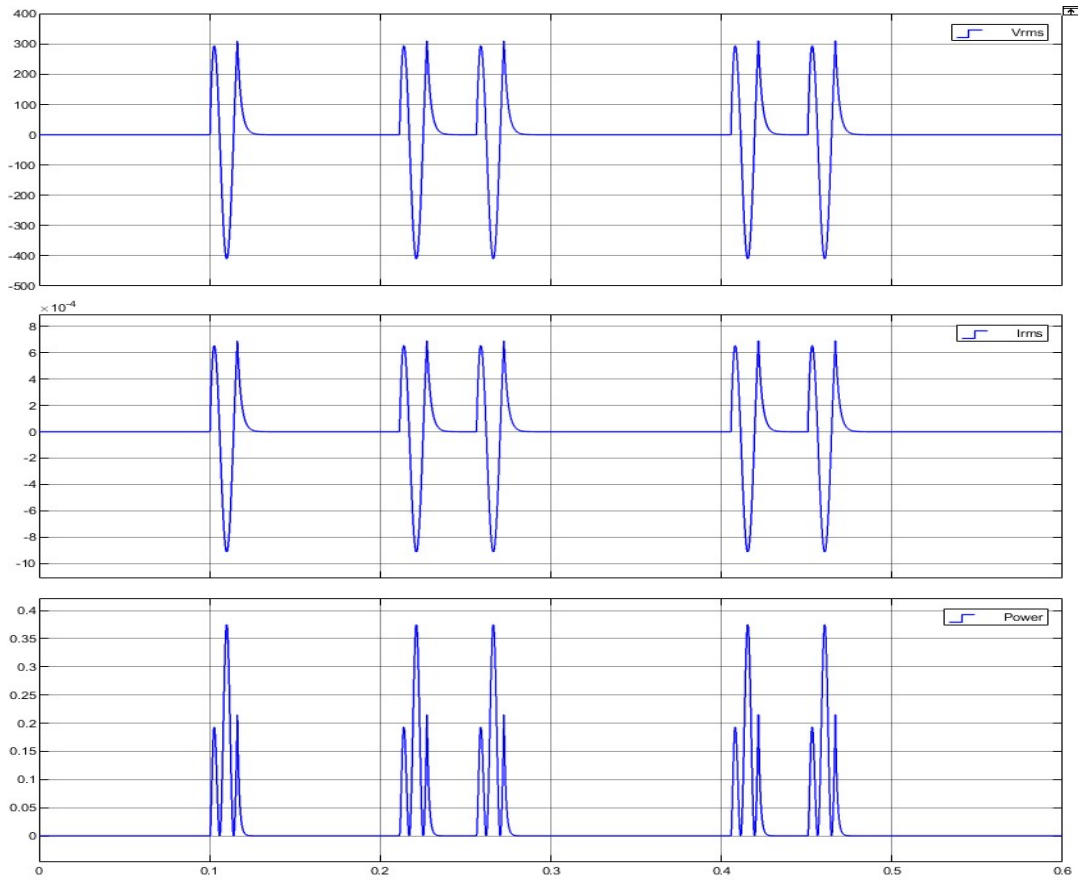


Figure 11. Simulation results of one PZT stack with resistive load at 62 Hz and 6 kN (a) voltage, (b) current and (c) power versus time.

The second step in the design was to add a diode rectifier at the output of the PZT stacks to convert the AC output voltage into a rectified DC voltage. The hardware testing in the lab showed that for one PZT stack connected to a diode rectifier and then to a resistive load under a load of 6 kN at 62 Hz gave nearly the same output as earlier (i.e., 0.9 mA, 400V_{rms}, and 0.38 W). These results show that adding a diode rectifier does not affect the output. Figure 112 shows the electrical circuit model used in the simulation and the output matching the values obtained in the lab. The peak values for the simulation show the voltage peak to be around 400 V_{rms}, the output current around 0.9 mA, and output power peak around 0.38 W. These values were obtained using a 450 kΩ resistive load.

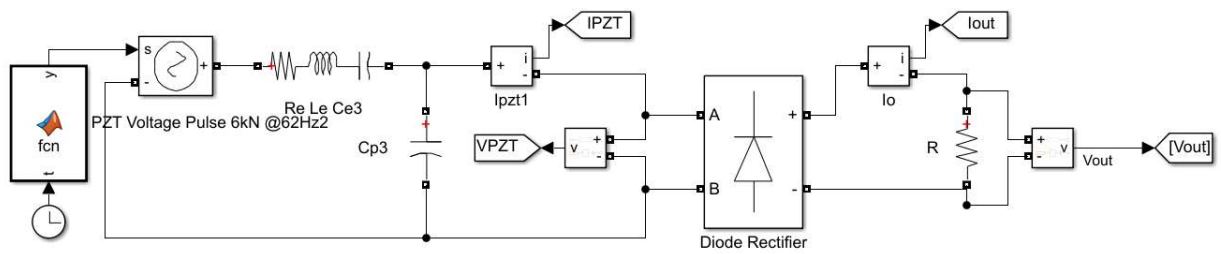


Figure 112. Simulation circuit schematic for a PZT stack feeding the diode rectifier, and resistive load.

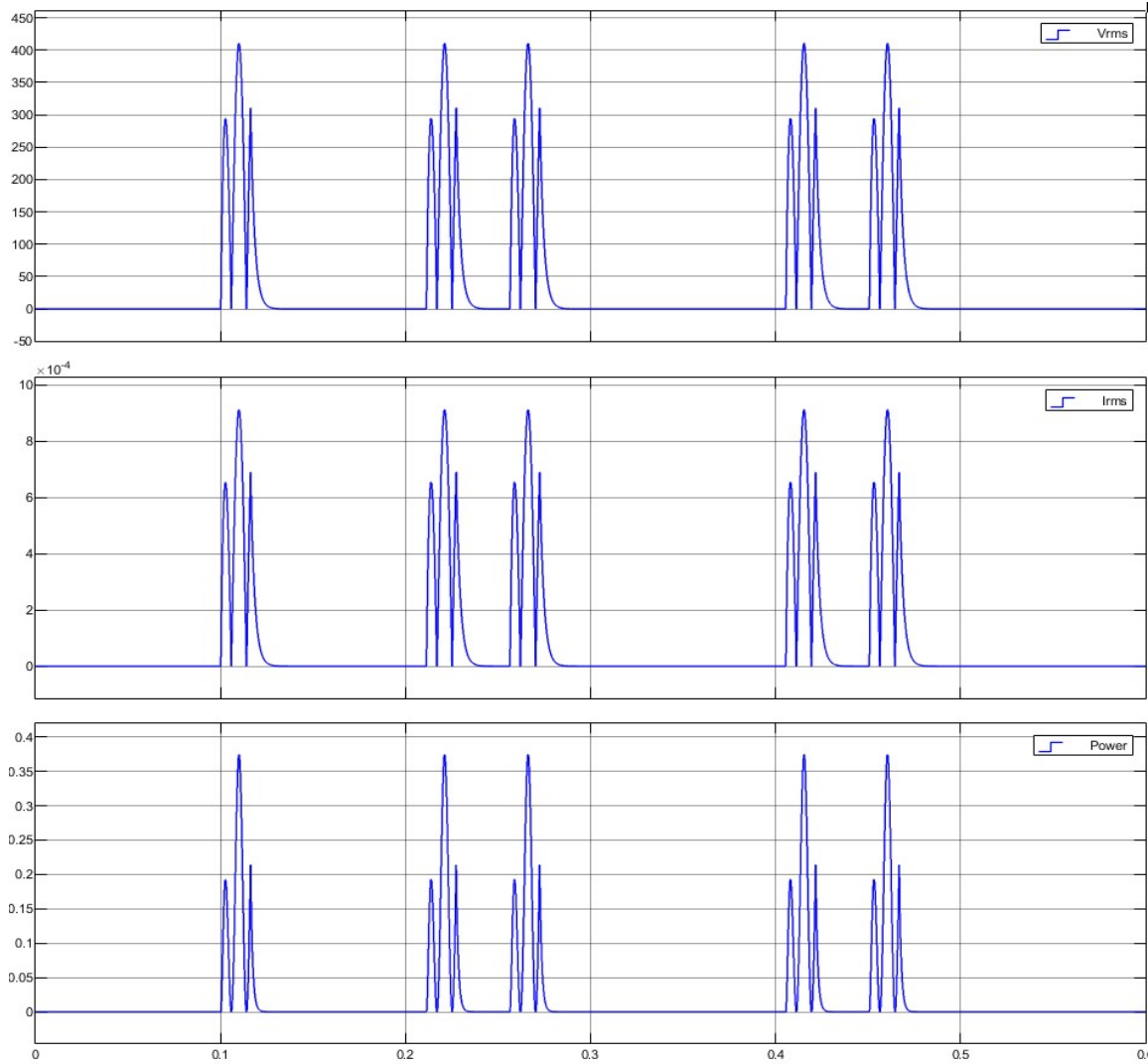
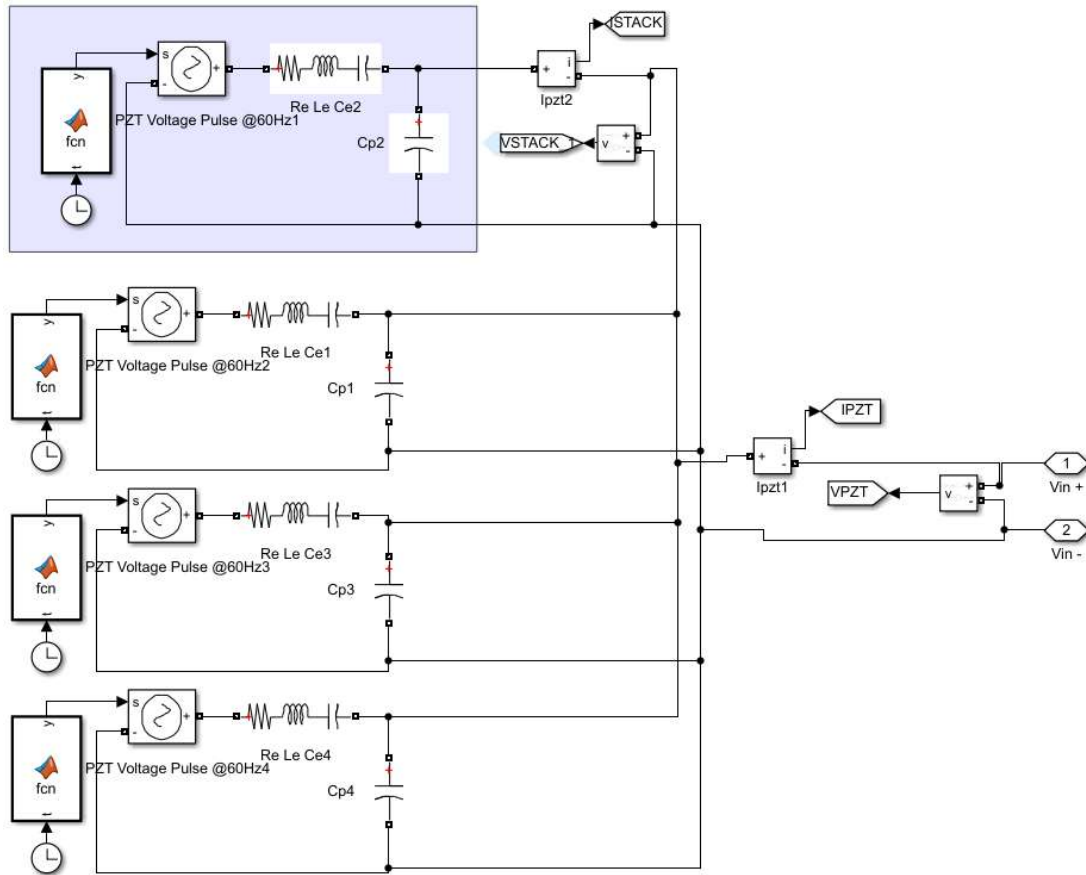
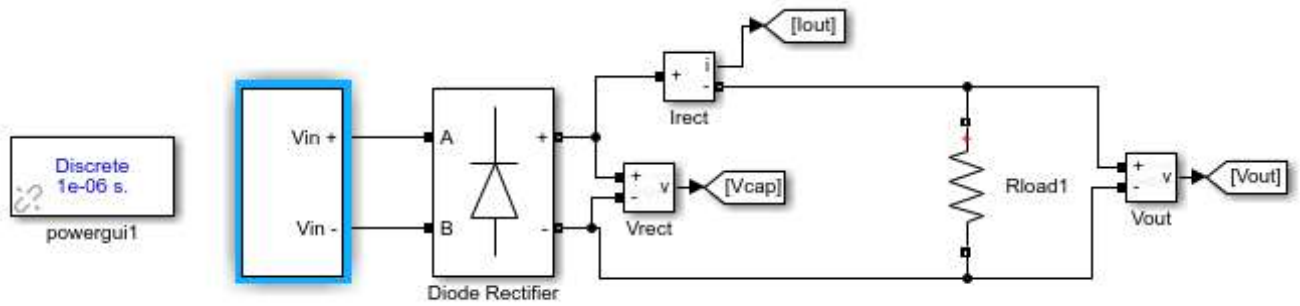


Figure 113. Simulation results of one PZT stack with diode rectifier and resistive load at 62 Hz and 6 kN (a) voltage, (b) current and (c) power versus time.

For simulating the 4 PZT stacks connected in parallel, it was assumed that the impedance of the 4 PZT stacks connected in parallel equaled the theoretical $1/4^{\text{th}}$ of the impedance of a single PZT stack. This was shown earlier to be the case for loading frequencies approximately higher than 10 Hz (Figure 55). This also suggests that the power output of the 4 PZT stacks should be roughly 4 times as large as that of a single PZT stack. Accordingly, it was found that the internal impedance of four stacks was 112.5 k Ω . The 4 PZT stacks connected in parallel were attached to a diode rectifier with a resistive load of 112.5 k Ω as shown in Figure 114. The peak output voltage of this configuration was about 400 V_{rms}, the corresponding peak output current was approximately 3.6 mA, and the resulting output power was 1.52 W (Figure 115).



(a)



(b)

Figure 114. (a) Model of four stacks of PZT, (b) four PZT stacks connected to a diode rectifier and an equivalent resistive load.

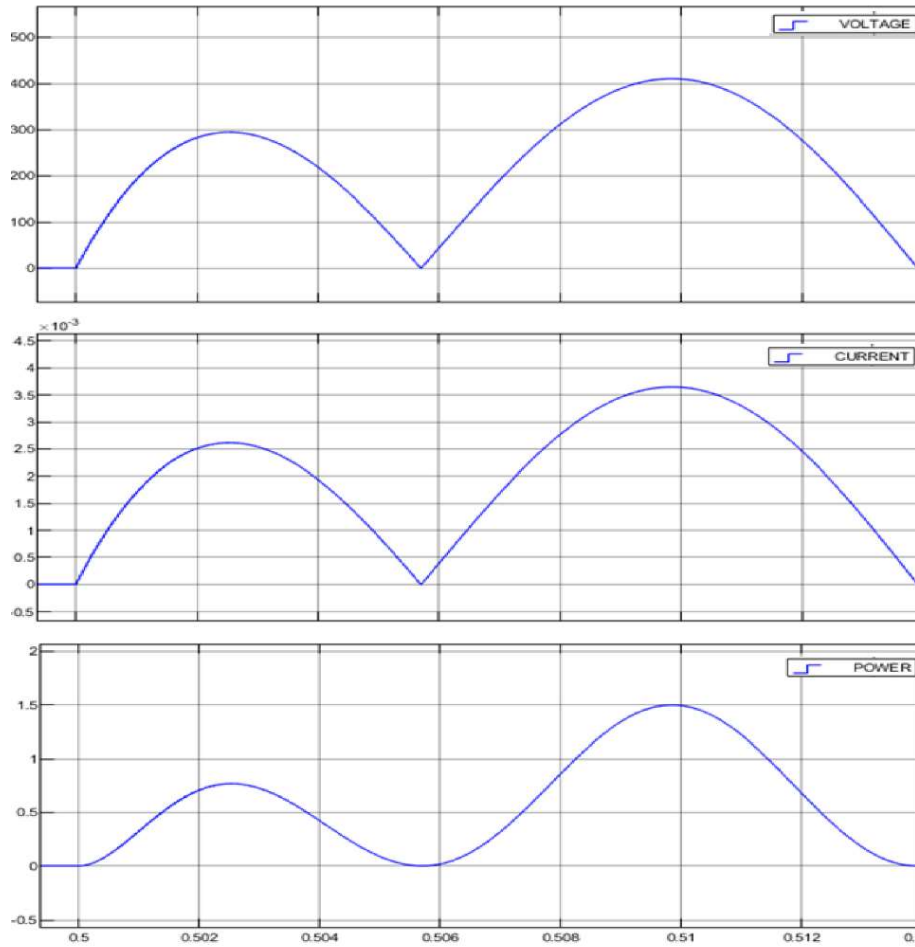


Figure 115. Simulation results of four PZT stacks with diode rectifier and equivalent resistive load at 62 Hz and 6 kN (a) voltage, (b) current and (c) power versus time.

The modified electromechanical model of the 4 PZT stacks connected in parallel described in Section 4.2.3 was also simulated using Matlab/Simulink®. Figure 116 plots the measured output voltage, current and power as a function of time with a 130 kΩ external impedance under a sinusoidal load of 6 kN at a 62 Hz frequency.

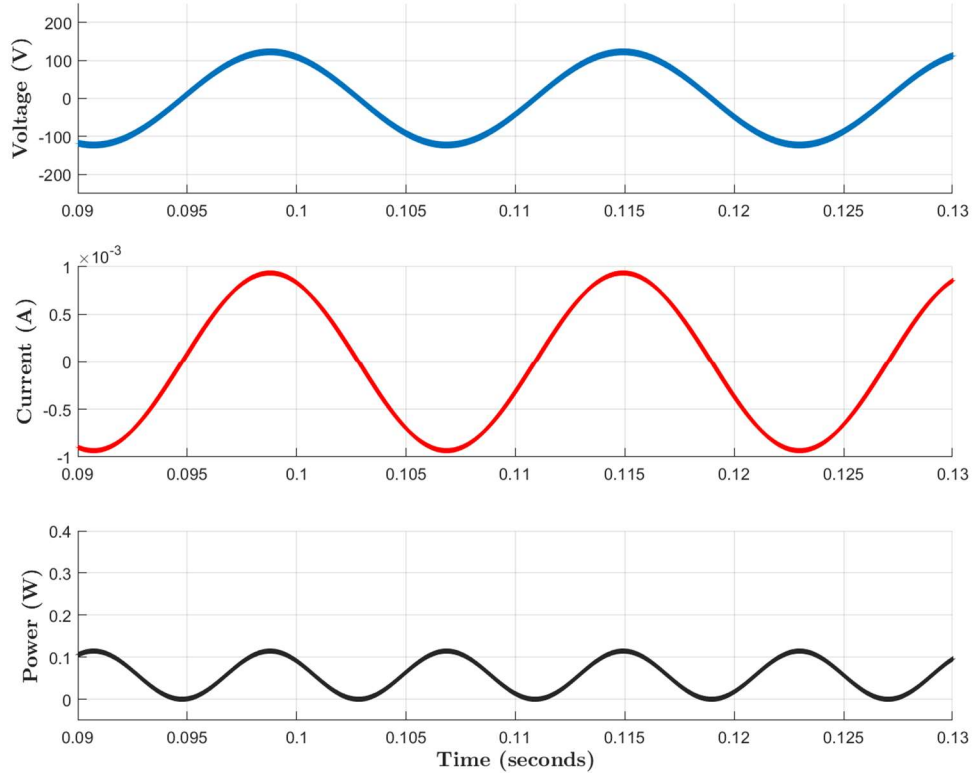


Figure 116. Simulation results of one PZT stack with diode rectifier and resistive load at 62 Hz and 6 kN (a) voltage, (b) current and (c) power versus time.

The next step in the design was to add a flyback converter after the diode rectifier to step down the voltage to the acceptable input range of the MCUs. The flyback was added to the output of the rectifier replacing the resistive load as shown in Figure 117. For the flyback converter design, the optimal switching frequency f_s was chosen to be 200 kHz and the optimal duty ratio d was found to be 20%. Using these values the rest of the flyback converter was designed using the following set of formulas:

$$N = \frac{V_{RECT}}{V_{OUT} V_{DIODE}} \frac{d}{(1 - d)} \quad [44]$$

Where, N is the number of turns of the transformer, V_{RECT} is the rectifier output voltage, V_{OUT} is the desired output voltage, V_{DIODE} is the voltage drop on the diode and d is the duty ratio. The primary inductance of the transformer L_p was used to match the internal impedance of the PZT and is calculated using Equation [44] as follows:

$$L_p = \frac{R_{INTERNAL} d^2}{2 f_s} \text{ and } R_{LOAD} = \frac{R_{INTERNAL}}{N^2} \quad [45]$$

Where, $R_{INTERNAL}$ is the internal impedance of the PZT stacks. The secondary inductance of the flyback transformer and the mutual inductance are then directly calculated using:

$$L_S = \frac{R_{LOAD}}{2 \pi f_S} \quad (46)$$

$$M = \sqrt{L_P L_S}$$

Using the equations above, the values used in the simulation were established. The primary, secondary, and mutual inductance values were 11.3 mH, 115 μ H, and 1.1 mH, respectively. The corresponding output resistive load value needed was at least 145 Ω . A smoothing capacitor was added before the resistive load in order to smoothen the output ripples. Figure 118 and Figure 119 depict the simulation results at the output of the diode rectifier and the flyback DC/DC converter, respectively. The output values obtained from this simulation were a peak output voltage 3.6 V_{rms}, a peak output current 25 mA_{rms}, and a peak output power 90 mW (Figure 119). However, to obtain this output, the resistive load needed is at least 145 Ω .

The simulation was then tested with 4 PZT stacks under a pulse signal representing a load of 11 kN at 62 Hz (i.e., the load applied by a light truck tire at highway speeds). Under this scenario, the flyback converter parameters were recalculated and resulted in primary, secondary, and mutual inductances of 11.3 mH, 32.8 μ H, and 607 μ H, respectively. The output voltage of the rectifier was 4.95 V, with peak output current 0.12 A_{rms}, and corresponding peak output power of 0.6 W (Figure 120). However, to obtain this output, the resistive load needed is at least 42 Ω .

In conclusion, simulations suggest that the PEH can generate sufficient power from traffic to sustain a roadside MCU. However, the converter transformer needs to be designed to match the input impedance of the PZTs, as well be able to provide sufficient output voltage. It was also concluded that the PEH power output from light vehicles (i.e., Classes 1 to 3) is too low to contribute significantly in powering the MCU. Light vehicles will be weighed and classified but will contribute little to powering the WIM system. On the other hand, heavy vehicles (i.e., Classes 4 to 13) generate sufficient output to power the WIM system.

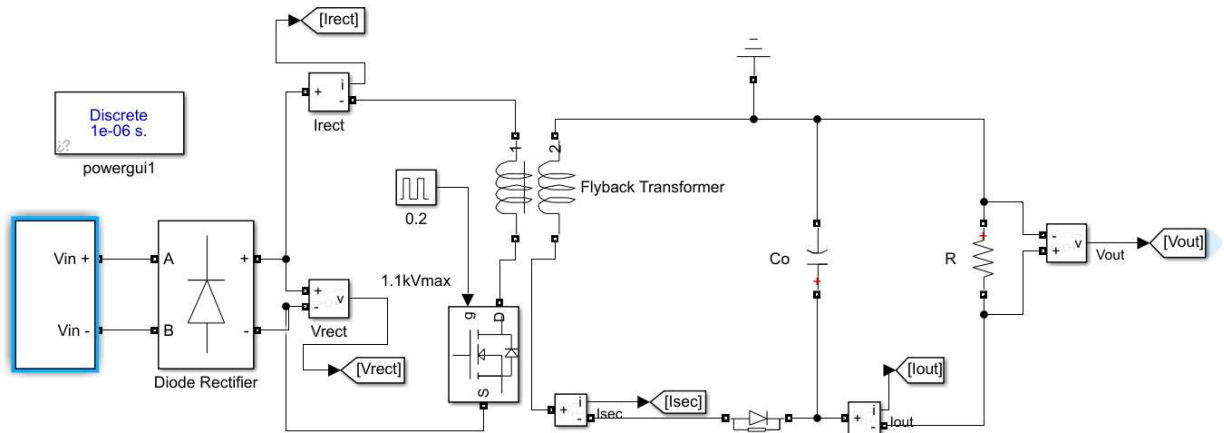


Figure 117. Simulation circuit schematic with four PZT stacks, diode rectifier, flyback DC/DC converter and a resistive load.

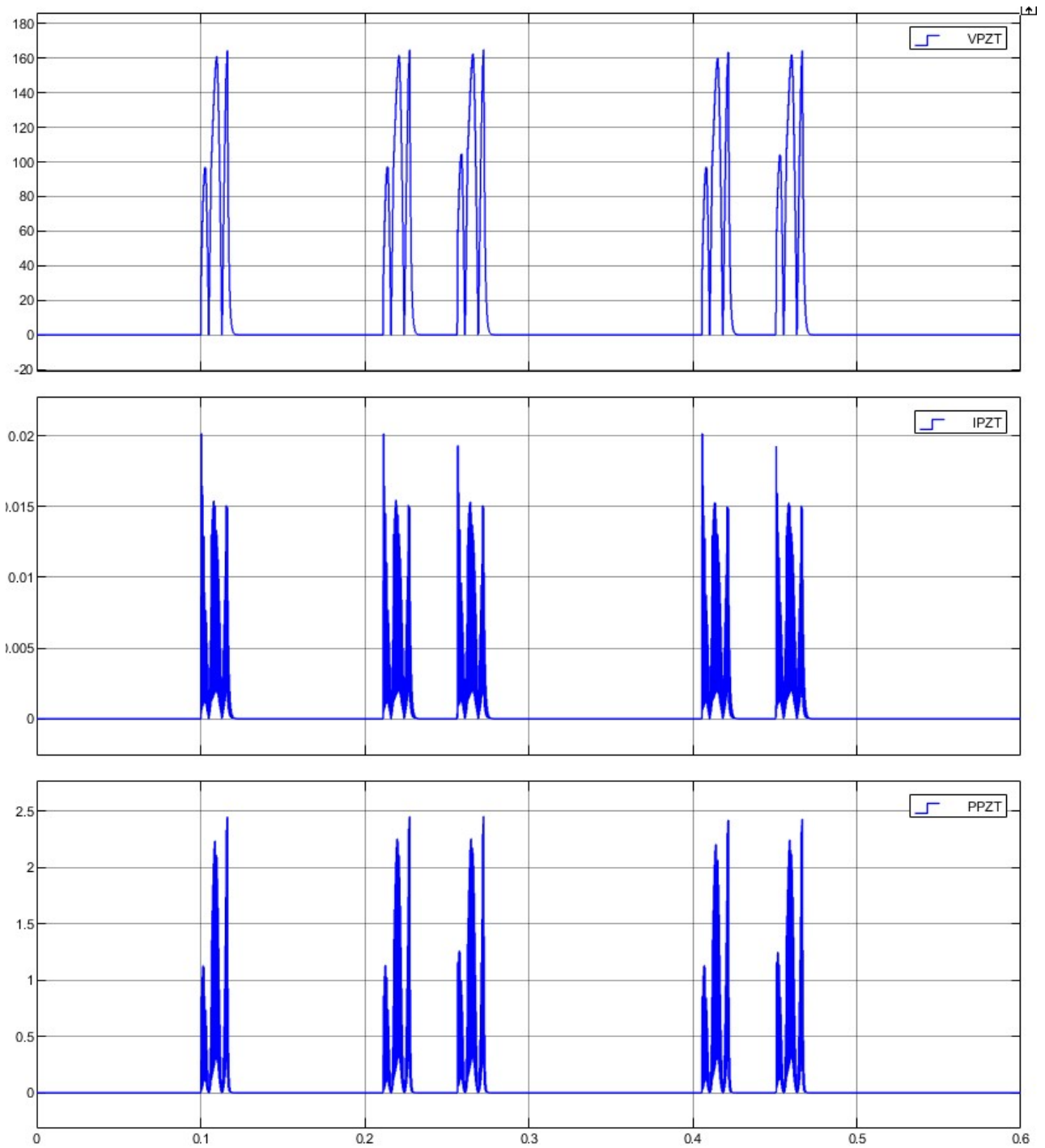


Figure 118. Simulation results at the output of the diode rectifier for four PZT stacks with diode rectifier, flyback DC/DC converter and resistive load of 145Ω at 62 Hz and 6 kN (a) voltage, (b) current and (c) power versus time.

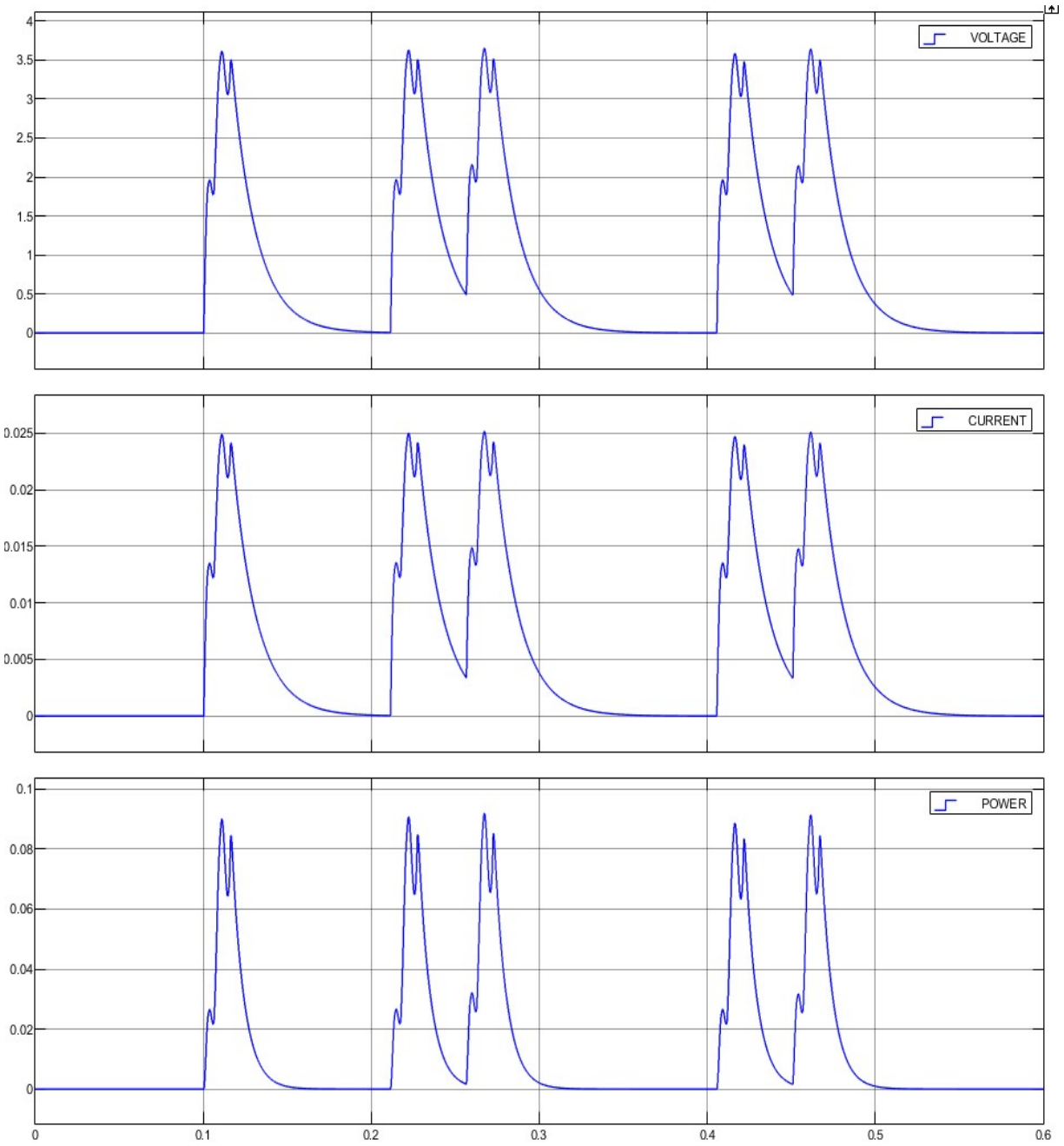


Figure 119. Simulation results at the flyback output of four PZT stacks with diode rectifier, flyback DC/DC converter and resistive load of 145 Ω at 62 Hz and 6 kN (a) voltage, (b) current and (c) power versus time.

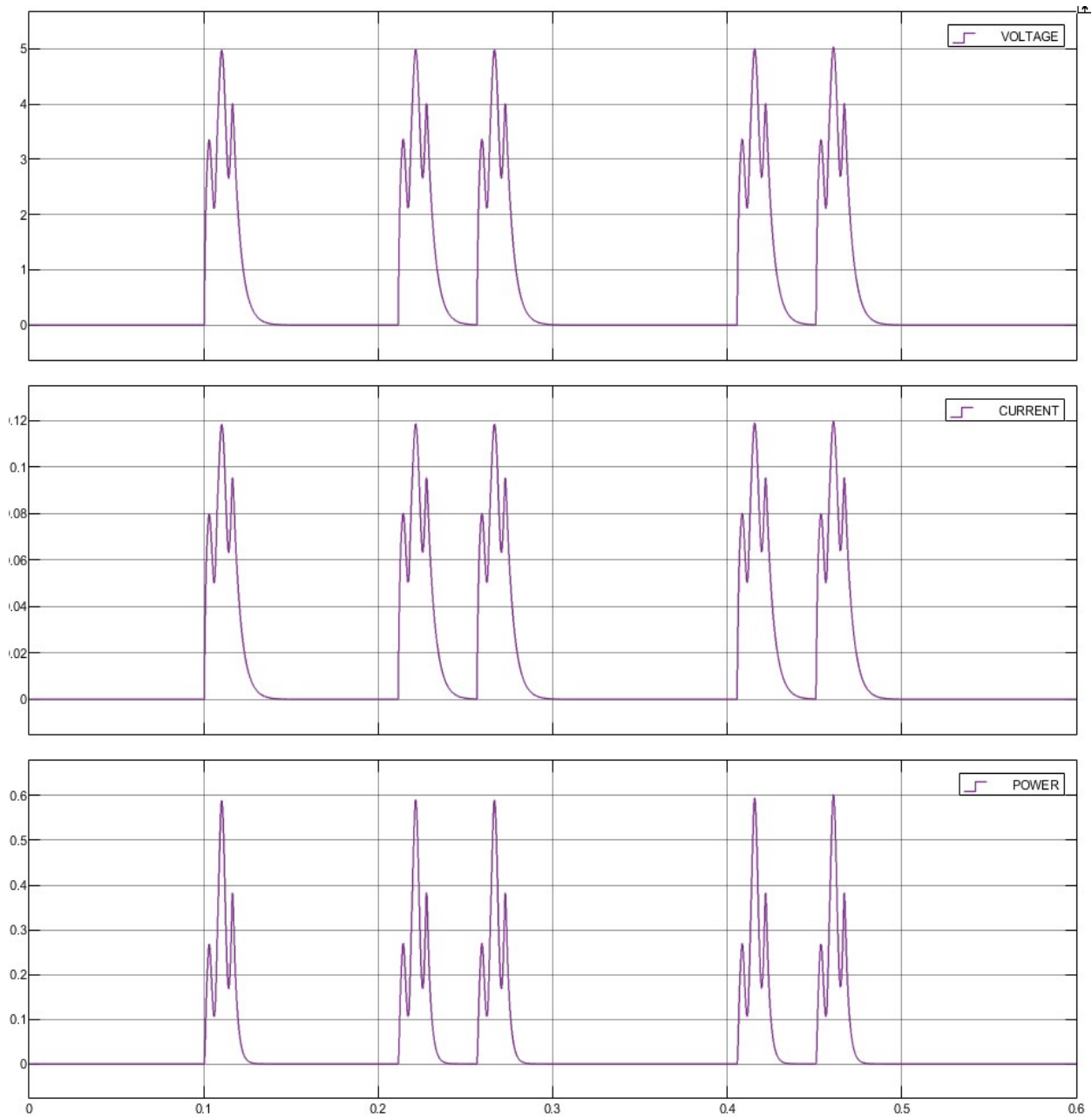


Figure 120. Simulation results at the flyback output of four PZT stacks with diode rectifier, flyback DC/DC converter and resistive load of 42Ω at 62 Hz and 11 kN (a) voltage, (b) current and (c) power versus time.

5.2.2. PEH laboratory testing

Figure 121 shows the laboratory setup for testing the energy harvesting circuit. The setup consists of four PZT stacks connected to a diode rectifier feeding a flyback DC/DC converter, an adjustable external resistance and a set of LEDs lights. The flyback DC/DC converter chosen was a commercial converter by Maximum Integrated (MAX 17497A) with input voltage of $85\text{-}265 \text{ V}_{\text{ac}}$, output voltage of 3.3 V , and maximum output current of 600 mA running at 250 kHz .

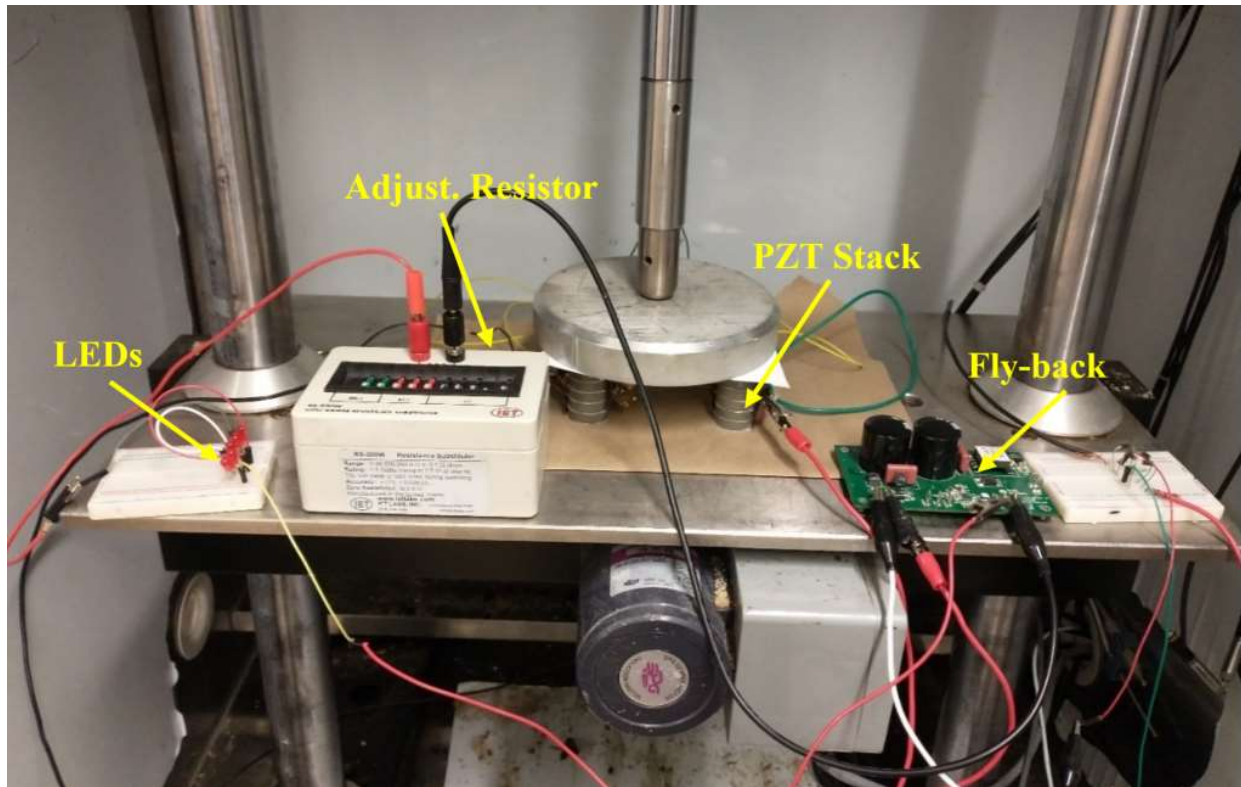


Figure 121. Experimental setup of the four piezo-stacks with diode rectifier, flyback DC/DC converter, resistive load and LEDs.

Figure 122 depicts an example of the experimental testing result of the four PZT stacks under a continuous sinusoidal loading of 11 kN at a frequency of 62 Hz. The results show that the output of the flyback is regulated to a constant 3.3 V. It also shows the energy harvested from the PEH is capable of powering multiple LEDs, which provides evidence that the power generated is sufficient for operating an ultra-low power MCU.

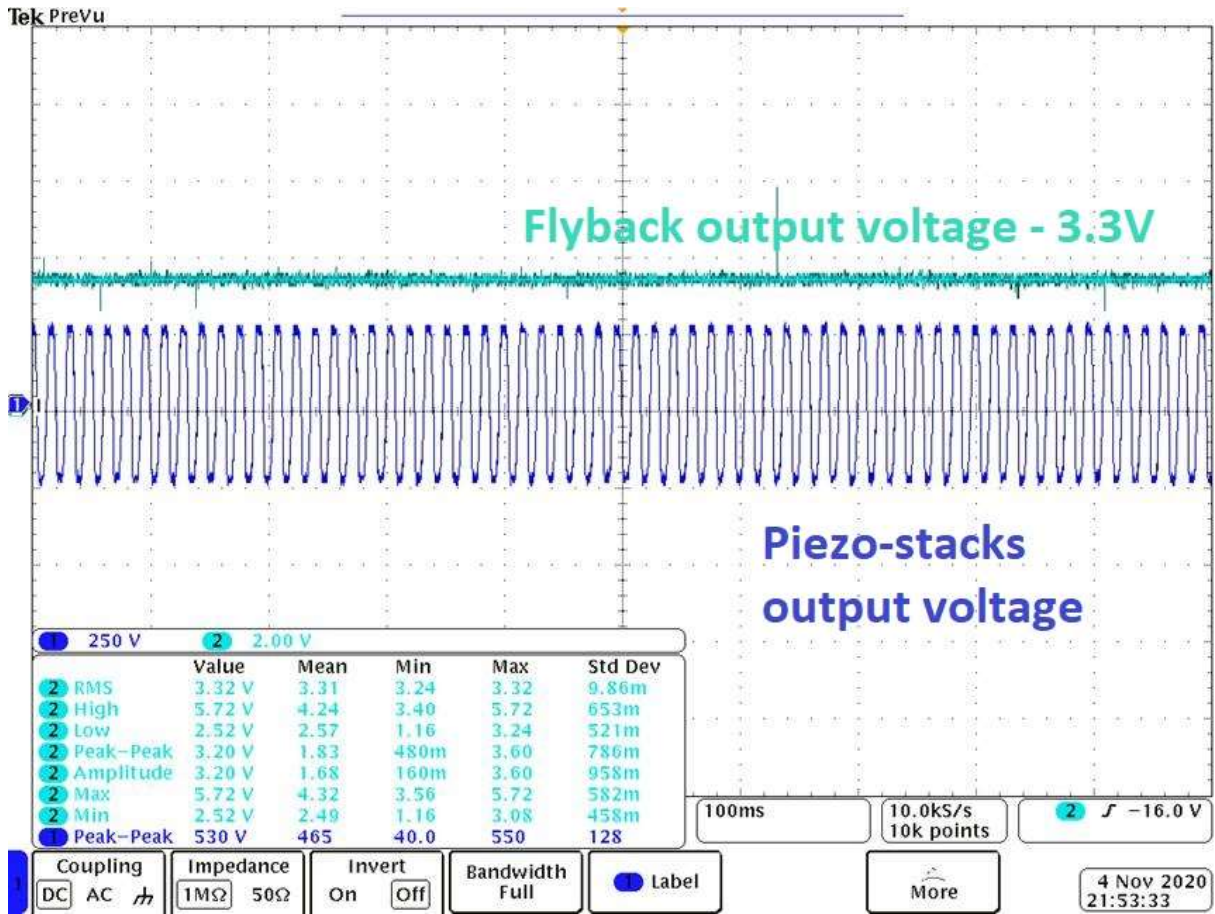


Figure 122. Experimental result – output voltage of the four piezo-stacks with diode rectifier, flyback DC/DC converter, resistive load and LEDs.

6 CONCLUSIONS

This Report described the development of a novel weigh-in-motion (WIM) system that utilizes piezoelectric (PZT) elements for sensing load and powering itself. Sensing is done by four cylindrical PZT elements 1-inch in diameter connected in parallel. Energy harvesting is done by a set of four PZT stacks, each consisting of 6 1-inch diameter elements arranged in alternating polarity and connected in parallel (i.e., this increases the amperage and decreases the voltage output). The WIM box enclosure has a simple “shoe-box” design, with each corner of its upper plate supported by one of the PZT stacks/sensor combinations. The box was sized to capture loads on one wheel path (i.e., 28-inch wide by 8 inch long).

A servo-hydraulic Universal Testing Machine (UTM) was used to apply loads at various frequencies. An oscilloscope was used for collecting the voltage output data. Preliminary testing showed that, given a loading frequency, the relationship between sensing voltage output and stress is linear, provided that the upper plate of the WIM box is sufficiently stiff. Electromechanical models were fitted to describe the relationship between voltage output, load and loading frequency/vehicle speed. The model for the four PZT sensing elements was used to translate voltage output to load for sensing purposes, while the model for the four PZT stacks connected in parallel was used for simulating the energy harvesting potential of the system.

Software was developed implementing the electromechanical model fitted for sensing. It outputs vehicle speed, axle load, number of axles and their spacing as well as vehicle classification according to the FHWA 13 vehicle scheme. The data is output for each individual vehicle using the W-record format specified in the 2016 Traffic Monitoring Guide. The software was first implemented in Matlab® and then converted to C language prior to loading onto the memory of an ultra-low power microcontroller unit (MCU).

Two MCUs were considered, with varying data handling capabilities and power consumption requirements. These MCUs have very short “wake-up” times allowing vehicle sensing without the need for inductive loops commonly used by commercially available WIM systems. The advantage of the faster MCU was that it allowed a higher sampling frequency of 2.5 kHz and could handle parallel processing, which shortens the time need to process each vehicle. The typical headway of 2 seconds was allotted to separate vehicles. Within this time interval, the time interval of loading pulses allows computing the loading frequency/vehicle speed and the time interval between pulses allows computing the axle spacing. The amplitude of pulses and the loading frequency is input into the electromechanical model of the sensing elements to predict load.

Special electric circuits were developed for conditioning/sensing the voltage output and for maximizing the power output. Simulations of the latter indicate that under heavy truck traffic the harvester should generate sufficient power for maintain operation of the MCU and recharging a backup battery. The system was tested in the laboratory by applying loading sequences simulating various vehicle classes moving at various speeds. The results suggest that vehicle speed and classification predictions were accurate, axle load predictions were precise and in general within the tolerance limits prescribed by the ASTM standard E1318. Additional work is need to implement the faster MCU which will shorten the time need to process a vehicle and test the WIM system in and field.

REFERENCES

1. Skokandić D, Žnidarič A, Mandić-Ivanković A, Kreslin M. Application of Bridge Weigh-in-Motion measurements in assessment of existing road bridges. 2017;8.
2. Mallela J, Titus-Glover L, Sadasivam S, Bhattacharya B, Darter M, Von Quintus H. Implementation of the AASHTO Mechanistic-Empirical Pavement Design Guide for Colorado [Internet]. Denver, CO: Colorado Department of Transportation; 2013 Jul [cited 2020 Nov 9]. Report No.: CDOT-2013-4. Available from: <https://trid.trb.org/view/1256466>
3. ASTM E1318-09(2017) - Standard Specification for Highway Weigh-In-Motion (WIM) Systems with User Requirements and Test Methods [Internet]. ASTM International, West Conshohocken, PA; 2017 [cited 2020 Mar 30]. Available from: www.astm.org
4. Kwon TM. Development of a Weigh-Pad-Based Portable Weigh-In-Motion System. 2012;
5. Dineva PS, Gross D, Müller R, Rangelov T. Dynamic Fracture of Piezoelectric Materials: Solution of Time-Harmonic Problems via BIEM [Internet]. Springer International Publishing; 2014 [cited 2018 Feb 12]. (Solid Mechanics and Its Applications). Available from: [//www.springer.com/us/book/9783319039602](http://www.springer.com/us/book/9783319039602)
6. Hu J, Tao J. Energy Harvesting from Pavement via PVDF: Hybrid Piezo-Pyroelectric Effects. 2016 Aug 11;556–66.
7. Cho I, Lee J-H, Park J, Yi D-H, Cho D ?Dan?, Kim S-W. A New Method for Accurately Estimating the Weight of Moving Vehicles Using Piezoelectric Sensors and Adaptive-footprint Tire Model. *Veh Syst Dyn*. 2003 Feb 1;39(2):135–48.
8. Jiang XZ, Li YC, Wang J, Li JC. Electromechanical modeling and experimental analysis of a compression-based piezoelectric vibration energy harvester. *Int J Smart Nano Mater*. 2014 Jul 3;5(3):152–68.
9. Xiong H, Wang L. Piezoelectric energy harvester for public roadway: On-site installation and evaluation. *Appl Energy*. 2016 Jul 15;174:101–7.
10. Lajnef N, Chatti K, Chakrabartty S, Rhimi M, Sarkar P. Smart pavement monitoring system. United States. Federal Highway Administration; 2013.
11. Alavi AH, Hasni H, Lajnef N, Chatti K. Continuous health monitoring of pavement systems using smart sensing technology. *Constr Build Mater*. 2016 Jul;114:719–36.
12. Andriopoulou S. A review on energy harvesting from roads. [Internet]. 2012 [cited 2020 Oct 4]. Available from: <http://urn.kb.se/resolve?urn=urn:nbn:se:kth:diva-101819>
13. Guan MJ, Liao WH. Characteristics of Energy Storage Devices in Piezoelectric Energy Harvesting Systems. *J Intell Mater Syst Struct*. 2008 Jun 1;19(6):671–80.
14. Guo L, Lu Q. Potentials of piezoelectric and thermoelectric technologies for harvesting energy from pavements. *Renew Sustain Energy Rev*. 2017 May;72:761–73.

15. Sodano HA, Inman DJ, Park G. Comparison of Piezoelectric Energy Harvesting Devices for Recharging Batteries. *J Intell Mater Syst Struct*. 2005 Oct;16(10):799–807.
16. Xiong H. Piezoelectric Energy Harvesting for Roadways [PhD Thesis]. Virginia Tech; 2015.
17. Roshani H, Jagtap P, Dessouky S, Montoya A, Papagiannakis AT. Theoretical and Experimental Evaluation of Two Roadway Piezoelectric-Based Energy Harvesting Prototypes. *J Mater Civ Eng*. 2018 Feb 1;30(2):04017264.
18. Papagiannakis A. T., Montoya A., Dessouky S., Helffrich J. Development and Evaluation of Piezoelectric Prototypes for Roadway Energy Harvesting. *J Energy Eng*. 2017 Oct 1;143(5):04017034.
19. Kour R, Charif A. Piezoelectric Roads: Energy Harvesting Method Using Piezoelectric Technology. *Innov Energy Res*. 2016 Mar 25;5(1):1–6.
20. Erturk A, Inman DJ. Piezoelectric Energy Harvesting. John Wiley & Sons; 2011. 467 p.
21. Platt SR, Farritor S, Haider H. On Low-Frequency Electric Power Generation With PZT Ceramics. *IEEEASME Trans Mechatron*. 2005 Apr;10(2):240–52.
22. Hassan HF, Hassan SIS, Rahim RA. Acoustic Energy Harvesting Using Piezoelectric Generator for Low Frequency Sound Waves Energy Conversion. *Int J Eng Technol*. 2014;5(6):7.
23. Suggs CW, Abrams CF. Mechanical impedance techniques for evaluating the dynamic characteristics of biological materials. *J Agric Eng Res*. 1971 Sep;16(3):307–15.
24. Feenstra J, Granstrom J, Sodano H. Energy harvesting through a backpack employing a mechanically amplified piezoelectric stack. *Mech Syst Signal Process*. 2008 Apr;22(3):721–34.
25. Batra AK, Alomari A. Power Harvesting via Smart Materials [Internet]. SPIE PRESS; 2017 [cited 2018 Jul 12]. Available from: <http://ebooks.spiedigitallibrary.org/book.aspx?doi=10.1117/3.2268643>
26. Ottman GK, Hofmann HF, Bhatt AC, Lesieutre GA. Adaptive piezoelectric energy harvesting circuit for wireless remote power supply. *IEEE Trans Power Electron*. 2002 Sep;17(5):669–76.
27. Calìò R, Rongala U, Camboni D, Milazzo M, Stefanini C, de Petris G, et al. Piezoelectric Energy Harvesting Solutions. *Sensors*. 2014 Mar 10;14(3):4755–90.
28. Xu T-B, Siochi EJ, Kang JH, Zuo L, Zhou W, Tang X, et al. Energy harvesting using a PZT ceramic multilayer stack. *Smart Mater Struct*. 2013 Jun 1;22(6):065015.

29. Wischke M, Masur M, Kröner M, Woias P. Vibration harvesting in traffic tunnels to power wireless sensor nodes. *Smart Mater Struct*. 2011 Jul;20(8):085014.
30. Yao L, Zhao HD, Dong ZY, Sun YF, Gao YF. Laboratory Testing of Piezoelectric Bridge Transducers for Asphalt Pavement Energy Harvesting [Internet]. Vol. 492, *Key Engineering Materials*. Trans Tech Publications Ltd; 2012 [cited 2020 Oct 4]. p. 172–5. Available from: <https://www.scientific.net/KEM.492.172>
31. Kim C-I, Kim K-B, Jeong Y-H, Lee Y-J, Cho J-H, Paik J-H, et al. Development and Evaluation of the Road Energy Harvester According to Piezoelectric Cantilever Structure and Vehicle Load Transfer Mechanism. *J Korean Inst Electr Electron Mater Eng*. 2012;25(10):773–8.
32. Cafiso S, Cuomo M, Di Graziano A, Vecchio C. Experimental Analysis for Piezoelectric Transducers Applications into Roads Pavements [Internet]. Vol. 684, *Advanced Materials Research*. Trans Tech Publications Ltd; 2013 [cited 2020 Oct 4]. p. 253–7. Available from: <https://www.scientific.net/AMR.684.253>
33. Zhao S, Erturk A. Energy harvesting from harmonic and noise excitation of multilayer piezoelectric stacks: modeling and experiment. In: *Active and Passive Smart Structures and Integrated Systems 2013* [Internet]. International Society for Optics and Photonics; 2013 [cited 2020 Oct 4]. p. 86881Q. Available from: <https://www.spiedigitallibrary.org/conference-proceedings-of-spie/8688/86881Q/Energy-harvesting-from-harmonic-and-noise-excitation-of-multilayer-piezoelectric/10.1117/12.2009823.short>
34. Li C. Road Performance of Common Piezoelectric Transducer for Asphalt Pavement Energy Harvesting [Internet]. Vols. 744–746, *Applied Mechanics and Materials*. Trans Tech Publications Ltd; 2015 [cited 2020 Oct 12]. p. 1491–4. Available from: <https://www.scientific.net/AMM.744-746.1491>
35. Song Y, Yang CH, Hong SK, Hwang SJ, Kim JH, Choi JY, et al. Road energy harvester designed as a macro-power source using the piezoelectric effect. *Int J Hydrog Energy*. 2016 Aug 3;41(29):12563–8.
36. Kim J, Lee TH, Song Y, Sung TH. Robust design optimization of fixed-fixed beam piezoelectric energy harvester considering manufacturing uncertainties. *Sens Actuators Phys*. 2017 Jun 15;260:236–46.
37. Xiao J, Zou X, Xu W. ePave: A Self-Powered Wireless Sensor for Smart and Autonomous Pavement. *Sensors*. 2017 Oct;17(10):2207.
38. Yang H, Wang L, Hou Y, Guo M, Ye Z, Tong X, et al. Development in Stacked-Array-Type Piezoelectric Energy Harvester in Asphalt Pavement. *J Mater Civ Eng*. 2017 Nov;29(11):04017224.
39. Hou Y, Wang L, Wang D, Yang H, Guo M, Ye Z, et al. A Preliminary Study on the IoT-Based Pavement Monitoring Platform Based on the Piezoelectric-Cantilever-Beam

- Powered Sensor [Internet]. Vol. 2017, *Advances in Materials Science and Engineering*. Hindawi; 2017 [cited 2020 Oct 12]. p. e4576026. Available from: <https://www.hindawi.com/journals/amse/2017/4576026/>
40. Guo L, Lu Q. Modeling a new energy harvesting pavement system with experimental verification. *Appl Energy*. 2017 Dec;208:1071–82.
 41. Jasim A, Wang H, Yesner G, Safari A, Maher A. Optimized design of layered bridge transducer for piezoelectric energy harvesting from roadway. *Energy*. 2017 Dec 15;141:1133–45.
 42. Wang C, Wang S, Li QJ, Wang X, Gao Z, Zhang L. Fabrication and performance of a power generation device based on stacked piezoelectric energy-harvesting units for pavements. *Energy Convers Manag*. 2018 May 1;163:196–207.
 43. Shin Y-H, Jung I, Noh M-S, Kim JH, Choi J-Y, Kim S, et al. Piezoelectric polymer-based roadway energy harvesting via displacement amplification module. *Appl Energy*. 2018 Apr 15;216:741–50.
 44. Rui X, Li Y, Liu Y, Zheng X, Zeng Z. Experimental Study and Parameter Optimization of a Magnetic Coupled Piezoelectric Energy Harvester. *Appl Sci*. 2018 Dec;8(12):2609.
 45. Yesner G, Kuciej M, Safari A, Jasim A, Wang H, Maher A. Piezoelectric energy harvesting using a novel cymbal transducer design. In: 2016 Joint IEEE International Symposium on the Applications of Ferroelectrics, European Conference on Application of Polar Dielectrics, and Piezoelectric Force Microscopy Workshop (ISAF/ECAPD/PFM). 2016. p. 1–4.
 46. Wang C, Song Z, Gao Z, Yu G, Wang S. Preparation and performance research of stacked piezoelectric energy-harvesting units for pavements. *Energy Build*. 2019 Jan;183:581–91.
 47. Ewart LM, McLaughlin EA, Gittings KD. Investigation of the Compressive Material Properties of PZT and PMN [Internet]. Newport, Rhode Island: Naval Undersea Warfare Center Division; 1999 Dec [cited 2019 Feb 25]. Report No.: TR 11,184. Available from: <https://apps.dtic.mil/dtic/tr/fulltext/u2/a379761.pdf>
 48. Piezoelectric Properties Of Piezo Materials [Internet]. [cited 2020 Oct 9]. Available from: <https://www.americanpiezo.com/apc-materials/physical-piezoelectric-properties.html>
 49. Su Y, Dagdeviren C, Li R. Measured Output Voltages of Piezoelectric Devices Depend on the Resistance of Voltmeter. *Adv Funct Mater*. 2015 Sep;25(33):5320–5.
 50. Ladvánszky J. *Theory of Power Matching*. Springer; 2019. 86 p.
 51. Hehn T, Manoli Y. Piezoelectricity and Energy Harvester Modelling. In: *CMOS Circuits for Piezoelectric Energy Harvesters* [Internet]. Dordrecht: Springer Netherlands; 2015 [cited 2019 Mar 1]. p. 21–40. Available from: http://link.springer.com/10.1007/978-94-017-9288-2_2

52. Khalili M, Biten AB, Vishwakarma G, Ahmed S, Papagiannakis AT. Electro-mechanical characterization of a piezoelectric energy harvester. *Appl Energy*. 2019 Nov 1;253:113585.
53. Timm DH, Priest A. Wheel Wander at the NCAT Test TRack. National Center for Asphalt Technology; 2005.
54. Montoya A, Jagtap P, Papagiannakis A, Dessouky S, Walubita L. Numerical Study on Design and Installation of Energy-Harvesting Modules Embedded within a Flexible Pavement Structure. *J Transp Eng Part B Pavements*. 2020 Dec 1;146(4):04020066.
55. Miller J, Bellinger W. Distress Identification Manual for the Long-Term Pavement Performance Program (Fifth Revised Edition) [Internet]. Office of Infrastructure Research and Development Federal Highway Administration; 2014 May [cited 2021 Feb 26]. Report No.: FHWA-HRT-13-092. Available from: <https://www.fhwa.dot.gov/publications/research/infrastructure/pavements/ltp/13092/13092.pdf>
56. Traffic Monitoring Guide, Federal Highway Administration. Washington DC; 2016 Oct.
57. STM8L152M8 [Internet]. STMicroelectronics. [cited 2020 Nov 12]. Available from: <https://www.st.com/en/microcontrollers-microprocessors/stm8l152m8.html>
58. OM40006|IoT Module Base Board | NXP [Internet]. [cited 2020 Nov 12]. Available from: <https://www.nxp.com/products/processors-and-microcontrollers/arm-microcontrollers/general-purpose-mcus/lpc54000-cortex-m4-/iot-module-base-board:OM40006#buy>